

DEVELOPMENT OF A SABOT DESIGN TOOL  
FOR AEROBALLISTIC RANGE TESTING

A THESIS SUBMITTED TO  
THE GRADUATE SCHOOL OF NATURAL AND APPLIED SCIENCES  
OF  
MIDDLE EAST TECHNICAL UNIVERSITY

BY

KARACA EFE KAFDAĞLI

IN PARTIAL FULFILLMENT OF THE REQUIREMENTS  
FOR  
THE DEGREE OF MASTER OF SCIENCE  
IN  
AEROSPACE ENGINEERING

SEPTEMBER 2006

Approval of the Graduate School of Natural and Applied Sciences

---

Prof. Dr. Canan ÖZGEN  
Director

I certify that this thesis satisfies all the requirements as a thesis for the degree of Master of Science.

---

Prof. Dr. Nafiz ALEMDAROĞLU  
Head of Department

This is to certify that we have read this thesis and that in our opinion it is fully adequate, in scope and quality, as a thesis for the degree of Master of Science.

---

Assoc. Prof. Dr. Altan KAYRAN  
Supervisor

**Examining Committee Members**

Prof. Dr. Yavuz YAMAN	(METU, AE)	_____
Assoc. Prof. Dr. Altan KAYRAN	(METU, AE)	_____
Assoc. Prof. Dr. Serkan ÖZGEN	(METU, AE)	_____
Dr. Gökmen MAHMUTYAZICIOĞLU	(TÜBİTAK-SAGE)	_____
Dr. Volkan NALBANTOĞLU	(ASELSAN)	_____

**I hereby declare that all information in this document has been obtained and presented in accordance with academic rules and ethical conduct. I also declare that, as required by these rules and conduct, I have fully cited and referenced all material and results that are not original to this work.**

Name, Last name: Karaca Efe KAFDAĞLI

Signature :

# **ABSTRACT**

## **DEVELOPMENT OF A SABOT DESIGN TOOL FOR AEROBALLISTIC RANGE TESTING**

Kafdađlı, Karaca Efe

M.Sc., Department of Aerospace Engineering

Supervisor: Assoc. Prof. Dr. Altan Kayran

September 2006, 156 pages

The aim of this thesis is to investigate the general design and analysis principles of sabots and to develop a sabot design tool. Structures which support and align the models in gun bore, and separate without disturbing the flight path of models are called sabots. In the scope of this study, structurally critical regions and loads acting on sabots due to acceleration in the gun are determined. To calculate the loads acting and to size the sabots, approximate relations are derived by the help of strength of materials approach and finite element solutions. Conventional sabots are investigated and new sabot geometries are designed to resist high accelerations.

To achieve the desired test velocity without affecting the stability of the model is the main objective. Sabots should be as light as possible, to reach the desired velocity with minimum inertial load, in other words minimum gun chamber pressure. To obtain the less weight sabot geometry with enough strength to resist the loads acting, a computer tool is developed. Structural analyses are automatically performed by the help of the sabot design tool. The advantage of the

design tool is to reduce the design engineer's work time spent for routine analyses processes.

The output of the tool, which is sabot geometry, should be evaluated as a result of preliminary design process, and can be used as an input for detailed design process. Detailed geometric modifications required for production can be applied on the tool output, and final product can be manufactured reliably and in the shortest possible time.

Keywords: Aeroballistics, Aeroballistic Range Testing, Sabot Design and Analysis

# ÖZ

## AEROBALİSTİK TESTLERDE KULLANILAN SABOTLAR İÇİN TASARIM ARACI GELİŞTİRİLMESİ

Kafdađlı, Karaca Efe

Yüksek Lisans, Havacılık ve Uzay Mühendisliđi Bölümü

Tez Yöneticisi: Doç. Dr. Altan Kayran

Eylül 2006, 156 sayfa

Bu çalışmanın amacı, aerobalistik testlerde kullanılan sabotlar için genel tasarım ve analiz yöntemlerinin belirlenmesi ve sabot tasarım yazılımı geliştirilmesidir. Namlu içerisinde hareketleri boyunca modelleri destekleyen, hizalayan ve namlu çıkışında modellerin uçuş doğrultusunu bozmadan ayrılan yapılara sabot denir. Bu çalışma kapsamında, namlu içerisindeki ivmelenme esnasında sabotlar üzerindeki yapısal kritik bölgeler ve etki eden yükler belirlenmiş, bu yüklerin hesaplanması için temel mukavemet bilgisinin yanı sıra sonlu elemanlar analiz çözümleri kullanılarak yaklaşık bağıntılar ve formüller türetilmiştir. Yapılan çalışmalarda geleneksel sabotlar incelenmiş bunun yanı sıra yüksek ivmelere dayanabilecek yeni bir sabot tasarımı gerçekleştirilmiştir.

İstenen test hızına modelin kararlılığını bozmadan ulaşabilmek esas amaçtır. Belirlenen hıza en az eylemsizlik kuvvetine maruz kalarak, bir başka deđişle en düşük namlu içi basınçlar altında ulaşabilmek için sabotların mümkün olduğunca hafif olması gerekmektedir. En hafif geometriye sahip olabilecek aynı zamanda da namlu içi yüklerle dayanabilecek sabotun tasarımı için tez çalışması kapsamında bir

kod yazılmıştır. Bu kod sayesinde sabot tasarımı için gerekli olan yapısal analizler otomatik olarak gerçekleştirilebilmektedir. Test koşullarındaki veya model geometrisindeki en ufak bir değişiklikte yapısal analizlerin her bölge için baştan yapılması gerektiğinden, sabot tasarım aracı tasarımcı için oldukça faydalı ve iş gücünü azaltan bir araç özelliğine sahiptir.

Sabot tasarım aracının çıktısı olarak verilen sabot geometrisi ön tasarımın bir sonucu olarak değerlendirilmeli, detaylı tasarıma girdi oluşturmak için kullanılmalıdır. Üretim için gerekli olan detaylı geometrik değişiklikler çıktı üzerinde uygulanabilir ve son ürün mümkün olan en kısa zamanda ve güvenilir bir biçimde üretilebilir.

Anahtar Kelimeler: Aerobalistik, Aerobalistik Test, Sabot Tasarımı ve Analizi

To My Wife

## ACKNOWLEDGMENTS

I would like to express my special thanks and gratitude to my supervisor Assoc. Prof. Dr. Altan KAYRAN for his guidance, motivation and patience.

I would like to state my gratitude to Vedat EKÜTEKİN and Koray DAYANÇ for their support and advices.

My test team members A. Arda ÖZYÜKSEL, İ. Murat KARBANCIOĞLU and Ali İhsan AKBAŞ are gratefully acknowledged for their effort in tests and suggestions.

I would like to thank my colleagues Selçuk ATAÇ, Sevsay AYTAR ORTAÇ, Ümit KUTLUAY, İlke AYDINCAK, Barış SABUNCUOĞLU and Tuğrul KOZAK for their support and comments.

This study was supported by TÜBİTAK-SAGE and its support is greatly acknowledged.

Finally I would like to thank my mother and my father for their corrections and suggestions in my thesis study and for their support throughout my life. I would like to thank my wife and my brother for their endless love, understanding and patience.

# TABLE OF CONTENTS

<b>PLAGIARISM</b> .....	<b>iii</b>
<b>ABSTRACT</b> .....	<b>iv</b>
<b>ÖZ</b> .....	<b>vi</b>
<b>ACKNOWLEDGMENTS</b> .....	<b>ix</b>
<b>TABLE OF CONTENTS</b> .....	<b>x</b>
<b>LIST OF TABLES</b> .....	<b>xiii</b>
<b>LIST OF FIGURES</b> .....	<b>xiv</b>
<b>LIST OF SYMBOLS</b> .....	<b>xix</b>
<b>CHAPTERS</b>	
<b>1 INTRODUCTION</b> .....	<b>1</b>
1.1 OVERVIEW .....	1
1.2 AEROBALLISTIC RANGE TESTING IN SAGE .....	3
1.3 OVERVIEW ON SABOTS .....	6
1.3.1. Functions of Sabots .....	7
1.3.2. Sabot Types .....	10
1.4 AIM OF THE STUDY .....	13
1.5 SCOPE OF THE STUDY .....	13
<b>2 SABOT DESIGN PRINCIPLES</b> .....	<b>15</b>
2.1 GENERAL DESIGN CONSIDERATIONS FOR SABOTS.....	15
2.2 STRUCTURAL ANALYSIS OF SABOTS .....	16
2.2.1 Assumptions and Limitations.....	17
2.2.2 Sabot Separation.....	18
2.2.3 Sabot Configurations.....	19
2.2.4 Forces Acting on Sabot-1 and Critical Regions.....	20
2.2.5 Conceptual Design of Sabot-2.....	26
2.2.6 Forces Acting on Sabot-2 and Critical Regions.....	30

2.3	STRESS FORMULATIONS .....	32
2.3.1.	Derivation of Stress Relations for the Pusher .....	32
2.3.2.	Sabot-1 Pusher Stress Analysis.....	46
2.3.3.	Sabot-2 Pusher Stress Analysis.....	51
2.3.4.	Sabot-1 Stress Analysis.....	54
2.3.5.	Sabot-2 Stress Analysis.....	69
<b>3</b>	<b>SABOT DESIGN TOOL .....</b>	<b>73</b>
3.1	MODIFICATIONS ON SABOT GEOMETRIES.....	74
3.2	MATERIAL SELECTION .....	83
3.3	CALCULATION OF PROJECTILE-SABOT PACKAGE ACCELERATION .....	85
3.4	CALCULATION OF PRESSURE.....	90
3.5	CALCULATION OF CORRECTION FACTORS, $c_n$ .....	91
3.5.1.	Sabot-1 Correction Factors.....	92
3.5.2.	Sabot-2 Correction Factors.....	96
3.6	ITERATIONS .....	98
3.6.1.	Sabot Design Tool for Sabot-1.....	99
3.6.2.	Sabot Design Tool for Sabot-2.....	103
<b>4</b>	<b>VERIFICATION OF THE SABOT DESIGN TOOL .....</b>	<b>107</b>
4.1	TEST MODELS .....	107
4.2	TEST CASES.....	109
4.3	FINITE ELEMENT ANALYSES.....	111
4.3.1.	MSC NASTRAN <sup>®</sup> /PATRAN <sup>®</sup> Analyses.....	111
4.3.2.	DISCUSSION OF STATIC FEA RESULTS .....	117
4.3.3.	MSC MARC <sup>®</sup> /MENTAT <sup>®</sup> Analysis.....	118
4.3.4.	DISCUSSION OF TRANSIENT FEA RESULTS .....	127
4.4	FML TESTS.....	128
4.4.1.	PRODUCTION OF THE SABOTS.....	128
4.4.2.	TEST SETUP .....	132
4.4.3.	TEST RESULTS.....	133
4.4.4.	DISCUSSION OF THE FML TEST RESULTS .....	137

<b>5 DISCUSSION AND CONCLUSION.....</b>	<b>140</b>
5.1 DISCUSSION .....	140
5.2 CONCLUSION .....	143
5.3 FUTURE WORK .....	144
<b>REFERENCES.....</b>	<b>146</b>
<b>APPENDICES</b>	
<b>A PRESSURE DATA.....</b>	<b>148</b>
<b>B SABOT SECTION COORECTION FACTORS.....</b>	<b>151</b>
B.1 SECTION-1 CORRECTION FACTORS .....	151
B.2 SECTION-3 CORRECTION FACTORS .....	152
<b>C TECHNICAL DRAWING OF A SABOT .....</b>	<b>155</b>

## LIST OF TABLES

Table 1 Thin Plate and Thick Plate Results .....	42
Table 2 Plastic Material Properties .....	84
Table 3 Aluminum Properties .....	84
Table 4 Gun Parameters .....	85
Table 5 A, L and $c_{nA}$ values for B=15 mm.....	94
Table 6 A, L and $c_{nC}$ values for B=15 mm.....	96
Table 7 Model Specifications.....	108
Table 8 Test Cases.....	109
Table 9 General Inputs for the Tool.....	110
Table 10 Tool Output – General .....	110
Table 11 Tool Output – Pusher .....	110
Table 12 Tool Output – Sabot.....	111
Table 13 Test Results-1 .....	134
Table 14 Test Results-2.....	134
Table 15 Sabot Comparison Results Taken From SDT .....	141
Table 16 Pusher Comparison Results Taken From SDT .....	142

## LIST OF FIGURES

Figure 1 Yaw cards .....	4
Figure 2 Model signature .....	5
Figure 3 Powder gas gun used in FML .....	5
Figure 4 Sabot- Projectile Package .....	7
Figure 5 Functions of Sabot .....	8
Figure 6 Nose angle .....	9
Figure 7 Pusher Type Sabot .....	10
Figure 8 3D view of pusher type sabot .....	11
Figure 9 Puller type sabot.....	11
Figure 10 Special type sabot .....	13
Figure 11 Design flowchart.....	16
Figure 12 3D view of Sabot-1 .....	20
Figure 13 Sabot-1 and projectile layout .....	21
Figure 14 Forces acting on sabot.....	21
Figure 15 Obturation .....	22
Figure 16 Free body diagram of pusher .....	22
Figure 17 Pusher deformation .....	23
Figure 18 Free body diagram of sabot .....	24
Figure 19 Package inbore view .....	24
Figure 20 y-displacement of Sabot-1 .....	25
Figure 21 Critical regions for sabot.....	26
Figure 22 APFSDS.....	27
Figure 23 KE Projectile sabot .....	27
Figure 24 Separation Mechanisms .....	28
Figure 25 Drag force acting on sabot.....	29
Figure 26 Sabot-2 geometry .....	29

Figure 27 3D View of Sabot-2 .....	30
Figure 28 Forces acting on Sabot-2.....	31
Figure 29 Free body diagram of Sabot-2 pusher.....	31
Figure 30 Critical regions for Sabot-2 .....	32
Figure 31 Polar coordinate system.....	36
Figure 32 Simply supported circular plate .....	37
Figure 33 y vs. thickness plot.....	43
Figure 34 Non-uniform loading of circular plate.....	44
Figure 35 3D half view of Sabot-1.....	47
Figure 36 Free body diagram of Sabot-1 pusher.....	47
Figure 37 Free body diagram of shear loading .....	50
Figure 38 3D half view of Sabot-2.....	52
Figure 39 Free body diagram of Sabot-2 pusher.....	52
Figure 40 Superposition of sabot pressure .....	53
Figure 41 Sections of Sabot-1 .....	54
Figure 42 Section-1 assumption.....	55
Figure 43 Bending due to distributed load [13] .....	56
Figure 44 Sabot-1 section-1 .....	57
Figure 45 Arc length 'b'.....	57
Figure 46 Section-1 compression force.....	59
Figure 47 Equivalent system for buckling analysis .....	61
Figure 48 Column buckling .....	61
Figure 49 Curved column buckling.....	62
Figure 50 Actual length of a column.....	64
Figure 51 Sabot-1 section-3 .....	66
Figure 52 Section angles .....	66
Figure 53 Diameters of Sabot-1 for calculations .....	69
Figure 54 Sections of Sabot-2 .....	69
Figure 55 Sabot-2 section-3 .....	70
Figure 56 Diameters of Sabot-1 for calculations .....	72
Figure 57 Sabot-1 FEM analysis.....	74
Figure 58 Sabot-2 FEM analysis.....	75

Figure 59 Predicted critical regions for Sabot-1 .....	75
Figure 60 Predicted critical regions for Sabot-2 .....	76
Figure 61 Mach vs. Pusher Thickness Graph.....	76
Figure 62 Sabot-1 pusher support .....	77
Figure 63 Sabot-1 modification.....	78
Figure 64 Sabot-2 modification.....	78
Figure 65 Section-3 von Misses stress .....	79
Figure 66 3D Model of sabot with BC modification .....	79
Figure 67 Modified section-3 von Misses stress.....	80
Figure 68 Upper section-3 von Misses stress.....	81
Figure 69 3D Model of sabot with CD modification .....	81
Figure 70 Modified upper section-3 von Misses stress.....	82
Figure 71 Increased thickness A .....	82
Figure 72 GPSIM output .....	86
Figure 73 Pusher at the entrance of the gun .....	90
Figure 74 Mass vs. Max. Pressure graph .....	91
Figure 75 Section-1 correction factor calculation.....	92
Figure 76 An example finite element analysis for $c_{nA}$ .....	93
Figure 77 Sabot-1 section-3 correction factor calculation .....	95
Figure 78 FEA results for section-3 of Sabot-2 .....	97
Figure 79 Sabot-2 section-3 correction factor calculation .....	98
Figure 80 Inputs for Sabot-1 .....	100
Figure 81 Flow Chart of SDT for Sabot-1 .....	102
Figure 82 Output of SDT for Sabot-1 .....	103
Figure 83 Inputs for Sabot-2 .....	104
Figure 84 Inputs for Sabot-2, back view .....	105
Figure 85 Output of SDT for Sabot-2 .....	105
Figure 86 Flow Chart of SDT for Sabot-2 .....	106
Figure 87 TOROS and BASIC WAF models .....	108
Figure 88 Loading and boundary conditions for FEA .....	112
Figure 89 Tet10 element .....	112
Figure 90 Test Case 1; Top view of Sabot-1.....	113

Figure 91	Test Case 1; Bottom view of Sabot-1 .....	113
Figure 92	Test Case 1; Section-1 view of Sabot-1 .....	114
Figure 93	Test Case 1; Section-3 view of Sabot-1 .....	114
Figure 94	Test Case 3; Top view of Sabot-1 .....	115
Figure 95	Test Case 3; Bottom view of Sabot-1 .....	115
Figure 96	Test Case 4; Top view of Sabot-2 .....	116
Figure 97	Test Case 4; Section-1 view of Sabot-2 .....	116
Figure 98	Test Case 4; Section-3 view of Sabot-2 .....	117
Figure 99	Pressure vs time graph .....	119
Figure 100	Test Case 3 boundary condition and loading .....	120
Figure 101	Test Case 3 contact surfaces and materials .....	120
Figure 102	Package velocity profile .....	121
Figure 103	Package acceleration profile .....	122
Figure 104	Motion in gun bore .....	123
Figure 105	Test Case 3; time increment 15 .....	123
Figure 106	Stress profile at the center of the pusher .....	124
Figure 107	Test Case 3 section-3, time increment 25 .....	125
Figure 108	Stress profile of section-3 node X .....	125
Figure 109	Test Case 3 section-3, time increment 25 .....	126
Figure 110	Stress profile of section-1 node Y .....	126
Figure 111	Stress profile at section-4 of sabot .....	127
Figure 112	Shear pin .....	129
Figure 113	Sabot-2 obturation .....	129
Figure 114	Produced pushers and obturators .....	130
Figure 115	Sabot-2 pusher after bonding process .....	130
Figure 116	Contact surfaces between two parts of Sabot-2 .....	131
Figure 117	Produced Sabot-2 parts .....	131
Figure 118	Sabot-1, pusher and Basic WAF package .....	132
Figure 119	Sabot-2 packages for two different projectiles .....	132
Figure 120	Example view from velocity measurement software .....	135
Figure 121	High speed camera images .....	136
Figure 122	Obturation surface comparison .....	138

Figure 123 Deformed projectile after fire .....	139
Figure 124 Mach vs. Sabot Mass graph .....	141
Figure 125 Mach vs. Pusher Mass graph .....	142
Figure 126 Mass vs. Pressure graph for Mach 0.8 .....	148
Figure 127 Mass vs. Pressure graph for Mach 0.9 .....	149
Figure 128 Mass vs. Pressure graph for Mach 1.2 .....	149
Figure 129 Mass vs. Pressure graph for Mach 2 .....	150
Figure 130 Mass vs. Pressure graph for Mach 2.5 .....	150
Figure 131 Technical drawing of the sabot group.....	155
Figure 132 Technical drawing of pusher.....	156
Figure 133 Technical drawing of pusher and support plate assembly .....	156

## LIST OF SYMBOLS

a	acceleration, radius of plate
c	thickness of plate from midsurface
cn	constant
D	gun diameter
d	model diameter
ds	sabot diameter
E	modulus of elasticity
F	force
G	modulus of elasticity in shear
I	moment of inertia
M	moment, mass
P	pressure
Pm	Pressure due to model
Ps	Pressure due to sabot
q	distributed load
r	radius
t	thickness
u, v, w	axial, tangential and radial displacements
w	load per unit length
x, y, z	distances, rectangular coordinates
y	equation of fitted curve
$\gamma$	shear strain
$\varepsilon$	normal strain
R, $\psi$	polar coordinates
r, z, $\theta$	cylindrical coordinates

$\mu$	coefficient of friction
$\nu$	Poisson's ratio
$\rho$	density
$\sigma$	normal stress
$\sigma_y$	yield stress
$\tau$	shear stress
$\phi$	stress function
$\nabla^2$	Laplace operator

### **Acronyms**

3D	Three Dimensional
AL	Aluminum
APFSDS	Armour-Piercing Fin-Stabilized Discarding Sabot
CFD	Computational Fluid Dynamics
CG	Center of Gravity
FEA	Finite Element Analysis
FEM	Finite Element Modeling
FML	Flight Mechanics Laboratory
KE	Kinetic Energy
PC	Polycarbonate
SDT	Sabot Design Tool
WAF	Wrap Around Fin

# CHAPTER 1

## INTRODUCTION

### 1.1 OVERVIEW

In the last decade by the development of advanced technologies, defense industries tend to search and develop more aerial systems. High-tech aircrafts, smart weapons, stand-off munitions, unmanned air vehicles are all being developed and used. In the design phase and development of these air vehicles, engineers need to know aerodynamic parameters such as drag and lift coefficients, stability derivatives, control derivatives etc. To obtain these parameters currently there are several methods in use [1], which are;

- Full scale flight testing
- Computational Aerodynamics
- Experimental Aerodynamics (Wind tunnel testing)
- Experimental flight dynamics

In full scale flight testing technique full scale instrumented (accelerometers, strain gages, gyroscopes, thermo couples and other sensors) model is tested. Full scale model is attached to the aircraft by using certified pylons. Models are carried or released from the aircraft and data are obtained from both, aircraft and model. Release of models from the aircraft is mostly used for munitions, weapons and missiles. Some space shuttles are also carried on large airplanes to be tested. The disadvantage of this is its high cost because of expensive sensors and full scale

production. Another disadvantage is the difficulties encountered in controlling test conditions.

Computational methods are becoming more important in almost every branch of engineering. However, computational aerodynamics is far from being the unique prediction method because of its limited speed. Without validating the estimated parameters using theoretical and experimental methods, computational aerodynamic results have less reliability [1].

By the help of the theoretical and empirical aerodynamics, large parameter database exists for basic aerodynamic geometries. But for complex geometries basic aerodynamic parameters are not satisfactory.

Wind tunnel testing is one of the techniques for experimental aerodynamics. In wind tunnel tests, air surrounding the model is accelerated to reach the flight conditions in the air. Variety of data with high accuracy can be obtained with wind tunnels. However, especially for missiles wide Mach number range from subsonic to hypersonic flow is needed, and cost for performing wind tunnel test increases drastically with increasing Mach number. Besides this, connecting element used for mounting the model in the tunnel distorts the flow around the most important region which is base of the model [1].

Another experimental method for estimating the aerodynamic parameters is experimental flight dynamics. Aeroballistics is a branch of experimental flight dynamics. Aeroballistics is the science of motion of projectiles in flight. Flying object that follows a ballistic trajectory is called projectile. Aeroballistic range is an indoor firing range used to examine the flight dynamics, exterior aerodynamics, wake phenomena, aerodynamic heating, ballistics of various models in free flight and impact loading behavior of materials [2]. In aeroballistic range tests the projectile itself is accelerated to the required test velocities. To accelerate the projectile to the desired velocities some kind of guns are used. The projectile is placed in a gun and fired. During its flight within its range, the model is tracked by

data acquisition systems through the test section. Yaw, pitch and roll attitude of the model is observed, and aerodynamic coefficients are predicted from these flight data. There are two main methods used for measuring flight data [1]:

- **Photographic Stations:** Photographic stations are lined up with a known distance along the range on the path of the projectile. While projectile is passing through the station, photograph of the model or shadow of the model is taken from two orthogonal directions with the time information. After processing the images, flight parameters can be obtained.
- **Yaw Card Stations:** Yaw card is a sheet of paper hanged in a plane normal to the flight path. The model punches the cards as the model passes through. The hole on the card gives information about the attitude of the model at the time of punching.

Different types of guns are used in aeroballistic range tests according to test requirements. Technology of powder gas guns is old such that they have been used for more than fifty years. Gunpowder is ignited and generated gases fire the projectiles. They are useful for low and intermediate speeds (up to Mach 5). If higher speeds are needed, light-gas gun is the most common solution. Compressed hydrogen or helium gases are released and push the model outside the gun tube. Models can be accelerated up to Mach 40 (11 km/sec).

## **1.2 AEROBALLISTIC RANGE TESTING IN SAGE**

TÜBİTAK-SAGE (Türkiye Bilimsel ve Teknolojik Araştırma Kurumu – Savunma Sanayii Araştırma ve Geliştirme Enstitüsü) owns the only aeroballistic range facility in TURKEY which is called FLIGHT MECHANICS LABORATORY (FML) and it is a member of Aeroballistic Range Association (ARA) since 1996. FML is composed of three main structures. Test section, gun and fire control room.

Test section is a closed and 200 m long building. Models are fired into this building and they travel for 200 m in the test section. Entrance of the section is made of reinforced concrete wall which is protected by sand bags. 200 mm diameter hole is the only gate on the concrete wall where the models enter after 20 m free flight. This hole allows only the entrance of the projectile. Since sensitive and expensive measuring devices (photographic stations etc.) and sensors are located in the test section, any other destructive materials should not enter.

FML has 30 yaw card (Figure 1) and 8 photographic stations to obtain desired flight parameters of projectiles. An example of a yaw card with hole is given in Figure 2. While projectile is passing through the yaw card, it vibrates the card. Accelerometers attached on the yaw cards trigger the system and time of flight can be stored. Also velocity measurement system is used inside the test section.



**Figure 1** Yaw cards

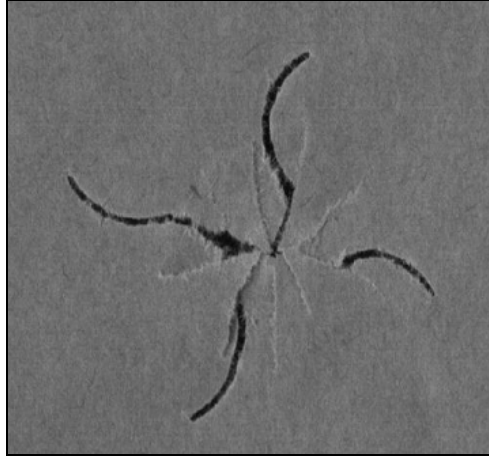


**Figure 2** Model signature

In flight mechanics laboratory, models are accelerated by using powder gas gun (Figure 3). Diameter of the gun is 100 mm and it has a barrel length of 5.5 m. The gun can accelerate models up to Mach 5.



**Figure 3** Powder gas gun used in FML

Tests are conducted for missile and rocket models in TÜBİTAK-SAGE. The models can be accelerated up to Mach 3 because of the structural constraints in the

production of the models. Aeroballistic range tests are performed at full scale Mach numbers in FML. Since the flight time is very short, error generated due to unscaled gravity force is assumed to be negligible.

Models are dynamically scaled rockets, missiles and munitions. Dimensions and the location of the center of gravity are scaled down. On the other hand, the ratio of the axial inertia to transverse inertia of the projectile should be same as the original munitions.

### **1.3 OVERVIEW ON SABOTS**

As stated in the previous section, projectiles used in aeroballistic range tests are scaled down models of the flying objects, therefore, projectiles may have fins, canards, wings or different geometric shapes. Because of these geometric differences, projectiles do not fit in the gun tube exactly; they have smaller diameters compared to the gun. Sabots act as adapter/carrier supporting structures and they are necessary to launch sub-caliber projectiles during gun tube (barrel) travel (Figure 4).

A sabot refers to a device named for a shoe used in a gun to fire a model that is smaller than the bore diameter. Since a strong seal is needed to trap propellant gasses behind the model, and keep the model centered in the barrel, something is needed to fill the gap between model and barrel, which is the role of the sabot.

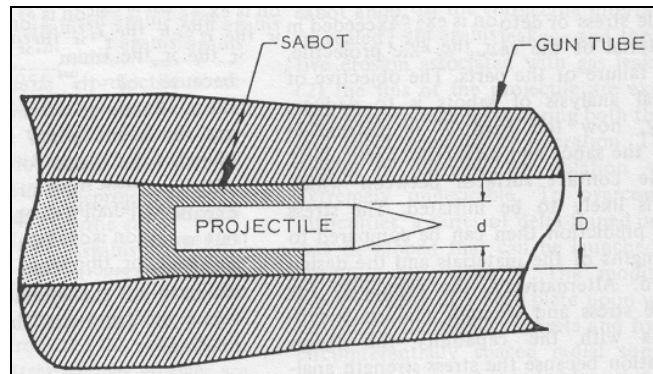


**Figure 4 Sabot- Projectile Package**

A sabot is a component of a weapon system designed for the ultimate goal of delivering a specified projectile to a target at a prescribed range with desired velocity and with acceptable dispersion [3].

### **1.3.1. Functions of Sabots**

Sabot aligns the model in the gun (Figure 5). If sabot is not manufactured within the given tolerances, when model is placed in the barrel it will have misalignment. As a result, model will not follow the predicted trajectory or have oscillations. This causes wrong projectile signs on the yaw cards. In addition, it is important that, in range testing, model must enter the test section from the 200 mm hole after firing. When the model is launched, it travels in the air approximately 20 m before entering the test section. Misaligned model usually hits the structure around the entrance hole and crashes.

Sabot also seals the gun pressure behind the model (Figure 5). It acts as an obturator. Models do not have any contact with gun tube wall, the only interface is the sabot. Contact surfaces between sabot-model and sabot-gun wall should fit to each other and seal the gases perfectly. The only force that accelerates the model is

the pressure behind the model. Gas leakage should be minimized otherwise desired velocity at the muzzle can not be reached.

There are several methods used for obturation. Producing the pusher part with a radius equal to the barrel radius is not enough for sealing the gases. Using plastic or elastomeric seals at the periphery of the sabot are common. In addition to that, if deformable materials like plastics, lexan etc, is used for sabot production, usually aft end of the pusher is made larger than the gun bore.

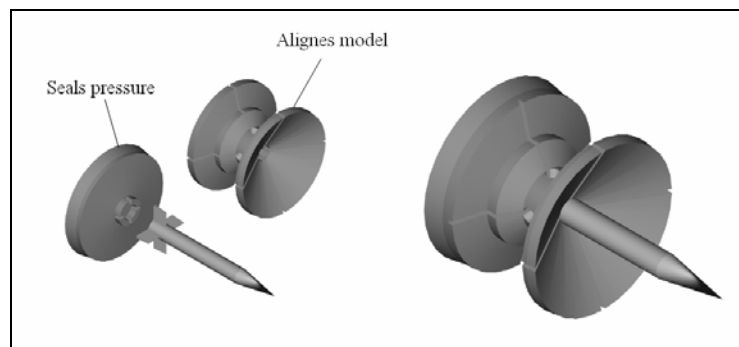


**Figure 5** Functions of Sabot

The aim of aeroballistic range testing is to test the projectile. It is only the model which enters the test section, while traveling on its trajectory. This means that sabot separates from the model after exiting the barrel. Sabot should separate smoothly without disturbing the flight path of the model. Since sabot may cause damage to systems or trigger measurement devices, it should not travel all the way to the end of the projectile's range. If separation time takes a long time, such as 0.03 seconds, that is an indication of the fact that sabot has followed the model too closely for a long distance and this may affect the wake flow [4]. Geometry of the sabot determines the separation time. Drag and lift, CG position and nose angle (Figure 6) of the sabot are the mainsprings for separation mechanisms.

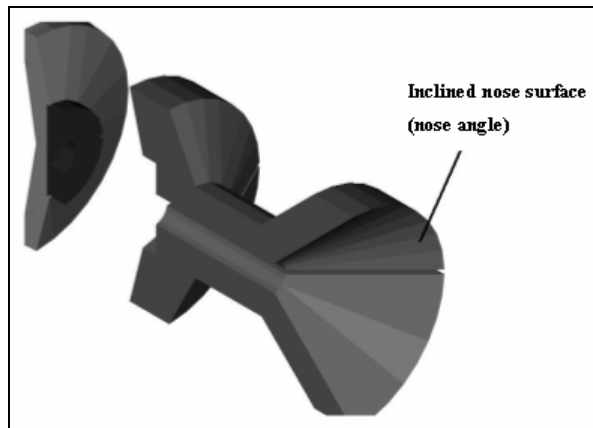


**Figure 6** Nose angle

Separation of sabots from the model is accomplished by five different mechanisms [4];

- Sabot parts are pulled radially outward because of the pressure acting on the beveled frontal face of the sabot (nose angle). This mechanism is called as aerodynamic separation. Sabot base plate and model can be axially separated by this mechanism. Light sabot parts can easily separate.
- Propellant gas separation mechanism can be achieved by hole or cavity machined in from the base at the interfaces of base and also sabot walls. High pressure propellant gas starts to separate the sabot parts at the muzzle.
- If sabot is made slightly oversize and compressed when loaded into the gun, upon leaving the barrel the rebound force causes the segments to separate. This mechanism is called internal elastic separation.
- Centrifugal mechanism can only be used if gun is rifled. Centrifugal forces to separate sabot does not rely on any internal and external pressure forces. Its use is limited to desired high roll rate.
- An external plate can be placed on the path of the flight of the model so that it allows only the model to pass. Such a plate is called sabot stripping plate.

### 1.3.2. Sabot Types

Sabot geometry depends on projectile geometry, test conditions (desired velocity, gun properties, etc.) and design engineer. It may have infinitely different geometries. But there are three main types of sabot with respect to their coverage of the projectile.

The first type is pusher type (Figure 7 & Figure 8). This type is composed of two parts; pusher and sabot walls. Pusher acts as an obturator and pushes the model. Sabot walls align the model in the barrel. At least two sabot walls should be used to separate the sabot from the model. If the difference between diameters of the model and the gun is high, the use of more than three sabot walls will be efficient. Because, as the diameter of the projectile decreases, sabot material used increases, and this means that the weight of the sabot wall increases. If sabot is not divided more than two parts separation will be difficult. Usually pusher type is used for simple geometries because of convenience in production.

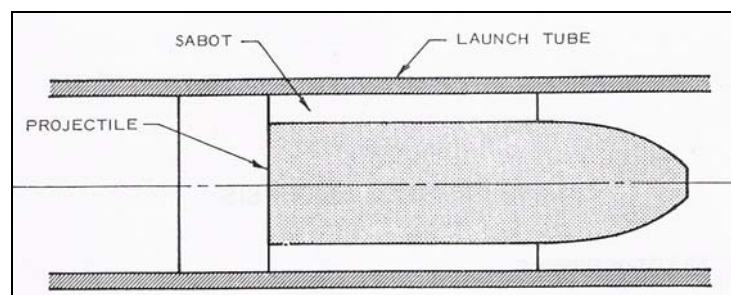


**Figure 7** Pusher Type Sabot

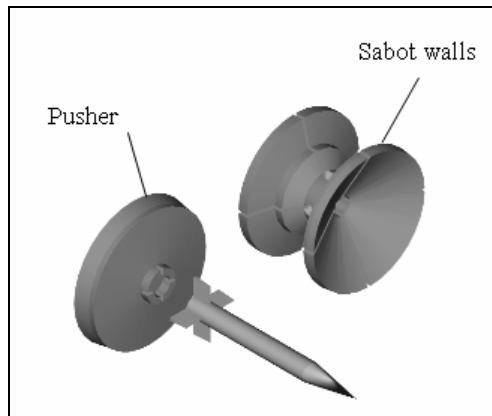


**Figure 8** 3D view of pusher type sabot

Another type is puller type sabot (ring sabot), composed of more than two parts (Figure 9). Sabot surrounds the model and by the help of the friction or buttress groove shapes on the surface between the sabot and model, sabot pulls the model at the region of center of gravity. Ring sabots are mostly used for kinetic energy projectiles (KE projectile). Kinetic energy ammunition relies on kinetic energy achieved through high velocity (more than Mach 5) and heavy, high aspect ratio rods to penetrate the armors [5], [6].

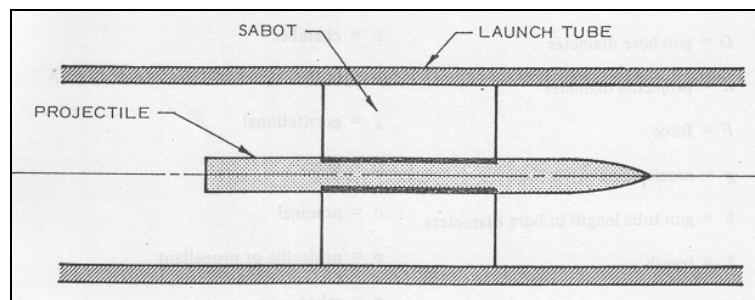


**Figure 9** Puller type sabot

Based upon the empirical evidences at Lockheed Propulsion Company Ballistic Research Laboratories, the following criterion has been established [3];

- $\frac{d}{D} > 0.40$  Use pusher type
- $\frac{d}{D} < 0.40$  Use puller type sabot (ring sabot)

Capital letter “D” in the upper criterion refers to gun diameter and small “d” refers to projectile diameter. Sabot is used to fill the gap between the projectile and gun wall. According to the criterion, for small diameter projectiles the ring sabots should be preferred.

The pusher type sabot fills larger volume between projectile and gun wall than puller type. Therefore, puller type sabot is lighter than pusher type sabot. On the other hand, manufacturing costs for producing a ring sabot can be much higher than for an equivalent pusher type sabot. Using different materials to achieve both friction and sealing, grooves and detailed geometric shapes are necessities to achieve the desired pulling force. Perfect manufacturing with very small tolerances is the only way to be successful, since gas sealing is needed between;

- Sabot - gun tube wall
- Sabot parts
- Sabot – projectile

Another disadvantage of using ring sabot is that back portion and fins of the projectile are exposed to high temperature gases [3].

According to test requirements, conditions and equipments, different sabots can be used. For example; if test section is very close to the gun, separation of base plate (pusher) of pusher type sabot must be very fast to prevent entering into the test section. Therefore, an alternative design could be the combination of the sabot wall and pusher. While sabot walls are discarding outward, part of the pusher which is integral with the sabot wall also discards easily (Figure 10).

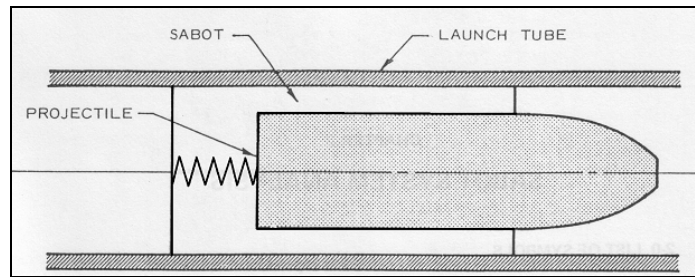


**Figure 10** Special type sabot

## **1.4 AIM OF THE STUDY**

The aim of this study is to investigate the design and analysis principles of a sabot design process and develop a sabot design tool which will enable faster sizing of sabots used for launching different projectiles. Design principles are investigated for conceptual and preliminary design phases. Since the main concern of this study is preliminary design, detailed and exact analyses will not be needed if the calculations are based on satisfactory assumptions. At the end of this work, stress analysis of sabots will be done easily without investigating design procedures and formulas from the beginning, by using finite element programs or complicated stress formulas.

In order to design a sabot, a computer tool is developed. Output of the tool is preliminary geometric information of a sabot that is suitable for desired test and loading conditions. By the help of the tool, engineering work and required time for routine design processes made by hand will be reduced.

## **1.5 SCOPE OF THE STUDY**

The main part of this work is based on geometrical and structural design of sabots using strength of materials approach supported by finite element analysis. In

Chapter 2, detailed information about sabots, their functions and general design considerations are presented. Assumptions are stated. Required relations, methods and procedures for stress analysis are derived in detail.

In Chapter 3, detailed information is given about the computer tool. MathWorks Inc.'s Matlab<sup>®</sup> 7.1 is selected as the development platform. Flowchart of the tool and analysis running in the tool are explained.

In Chapter 4, test cases are performed for the verification of the computer tool. The results of the tool is first drawn and modeled by using Mechanical Desktop<sup>®</sup> 2004 DX CAD tool, then analyzed by using commercial FEM software. Static analyses are performed by MSC NASTRAN<sup>®</sup>/PATRAN<sup>®</sup> and transient solutions are obtained from MSC MARC<sup>®</sup>/MENTAT<sup>®</sup> 2005. In addition to finite element analyses, sabots are produced with the dimensions obtained by the tool at TÜBİTAK-SAGE Mechanical Production Plant. The manufactured sabots are tested by firing them with their projectiles in FML. Firing tests are performed to see successful exit from the gun. Thus, occurrence of any failure on the sabots during their travel in the gun is monitored.

In Chapter 5, the evaluation of the study is done; remarks about the results are given.

## **CHAPTER 2**

### **SABOT DESIGN PRINCIPLES**

#### **2.1 GENERAL DESIGN CONSIDERATIONS FOR SABOTS**

As it is stated in the previous section, sabot is a protecting and supporting carrier of a projectile. The sabot must withstand the high pressure, temperature and acceleration in the gun barrel. Sabot design should be done by taking in the account high compulsive environment. Requirement for the aeroballistic range testing is to achieve pre-determined high muzzle velocity of the projectile. Therefore, lightest sabot-projectile package is desired. But minimizing the weight may increase the stress and deformation [3].

To achieve an optimum design which covers all the requirements is rarely possible. Most of the time, successful combination of best sabot and projectile is not obtained only by calculations, and a development period supported by firing tests with some corrective redesign is often necessary [4].

In Figure 11, engineering design process for a typical sabot is summarized. Sabot design process is done according to this design flowchart.

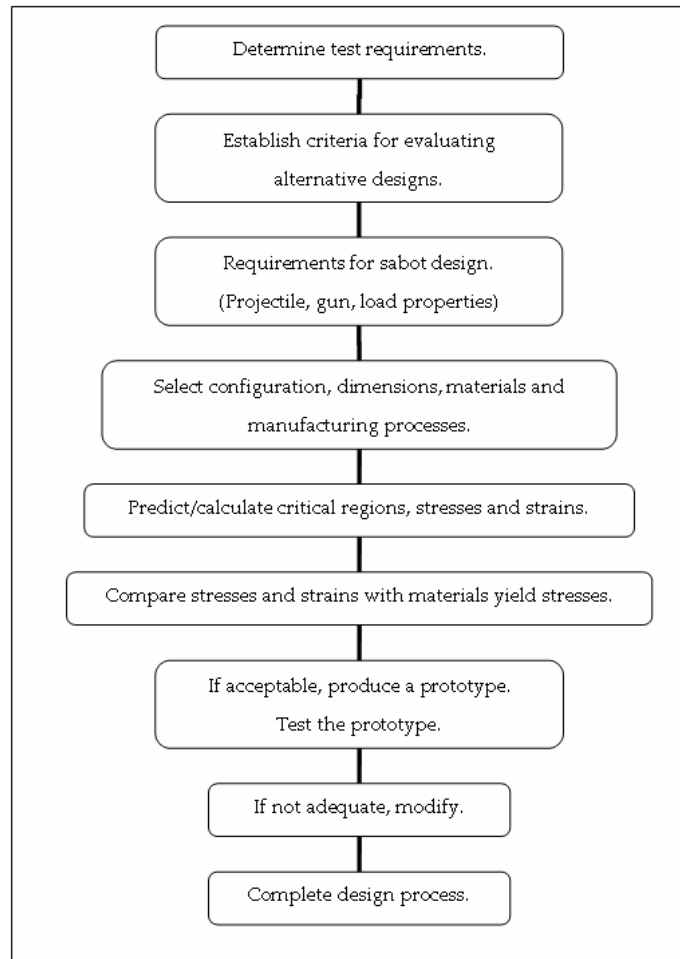


**Figure 11** Design flowchart

## 2.2 STRUCTURAL ANALYSIS OF SABOTS

To start the structural analysis, first of all, assumptions should be stated. Then structurally critical regions and loading types on these regions should be determined. In the following sections these analysis steps are explained.

### 2.2.1 Assumptions and Limitations

A model is placed in a gun with its sabot. Gun powder is calculated for the desired muzzle velocity and placed in the chamber behind the model-sabot package. After firing the gun, package accelerates in the gun barrel, travels through the gun tube. This is the first stage of the package journey. At the end of the barrel the package exits from the muzzle and second stage begins. In this stage the package starts to decelerate. Only aerodynamic and gravitational forces act on the package. Pushing forces behind the package and constraint forces on the sabot walls from the barrel (barrel holds the sabot walls and prevents them to separate) disappears. In this study, design processes include the first stage which is the in-bore motion of the package.

Even though the temperature in the barrel is high due to the explosion of the gunpowder, temperature effects on the stress analysis are ignored. Package is exposed to hot air for very short time period around 8 milliseconds. Only back face gets hot because this region is directly subjected to hot air. On the other hand, front region, which includes model and sabot walls, travels through the fresh air. Therefore, the material selection criterion for the pusher is important from this point of view.

Since inertial forces are much greater than aerodynamic forces, aerodynamic forces acting on the sabot in the barrel is neglected,

In aeroballistic range testing wide range of models are used. For every different projectile geometry, a new sabot design is needed. Therefore, in this study it is impossible to develop a computer tool including all situations. Thus, it is decided to develop a tool for two different sabot geometries based on pusher type. Sabot designs in FML are made for common models of the rockets. As a result, sabot design is done for axially constant radius models with different physical properties (mass, CG etc.).

Since it is difficult to determine the dynamic effects in the gun bore, in this study stress analysis is treated as a static loading. For initial design it is not a must to consider the dynamic effects [4].

According to these assumptions, structural analysis seems oversimplified. By using past design experiences, and with some trials a successful design can be achieved, so it is not necessary to make the design process complicated. Loading on the sabot can be treated as impact loading since loading time is very short. Also true nature of the loads acting on the sabot and model during gun tube travel and dynamic material properties is not conclusively known [4]. Therefore, using static material properties are conservative and satisfactory [7].

### **2.2.2 Sabot Separation**

As it is mentioned in the previous sections, separation of the sabot from the model is very important. Sabot design process should also cover separation subject. On the other hand, to discover the separation properties and optimum aerodynamic geometry (nose angle, rear geometry etc.) for new sabot geometry, CFD analysis is needed. CFD analysis should be done for a separating sabot wall after exiting the gun during its free flight. Modeling the sabot during its motion is very difficult and it takes very long time, because unsteady analysis with moving mesh should be performed. CFD analysis for this case is by itself a new work. From the literature survey it is seen that discard analysis is also done by detailed aerodynamic calculations, and angles on the sabot and outer shape of the sabot are modified after these analysis. Empirical formulas are not available for these analyses.

Scope of this thesis study covers only structural design in gun bore travel stage. Therefore, detailed separation analysis during free flight is not considered. If conventional sabot front face is used, separation is unavoidable. For generally used conventional sabots, it is seen from researches that, 45 degrees nose angle is used. Therefore, nose angle of the sabot walls is taken as 45 degrees in this study.

According to test experiences, with 45 degrees nose angle, sabot walls separate because of drag force and separation distance is short enough to let the model enter alone into the test section.

If improvement is needed for the designed sabot, separation analyses can be performed and from these results nose angle can be changed.

### **2.2.3 Sabot Configurations**

As mentioned in the previous section, in FML tests pusher type sabot configuration is used. The models used usually have smooth body surface, therefore ring sabot can not be used. In addition, production of ring or complicated sabot geometries is more difficult.

Therefore, it is decided to design pusher type of sabots. There is a conventional pusher type which is always used in FML tests (Figure 12). Production of this type is very easy and it seems to be a satisfactory type. But it is not resistant to high speeds. Therefore, a need for new sabot geometry appears.

In the next sections stress analysis will be done for two different sabots. Conventional sabot will be called as Sabot-1 and new type will be called as Sabot-2.

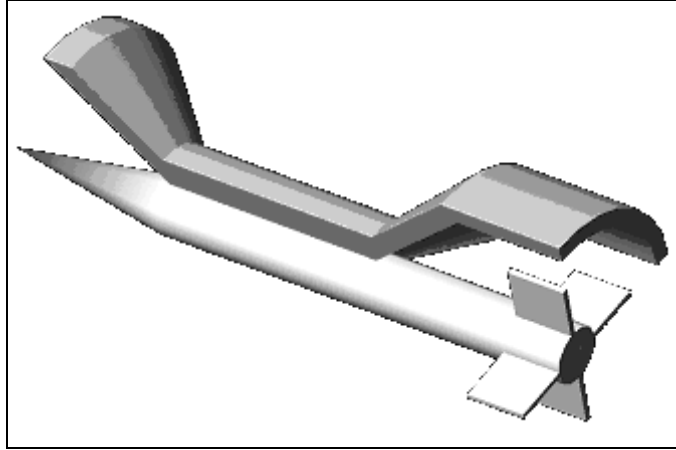


**Figure 12** 3D view of Sabot-1

#### **2.2.4 Forces Acting on Sabot-1 and Critical Regions**

The only force that accelerates the sabot-projectile package is the pressurized gases in the combustion chamber. First external force is the pressure acting to the back face of the pusher. Second external force is the friction force. Contact surface is between the sabot and the gun tube. Sabots are produced with smaller radius than the gun tube. The aim of this technique is to reduce the friction force. 0.5 mm smaller radius is enough for reducing the friction. If the sabot diameter is smaller than the given value, sabot will not align the projectile in the bore and during the gun tube travel some collisions may occur. This smaller radius production is applied to both sabot walls and front region of the pusher. But the rear periphery of the pusher must have little larger radius as mentioned in the previous sections. For the sabot walls, the friction force is negligible when compared with inertial loads, since normal force is the total weight of the sabot-projectile package. On the other hand, the pusher part fits in the gun tightly and after firing, larger radius part plastically deforms and provides sealing (Figure 13). The friction force in this region should be taken into consideration.

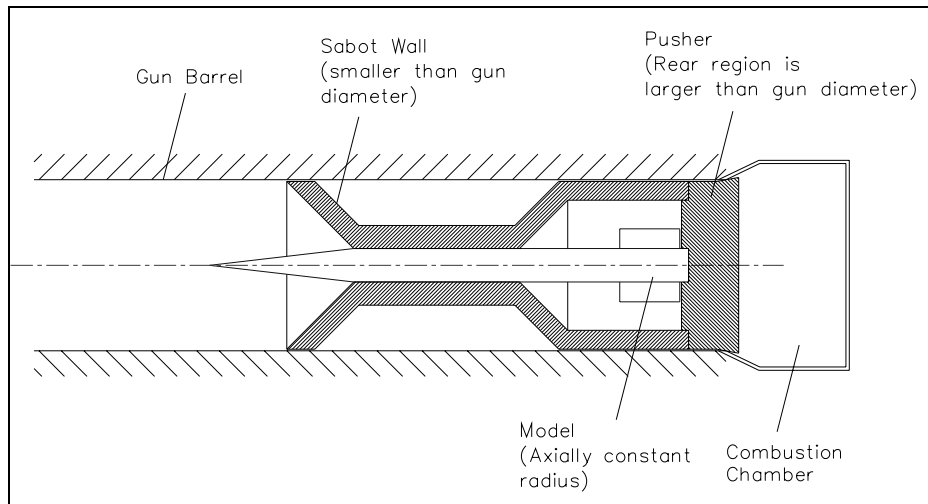


**Figure 13** Sabot-1 and projectile layout

Since friction force and pressure behind the sabot are the only external forces acting on the system (Figure 14), acceleration of the whole system can be calculated easily. Formulation for calculating the acceleration will be discussed in Chapter 3. Thus, with a known acceleration, stress analysis can be applied to critical regions of the sabot [3]. Load at any section of the sabot is equal to the load to accelerate the mass ahead of that section.

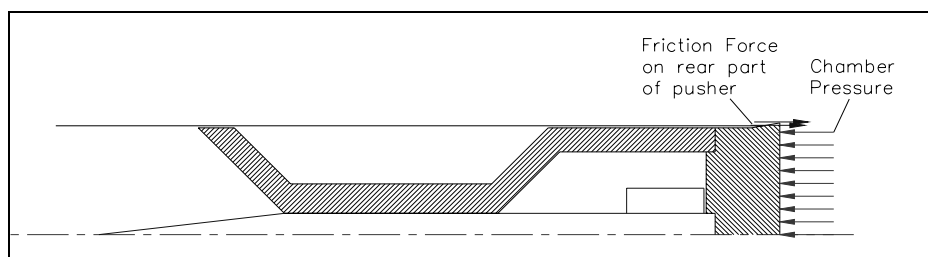


**Figure 14** Forces acting on sabot

Friction force does not act to whole side surface of the pusher; it acts only on the rear part of the pusher (Figure 15). While the pusher tightens in the gun tube, it

plastically deforms just at the beginning of the travel. This event causes stress intensity around a local area.

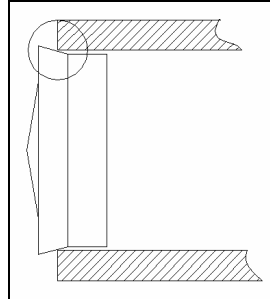


**Figure 15** Obturation

At the rest of the report, sabot will be investigated in two parts; sabot walls and pusher. Sabot wall will be called as sabot shortly.

The forces acting on the pusher are the sabot and model reaction forces and chamber pressure. During acceleration, sabot and model weight rests on the pusher. In Figure 16, forces mentioned above can be seen on the free body diagram. Since the system is axially symmetric, only the half part is drawn.

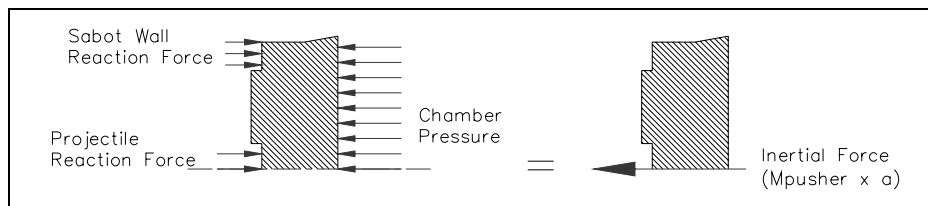


**Figure 16** Free body diagram of pusher

Pressure is assumed to be distributed on the back face of the pusher uniformly in the direction of motion. Because of the system acceleration, inertial force of the model acts on a region with a diameter equal to the model diameter. This inertial force is in the opposite direction of the motion. Therefore, it is expected that pusher would bend. Thus, it is important to calculate the radial stress at center and on the top face of the pusher. In addition to bending, inertial force of the model causes shear in the pusher material. In determination of thickness of the pusher, these two failure mechanisms should be taken into account (Figure 17).

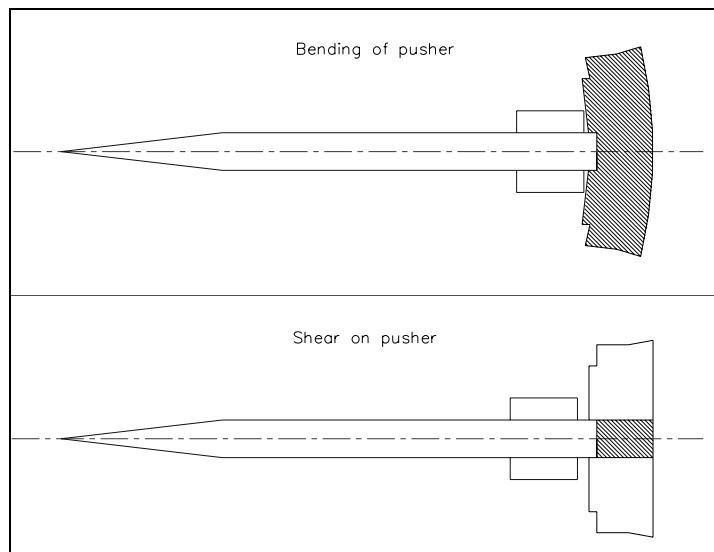


**Figure 17** Pusher deformation

Sabot travels in the gun by the help of the pusher. The only axial force on the sabot is the external force at the interaction surface between the pusher and sabot. Free body diagram of the sabot is given in the following figure (Figure 18). This force at the contact face equals to inertial force acting on the whole sabot mass. Since the force is distributed and mass dependent, load is higher at the rear part of the sabot.

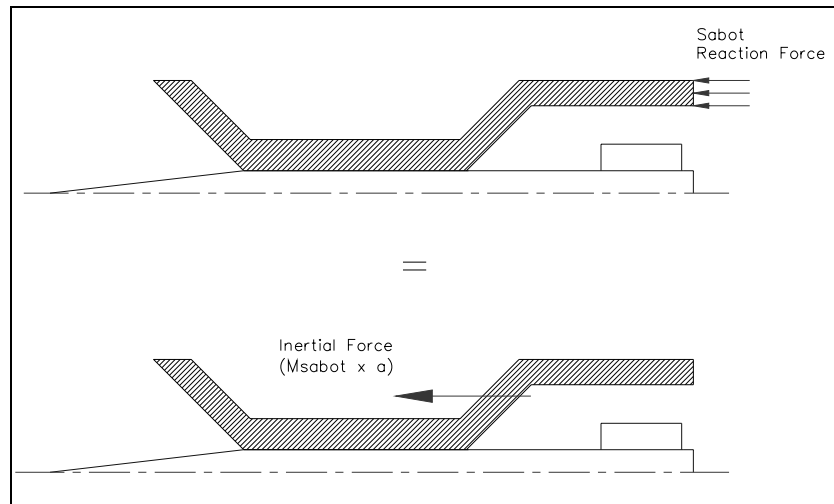


**Figure 18** Free body diagram of sabot

Motion of the sabot-model package is only in the gun bore's axial direction and gun bore restricts the motion in other directions. Therefore, between sabot and model there is no external force. Reaction force between sabot and model starts to appear when sabot tends to deform because of inertial loading. Since reaction force acting on model due to deformation tendency of sabot in radial direction is axially symmetric, model can be assumed as a rigid structure which is located exactly at the axis of the gun. Inbore view of the sabot-model package is given in Figure 19.

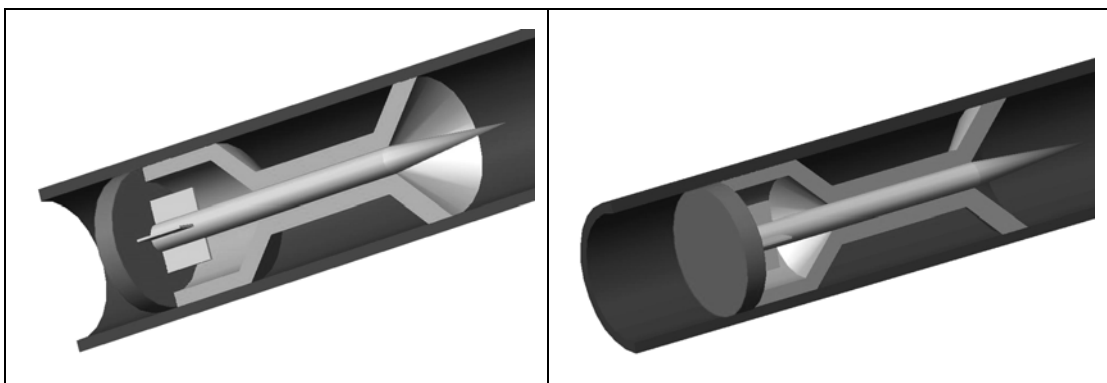


**Figure 19** Package inbore view

In Figure 21, structurally critical regions of the sabot are shown. At the nose part (inclined surface at the front) because of mass of that part, inertial force causes moment and bending. Stress will be high at the intersection of inclined surface (section-1) and the part which is parallel to model (section-2). Shear stress in that region will be very low since nose part is very light and as a result inertial force is not high. In section-2, axial force causes compression stress and since this section is long, buckling may occur. Section-3 is the most important part. This part is located at the rear part of the sabot; most of the sabot mass is in the front of that section. In addition, because of moment arm between section-2 and section-4, both bending and shear is dominant. Considering only compression stress at section-4 will be sufficient. Bending at section-4 is not possible because due to finite element analysis, section-3 pushes the section-4 in outward direction (upward) under inertial loading and section-4 is in contact with gun wall. Figure 20 is the displacement counter plot of sabot-model package in 'y' direction (radial). In this figure, it is seen that section-4 has orange to yellow color scatter and from the displacement scale these colors refer to positive (outward) displacement.

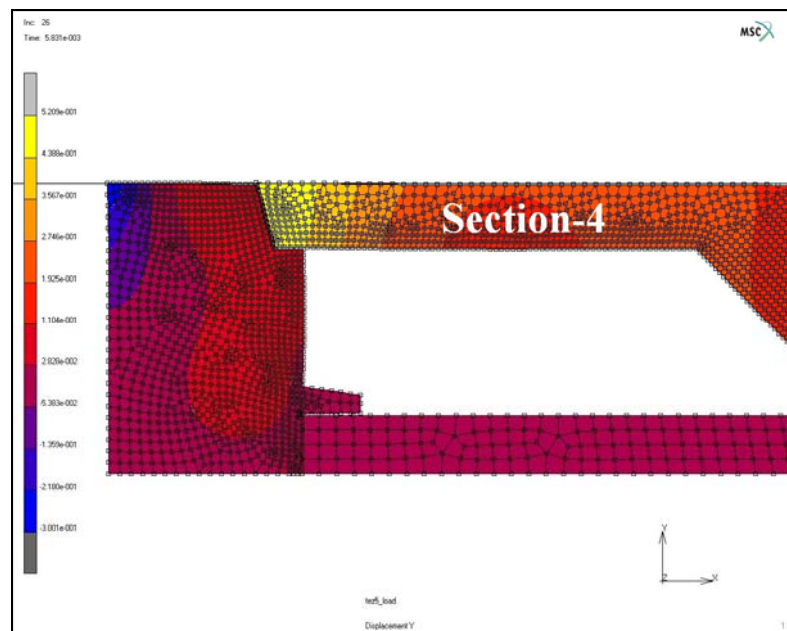


**Figure 20** y-displacement of Sabot-1

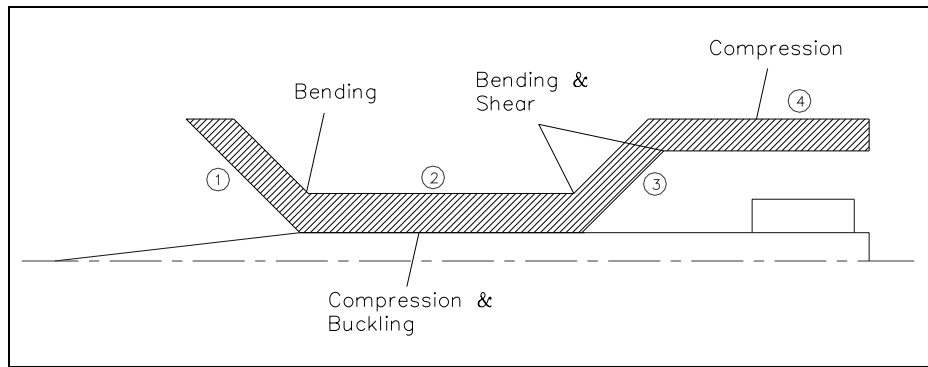


**Figure 21** Critical regions for sabot

### 2.2.5 Conceptual Design of Sabot-2

Sabot-1 is the conventional design for aeroballistic range testing. In FML tests, maximum muzzle velocity that has been reached is around Mach 2. Most of the time, sabot failure imposes a restriction on the maximum velocity that can be reached. For high velocity tests, there was a demand for a new sabot that can resist loadings due to high accelerations.

Critical regions of Sabot-1 were mentioned in the previous section. From the experiences gathered, critical region is the intersection part of 3 and 2. Since the structure is inclined and has eccentricity in that region, compression force turns out to be a bending force. Therefore, designers should avoid eccentricity in the structure, which increases the stresses, and in turn causes combined loading.

For high speed kinetic energy projectiles, there are several launch dynamics studies in the literature. Sabots used for these projectiles are ring sabots. Inclined nose profile causes drag and the main force for separation is the drag force acting on the nose part. The most common modern type of kinetic energy projectile is known as “armour-piercing fin-stabilized discarding sabot (APFSDS)” (Figure 22). This KE projectile sabot has another pocket located around the CG of the projectile (Figure

23). Actually, function of this pocket is to seal the gases, and this part also pulls the projectile. On the other hand, during separation this part acts as drag generator and makes the separation easier.

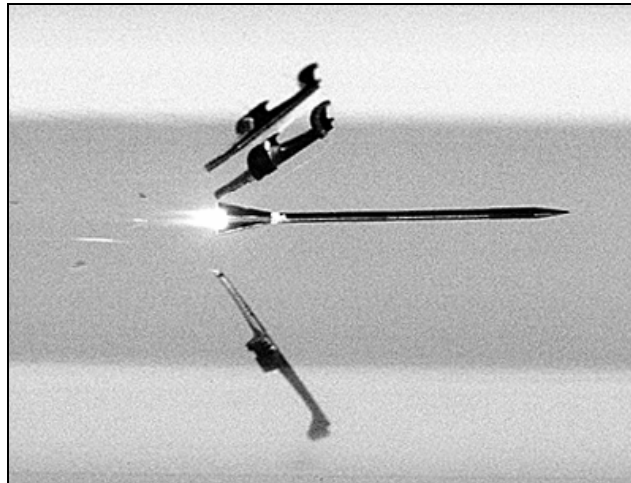


**Figure 22** APFSDS

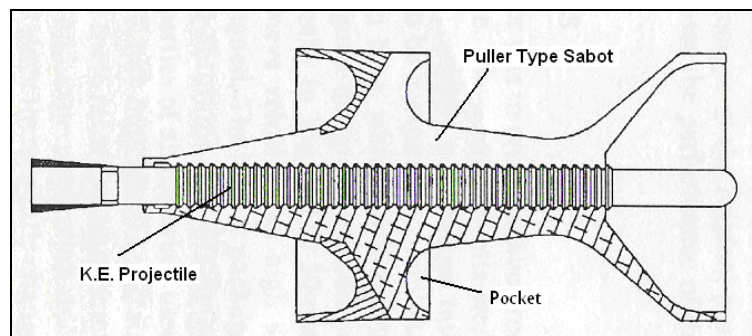


**Figure 23** KE Projectile sabot

To summarize, three main separation mechanisms exist for these projectiles. First one is the drag force caused separation as mentioned above. Second mechanism is the lift separation produced by the presence of the rear and middle pocket. Third

mechanism is generated using rear separation, in the initial opening stage, by the use of the rear pocket (Figure 24) [8].

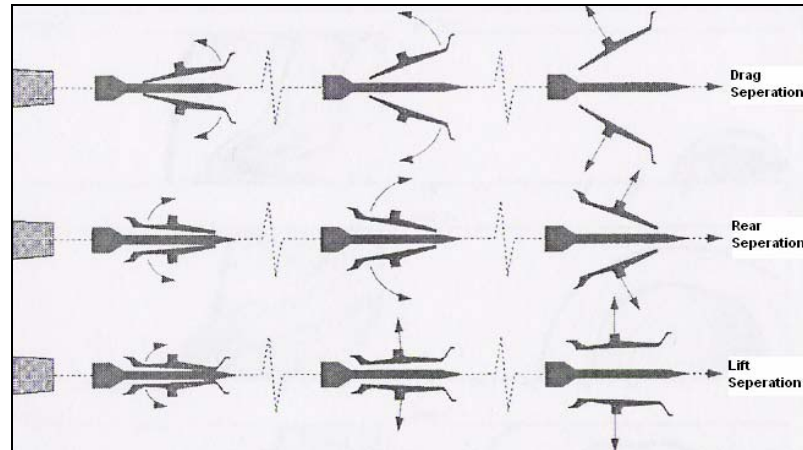


**Figure 24** Separation Mechanisms

A relation is established for the separation mechanism between pusher type and ring sabot. It is obvious that the new sabot geometry will be similar to drag separation concept. Because of high stresses at geometries like section-3 of Sabot-1 and eccentricity based problems, rear pocket will be risky. Since drag separation is the main mechanism, CG location is very important; sabot pitches up about its CG location. On the other hand, the only force is not drag force acting on the sabot. There is also aerodynamic normal force due to pressure distribution on the surface of the sabot and according to the following geometry total normal force is usually in the downward direction. In other words this type of geometries can not generate opening force by resultant aerodynamic normal force. But from the CFD analysis, it has been observed that drag force is several times larger than normal force [9]. If sabot CG is closer to the centerline of the projectile, because of higher moment arm, separation will be easier (Figure 25).

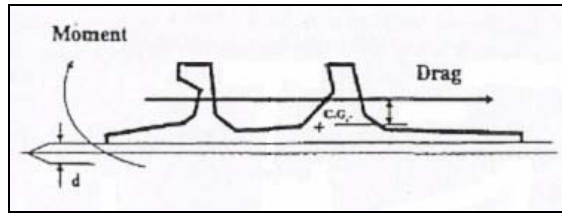


**Figure 25** Drag force acting on sabot

From the reasons mentioned in the above paragraphs Sabot-2 geometry is designed as in the Figure 26. By this way, sabot geometry looks like kinetic energy projectile sabot with pusher.

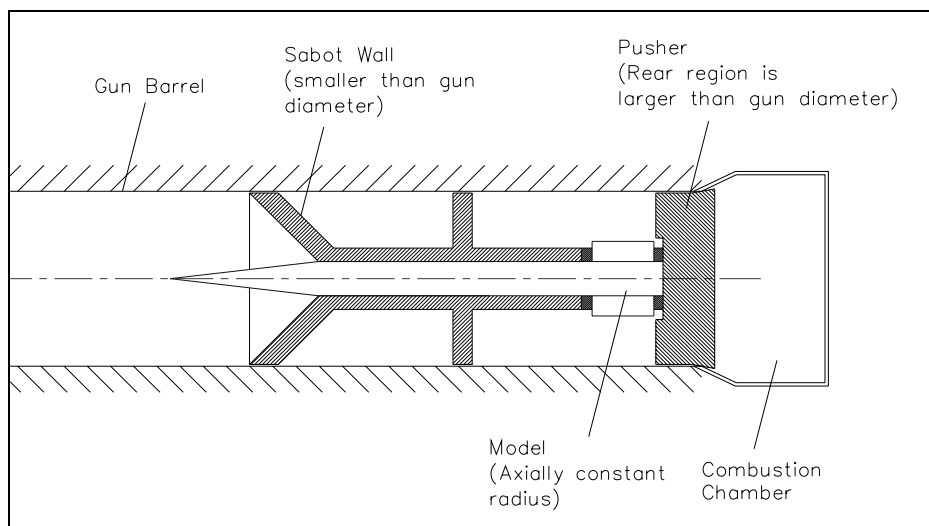


**Figure 26** Sabot-2 geometry

Projectiles have usually four fins. Sabots are composed of four sabot walls. As seen in Figure 26, since new sabot lies down on the whole length of the projectile, fins and sabot coincide at rear region of the sabot. This problem is solved by making cavities for fins on the aft region of the sabot parts. In other words, each part is 90 degrees, because sabot is divided into four parts equally. Because of the cavities,

rear section of the sabot parts is slim and the angle between the sabot walls is slightly less than 90 degrees (Figure 27).

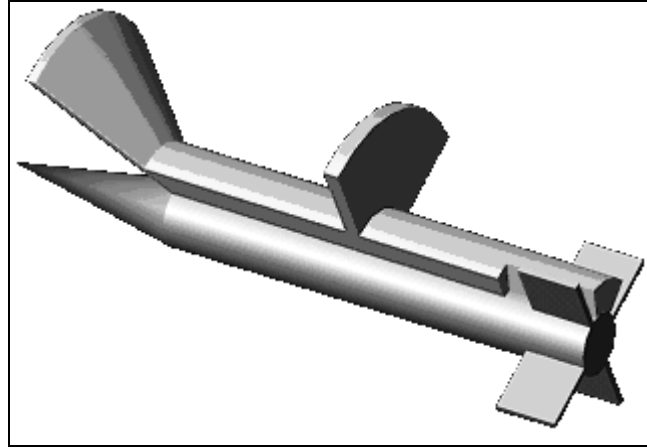


**Figure 27** 3D View of Sabot-2

When Sabot-1 and Sabot-2 is compared with each other, it is expected that Sabot-2 is lighter and tougher than Sabot-1 because of different aft geometry which has smaller diameter. In addition, CG location of Sabot-2 is closer to the projectile and this makes it easier for Sabot-2 to separate.

### **2.2.6 Forces Acting on Sabot-2 and Critical Regions**

Pusher of Sabot-2 has the same obturation principle as Sabot-1. Since aft periphery is larger than the gun diameter, friction force is the only external force besides the base pressure (Figure 28).

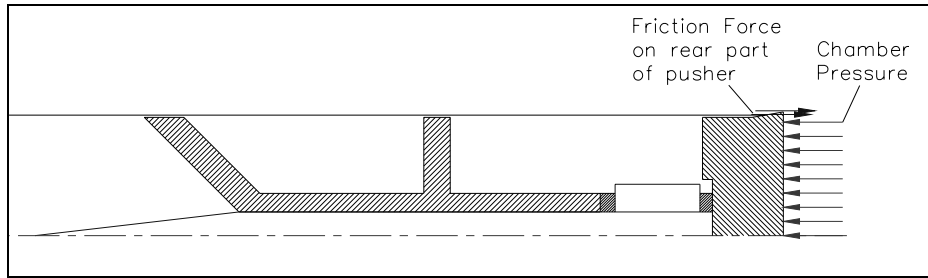


**Figure 28** Forces acting on Sabot-2

When pusher and sabot interaction is investigated, when compared to Sabot-1, it is obvious that the only difference is the application region of the sabot reaction force. This force is closer to the center of the pusher in this case (Figure 29). Similar to the Sabot-1 shear and bending are the critical stress generators.

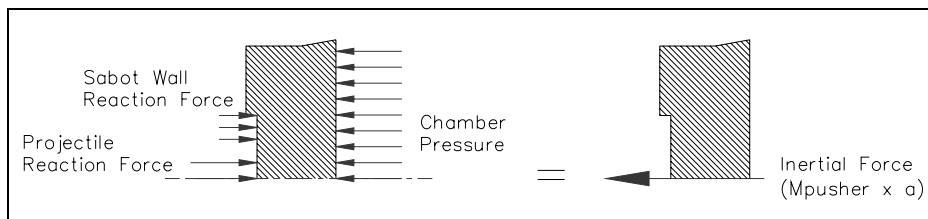


**Figure 29** Free body diagram of Sabot-2 pusher

Section-1 and section-2 of the Sabot-2 have same geometry with the Sabot-1. Therefore, failure mechanisms are same. Because of existence of section-3, inertial force causes bending moment, and stress is high at the intersection of section-3 and section-4. When the force that causes bending is compared with Sabot-1, it can be seen that it is less on Sabot-2. Section-3 of Sabot-2 is lighter than the part in front of the section-3 of Sabot-1 (Figure 30). Section-2 and section-4 have only compression force on them. This compression force may cause buckling which will be investigated in the next sections. Section-4 has more compression force; because total weight in front of that section is heavier.

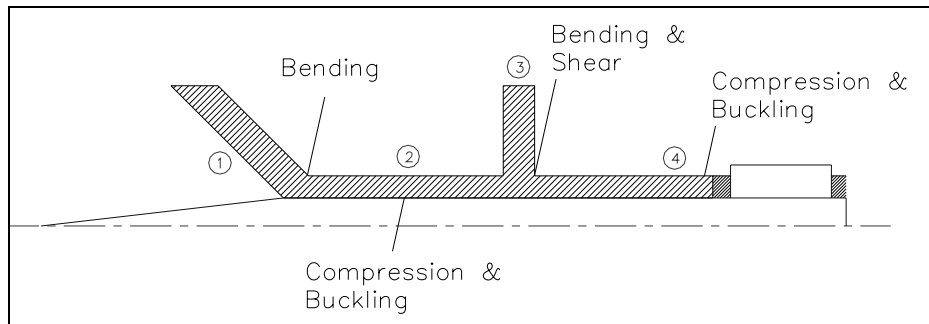


**Figure 30** Critical regions for Sabot-2

## 2.3 STRESS FORMULATIONS

After the acting forces on the critical regions are determined, formulas and relations to calculate the stresses should be derived. In the following sections, these relations for sabots and pushers are derived separately and analysis principles are explained.

### 2.3.1. Derivation of Stress Relations for the Pusher

Set back forces of the sabot and projectile acting on the pusher causes bending on the pusher. Figure 16 and Figure 29 shows the forces acting on the pusher types. To calculate the stresses on the pusher, appropriate stress relations has to be derived. Stress and deformation on the pusher will be axisymmetric, and a cylindrical coordinate system would be proper to use for the analysis [3].

Previous sabot productions show that pusher is a thick circular plate. Criterion for thin plate assumption is valid for a thickness to diameter ratio of less than 1/20 [10]. Thickness to span length ratio of a pusher is generally around 1/3. Therefore, thin plate theory assumption can not be made.

The fundamental assumptions for thin plate theory, known as Kirchhoff hypotheses, can be stated as follows [10];

- 1) The deflection of the midsurface is small compared with the thickness of the plate. The slope of the surface is very small and square of the slope is negligible.
- 2) The midplane remains unstrained subsequent to bending.
- 3) Plane sections initially normal to the midsurface remain plane and normal to that surface after bending. In other words the transverse shear strains  $\sigma_{rz}$  and  $\sigma_{\theta z}$  are negligible.
- 4) The stresses normal to midplane,  $\sigma_z$  is small compared with the other stress components and may be neglected.

For thick plates, assumptions 3 and 4 are not suitable, since shear stresses can not be neglected. Therefore, for pusher stress analysis stress components  $\sigma_r$ ,  $\sigma_\theta$ ,  $\sigma_z$  and  $\sigma_{rz}$  should be determined.

Strain-displacement relations in cylindrical coordinates for axisymmetric loading problems, where  $v = 0$  and  $\frac{\partial}{\partial \theta} = 0$ , are given as;

$$\begin{aligned} \epsilon_r &= \frac{\partial u}{\partial r} & \epsilon_z &= \frac{\partial w}{\partial z} \\ \epsilon_\theta &= \frac{u}{r} & \gamma_{rz} &= \frac{\partial u}{\partial z} + \frac{\partial w}{\partial r} \end{aligned} \quad (1)$$

For axisymmetric loading problems, stress components are independent of  $\theta$  and therefore  $\sigma_{r\theta}$  and  $\sigma_{\theta z}$  components are zero. Thus, equilibrium equations reduce to;

$$\begin{aligned}\frac{\partial \sigma_r}{\partial r} + \frac{\partial \sigma_{rz}}{\partial z} + \frac{\sigma_r - \sigma_\theta}{r} &= 0 \\ \frac{\partial \sigma_{rz}}{\partial r} + \frac{\partial \sigma_z}{\partial z} + \frac{\sigma_{rz}}{r} &= 0\end{aligned}\quad (2)$$

Determination of stress components  $\sigma_z$  and  $\sigma_{rz}$  will be performed using stress functions. Introducing a stress function  $\phi$  will bring an advantage. It may be verified that Equation (2) is satisfied if stress components are taken as [11];

$$\begin{aligned}\sigma_r &= \frac{\partial}{\partial z} \left( \nu \nabla^2 \phi - \frac{\partial^2 \phi}{\partial r^2} \right) \\ \sigma_\theta &= \frac{\partial}{\partial z} \left( \nu \nabla^2 \phi - \frac{1}{r} \frac{\partial \phi}{\partial r} \right) \\ \sigma_z &= \frac{\partial}{\partial z} \left[ (2 - \nu) \nabla^2 \phi - \frac{\partial^2 \phi}{\partial z^2} \right] \\ \sigma_{rz} &= \frac{\partial}{\partial r} \left[ (1 - \nu) \nabla^2 \phi - \frac{\partial^2 \phi}{\partial z^2} \right]\end{aligned}\quad (3)$$

In addition, stress function  $\phi$  must satisfy strain-compatibility equation which is;

$$\left( \frac{\partial^2}{\partial r^2} + \frac{1}{r} \frac{\partial}{\partial r} + \frac{\partial^2}{\partial z^2} \right) \left( \frac{\partial^2 \phi}{\partial r^2} + \frac{1}{r} \frac{\partial \phi}{\partial r} + \frac{\partial^2 \phi}{\partial z^2} \right) = \nabla^2 \nabla^2 \phi = 0 \quad (4)$$

Displacement 'u' can be written as;

$$u = r\varepsilon_\theta = \frac{r}{E} [\sigma_\theta - \nu(\sigma_r + \sigma_z)] = -\frac{1+\nu}{E} \frac{\partial^2 \phi}{\partial r \partial z} \quad (5)$$

Derivation of displacement in z-direction can be started by writing the strain in terms of function  $\phi$ ;

$$\frac{\partial w}{\partial z} = \varepsilon_z = \frac{1}{E} [\sigma_z - \nu(\sigma_r + \sigma_\theta)] = \frac{1}{E} \frac{\partial}{\partial z} \left[ 2(1-\nu^2) \nabla^2 \phi - (1+\nu) \frac{\partial^2 \phi}{\partial z^2} \right] \quad (6)$$

After integrating the Equation (6), 'w' is obtained as;

$$w = \frac{1}{E} (1+\nu) \left[ 2(1-\nu) \nabla^2 \phi - \frac{\partial^2 \phi}{\partial z^2} \right] + f(r) \quad (7)$$

where  $f(r)$  is arbitrary and a function of 'r'. 'w' can also be obtained by using the expression for  $\sigma_{rz}$  and  $\gamma_{rz}$  in the relation  $\sigma_{rz} = G\gamma_{rz}$  where  $E = 2(1+\nu)G$ .

$$w = \frac{1}{E} (1+\nu) \left[ 2(1-\nu) \nabla^2 \phi - \frac{\partial^2 \phi}{\partial z^2} \right] + g(z) \quad (8)$$

where  $g(z)$  is arbitrary and function of z. Since Equation (7) and Equation (8) must be equal,  $f(r)$  and  $g(z)$  should be identical at all points. Therefore,  $f(r) = g(z) = A$  and 'A' is a constant, corresponds to an axial rigid body translation and can be restored when a fixity condition is needed.

If a function  $\phi$  can be defined satisfying Equation (4) and boundary conditions; displacements ‘u’ and ‘w’, strains and stress can be obtained. To solve this problem, using polar coordinates R and  $\Psi$  would be appropriate (Figure 31).

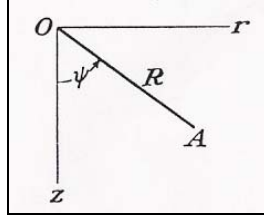


**Figure 31** Polar coordinate system

By using polar coordinate system, Equation (4) can be written as;

$$\nabla^4 \phi = 0 = \left( \frac{\partial^2}{\partial R^2} + \frac{2}{R} \frac{\partial}{\partial R} + \frac{1}{R^2} \cot \Psi \frac{\partial}{\partial \Psi} + \frac{1}{R^2} \frac{\partial^2}{\partial \Psi^2} \right) \cdot \left( \frac{\partial^2 \phi}{\partial R^2} + \frac{2}{R} \frac{\partial \phi}{\partial R} + \frac{1}{R^2} \cot \Psi \frac{\partial \phi}{\partial \Psi} + \frac{1}{R^2} \frac{\partial^2 \phi}{\partial \Psi^2} \right) \quad (9)$$

The rest of the derivation procedure is related with Equation (9). The solution can be obtained by polynomial solution of Legendre’s equation which is given in detail in Reference [11].

When the function  $\phi$  is taken as sixth power polynomial form, solution for uniformly loaded circular plate can be obtained (Figure 32).

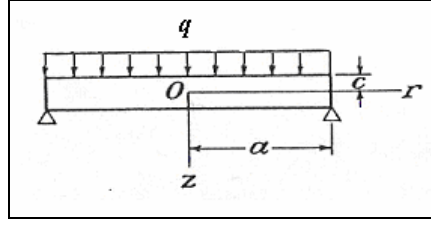


**Figure 32** Simply supported circular plate

Stress function for simply supported uniformly loaded circular plate is given as [11];

$$\phi = \frac{1}{3} a_6 (16z^6 - 120z^4r^2 + 90z^2r^4 - 5r^6) + b_6 (8z^6 - 16z^4r^2 - 21z^2r^4 + 3r^6) \quad (10)$$

Subscripts of the constants in the formulas show the power of the polynomial used. Substituting  $\phi$  in Equation (3) and adding terms which are derived from third and fourth order polynomial, stress definitions turn out to be [11];

$$\begin{aligned} \sigma_r &= a_6 (320z^3 - 720r^2z) + b_6 \{ 64(2 + 11\nu)z^3 \\ &\quad + [504 - 1056\nu]r^2z \} + 96a_4z \\ \sigma_z &= a_6 (-640z^3 + 960r^2z) + b_6 \{ [-960 + 704(2 - \nu)]z^3 \\ &\quad + [384 - 1056(2 - \nu)]r^2z \} - 192a_4z - \frac{q}{2} \\ \sigma_{rz} &= a_6 (960rz^2 - 240r^3) + b_6 \{ [-672 + 1056\nu]z^2r \\ &\quad + [432 - 264\nu]r^3 \} + 96a_4r \end{aligned} \quad (11)$$

Here 'q' is the intensity of the uniform loading and 2c is the thickness of the plate.  $-q/2$  term in  $\sigma_z$  term comes from the third power polynomial solution, and  $b_4$  which comes from fourth order polynomial is zero [11]. Three constants  $a_6$ ,  $b_6$  and  $a_4$  can be obtained by using boundary conditions. Stresses should satisfy the upper and lower surface boundary conditions.

$$\text{For } z = c \quad \sigma_z = 0$$

$$\sigma_{rz} = 0$$

$$\text{For } z = -c \quad \sigma_z = -q$$

$$\sigma_{rz} = 0$$

Constants that satisfy the boundary conditions are derived as;

$$a_4 = -\frac{q}{256c} \quad a_6 = \frac{q(18-11\nu)}{28160c^3} \quad b_6 = \frac{q}{2816c^3} \quad (12)$$

When constants are substituted into the stress definitions, they become;

$$\begin{aligned} \sigma_r &= q \left[ \frac{2+\nu}{8} \frac{z^3}{c^3} - \frac{3(3+\nu)}{32} \frac{r^2 z}{c^3} - \frac{3z}{8c} \right] \\ \sigma_z &= q \left( -\frac{z^3}{4c^3} + \frac{3z}{4c} - \frac{1}{2} \right) \\ \sigma_{rz} &= -\frac{3qr}{8c^3} (c^2 - z^2) \end{aligned} \quad (13)$$

The radial stress  $\sigma_r$  is an odd function of z, thus it gives bending moment which is distributed uniformly along the boundary. To get the solution for simply supported circular plate, this stress expression should be deprived from the bending moment

by applying Equation (14). Fourth order polynomial solution of the function  $\varphi$  represents pure bending of the plate by moments uniformly distributed along the boundary (Equation (15)) [11].

$$\int_{-c}^c \sigma_r z dz = 0 \quad (14)$$

$$\sigma_r = 28(1 + \nu)b_4 z \quad (15)$$

Equation (15) is added to radial stress expression given in Equation (13). Resultant radial stress is substituted into the Equation (14) and constant  $b_4$  is obtained for radial stress at  $r=a$ . This solution condition is different from the solution of Equation (11). This term also comes from the fourth order polynomial solution but subscript 4 has already been used. Therefore, constant  $b_4$  in Equation (15) will be called as  $b_5$  and derived as;

$$b_5 = \frac{q}{28(1 + \nu)} \left[ \frac{3}{40} \frac{3 - \nu}{c} + \frac{3}{32} \frac{(3 + \nu)a^2}{c^3} \right] \quad (16)$$

Corresponding constant satisfying the fourth power polynomial solution with  $b_5$  is  $a_5$ ;

$$a_5 = b_5 \frac{(16 - 14\nu)}{48} \quad (17)$$

As mentioned in the previous paragraph  $-q/2$  term comes from the third power polynomial solution. It is assumed that  $\sigma_z = -q/2$  and other stress components are zero. Constants of third power polynomial satisfying these conditions are obtained as following;

$$a_3 = -q \frac{(1-5\nu)}{(60+60\nu)} \quad b_3 = -q \frac{1}{(20+20\nu)} \quad (18)$$

Finally governing function  $\phi$  for the uniformly loaded simply supported circular plate can be determined as;

$$\begin{aligned} \phi = & \frac{1}{3} a_6 (16z^6 - 120z^4r^2 + 90z^2r^4 - 5r^6) + b_6 (8z^6 - 16z^4r^2 \\ & - 21z^2r^4 + 3r^6) + a_4 (8z^4 - 24z^2r^2 + 3r^4) + a_5 (8z^4 - 24z^2r^2 + 3r^4) \\ & + b_5 (2z^4 + z^2r^2 - r^4) + a_3 (2z^3 - 3zr^2) + b_3 (zr^2 + z^3) \end{aligned} \quad (19)$$

When Equation (19) is inserted into Equations (3) and (7), final expressions for thick plate stress components and deflection 'w' becomes;

$$\begin{aligned}
\sigma_{\text{r exact}} &= q \left[ \frac{2+\nu}{8} \frac{z^3}{c^3} - \frac{3(3+\nu)}{32} \frac{r^2 z}{c^3} - \frac{3(2+\nu)}{8} \frac{z}{5c} + \frac{3(3+\nu)}{32} \frac{a^2 z}{c^3} \right] \\
\sigma_{\theta \text{ exact}} &= q \left[ \frac{9+3\nu}{32} \frac{z a^2}{c^3} - \frac{(3+9\nu)}{32} \frac{r^2 z}{c^3} - \frac{6+3\nu}{40c} + \frac{(2+\nu)}{8} \frac{z^3}{c^3} \right] \\
\sigma_z &= q \left( -\frac{z^3}{4c^3} + \frac{3z}{4c} - \frac{1}{2} \right) \\
\sigma_{rz} &= -\frac{3qr}{8c^3} (c^2 - z^2) \\
w &= \frac{q}{640} \frac{1}{Ec^3} \left( -24c^2 r^2 \nu - 180a^2 z^2 \nu - 60a^2 \nu^2 z^2 + 120\nu r^2 z^2 \right. \\
&\quad + 30a^2 \nu^2 r^2 + 48c^2 \nu^2 z^2 - 24c^2 \nu^2 r^2 + 60a^2 \nu r^2 + 96c^2 \nu z^2 \\
&\quad + 120r^2 \nu^2 z^2 - 40z^4 + 15r^4 - 320zc^3 - 80\nu z^4 - 40\nu^2 z^4 - 15\nu^2 r^4 \\
&\quad \left. + 240c^2 z^2 - 192r^2 c^2 - 90a^2 r^2 \right) + A
\end{aligned} \tag{20}$$

As mentioned in the previous paragraphs constant ‘A’ comes from axial rigid body translation. This constant equals to value of ‘w’ at r=a and when ‘A’ is zero.

Radial stress component for the thick plate is difficult to use because of long complicated terms. It is not necessary to derive an appropriate relation for non-uniform loading situation within the scope of this study. Instead of deriving complicated relations, a relation can be obtained between thin and thick plate for uniform loading. This relation can then be used with known thin plate non-uniform formulation to get approximate thick plate non-uniform loading solution. To find a general relation between thin plate radial stress and thick plate radial stress, stresses are calculated at different arbitrary pressure values and thicknesses for a 100 mm (equals to the gun diameter) diameter circular plate. Results are shown in Table 1. Thin plate stress components are given in Equation (21) [9].

$$\sigma_r = \frac{3qz}{4t^3}(3 + \nu)(a^2 - r^2) \quad (21)$$

$$\sigma_\theta = \frac{3qz}{4t^3}[(3 + \nu)a^2 - (1 + 3\nu)r^2]$$

In Table 1, stresses are calculated at  $r=0$  where maximum radial stress is achieved, at  $z=t/2=c$  where 't' is the thickness of the plate. The found relation is called as 'y'. Equation (22) is the definition of 'y'. For the same plate thickness, value of 'y' does not change with different pressure values. Therefore, an equation can be derived for 'y' and thickness of a plate.

$$y = \frac{(\text{thick} - \text{thin})}{\text{thin}} 100 \quad (22)$$

**Table 1** Thin Plate and Thick Plate Results

Thickness (m)	P=5e6 Pa			P=7e4 Pa			Average y
	$\sigma_r$ (Pa)		y	$\sigma_r$ (Pa)		y	
	Thin	Thick		Thin	Thick		
1.0E-02	1.59E+08	1.60E+08	0.376	2.22E+06	2.23E+06	0.378	0.377
1.5E-02	7.06E+07	7.12E+07	0.847	9.89E+05	9.97E+05	0.847	0.847
2.5E-02	2.54E+07	2.60E+07	2.350	3.56E+05	3.64E+05	2.350	2.350
3.5E-02	1.30E+07	1.36E+07	4.602	1.82E+05	1.90E+05	4.603	4.603
5.0E-02	6.36E+06	6.95E+06	9.399	8.90E+04	9.74E+04	9.399	9.399
6.0E-02	4.41E+06	5.01E+06	13.536	6.18E+04	7.02E+04	13.536	13.536
8.0E-02	2.48E+06	3.08E+06	24.065	3.48E+04	4.31E+04	24.064	24.064
1.0E-01	1.59E+06	2.19E+06	37.600	2.22E+04	3.06E+04	37.601	37.600

In Figure 33, average value of 'y' which is given in the above table is drawn with respect to plate thickness. When a polynomial line is fitted to the curve equation of 'y' is obtained.

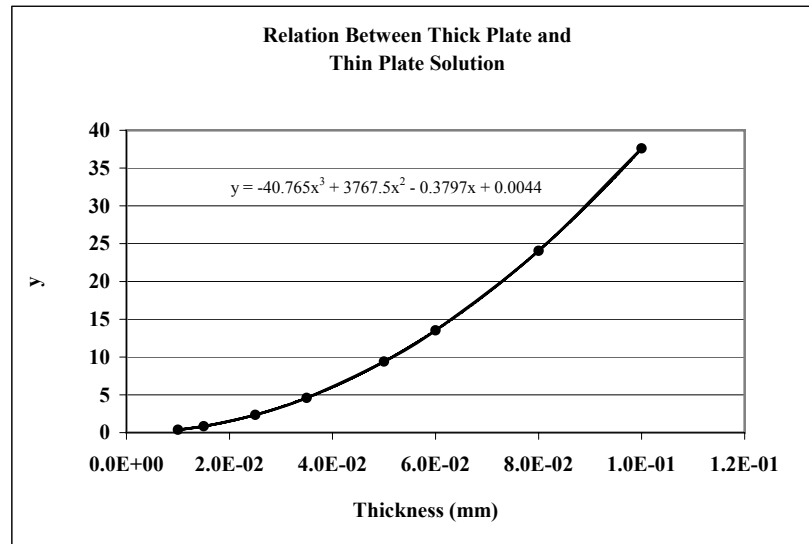


**Figure 33** y vs. thickness plot

For a thick, circular, simply supported plate with uniformly distributed loading, radial stress can be found by using thin plate theory formulation and Equation (23).

$$y = -40.765t^3 + 3767.5t^2 - 0.3797t + 0.0044 \quad (23)$$

Chamber pressure in the gun causes a uniformly distributed load on pusher. A formula was derived for this type of loading. In addition to uniformly distributed load, non-uniform load is applied by the set back force of sabot and projectile. Now it is needed to derive a formula for this type of loading which is suitable for thin plates. Figure 34 shows the general drawing for a typical non-uniform loading.

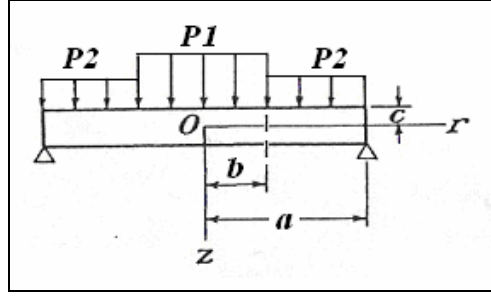


**Figure 34** Non-uniform loading of circular plate

Let circular plate be loaded by a uniform load  $P_1$  over region defined by  $r < b$  and a uniform load  $P_2$  over region defined by  $b < r < a$  as given in Figure 34. Plate is simply supported over the boundary  $r = a$ . In Reference [12], deflection 'w' is given as;

$$\begin{aligned}
 w_1 &= c_0 + c_2 r^2 + \frac{P_1 r^4}{64D} && \text{if } 0 \leq r \leq b \\
 w_2 &= c'_0 + c'_1 \log r + c'_2 r^2 + c'_3 r^2 \log r + \frac{P_2 r^4}{64D} && \text{if } b \leq r \leq a
 \end{aligned} \tag{24}$$

Where  $D = \frac{Et^3}{12(1-\nu^2)}$  and constants are;

$$\begin{aligned}
 c_0 &= \frac{b^2(P_1 - P_2)}{64D} \left[ \frac{4(3+\nu)a^2 - (7+3\nu)b^2}{1+\nu} - 4b^2 \log \frac{a}{b} \right] + \frac{(5+\nu)P_2 a^4}{(1+\nu)64D} \\
 c_2 &= -\frac{b^2(P_1 - P_2)}{8D} \left[ \frac{4a^2 - (1-\nu)b^2}{4(1+\nu)a^2} + \log \frac{a}{b} \right] - \frac{(3+\nu)P_2 a^2}{(1+\nu)32D}
 \end{aligned} \tag{25}$$

$$\begin{aligned}
c'_0 &= \frac{b^2(P1-P2)}{64D} \left[ \frac{2(3+\nu)a^2 - (1-\nu)b^2}{4(1+\nu)} - \frac{b^2}{2} \log a \right] + \frac{(5+\nu)P2a^4}{(1+\nu)64D} \\
c'_1 &= \frac{b^4(P1-P2)}{16D} \\
c'_2 &= -\frac{b^2(P1-P2)}{8D} \left[ \frac{(3+\nu)}{2(1+\nu)} + \log a - \frac{(1-\nu)b^2}{4(1+\nu)a^2} \right] - \frac{(3+\nu)P2a^2}{(1+\nu)32D}
\end{aligned} \tag{26}$$

Radial stress can be calculated by using the following expression and deflection 'w'.

$$\sigma_r = -\frac{Ez}{1-\nu^2} \left( \frac{d^2w}{dr^2} + \frac{\nu}{r} \frac{dw}{dr} \right) \tag{27}$$

After differentiating the deflection and substituting into the above expression, radial stress component can be obtained in partial function form.

for  $0 \leq r \leq b$

$$\begin{aligned}
\sigma_1 &= \frac{3}{4} \frac{z}{t^3} \left\{ (P1-P2) \left[ \frac{b^4(\nu-1)}{a^2} + 4b^2 + 4b^2 \log\left(\frac{a}{b}\right)(1+\nu) \right] \right. \\
&\quad \left. + P2(\nu+3)a^2 - P1(\nu+3)r^2 \right\}
\end{aligned} \tag{28}$$

for  $b \leq r \leq a$

$$\begin{aligned}
\sigma_2 &= \frac{3}{4} \frac{z}{t^3} \left\{ (P1-P2) \left[ \frac{b^4(\nu-1)}{a^2} + \frac{b^4(1-\nu)}{r^2} + 4b^2 \log(a)(1+\nu) \right. \right. \\
&\quad \left. \left. - 4b^2 \log(r)(1+\nu) \right] + P2 \left[ (\nu+3)a^2 - (3+\nu)r^2 \right] \right\}
\end{aligned}$$

Since maximum stress occurs at the center of the plate,  $\sigma_1$  should be used for calculations. To obtain the most accurate results thick plate effects should also be considered. 'y' definition given in Equation (22) and 'y' function given in Equation (23) can be used for calculation of thick non-uniform radial stress as:

$$\sigma_{1\text{thick}} = \sigma_1 \left( \frac{y}{100} + 1 \right) \quad (29)$$

To summarize, the reason for deriving the 'y' function, thin plate stress components, thick plate stress components both for uniform and non-uniform loading is to obtain analytic equations. By using finite element method or by using finite element modeling software these stresses can easily be obtained. However, to able to calculate the stresses in the computer tool, analytic equations are needed because during calculations lots of iterations are going to be performed. Writing a finite element code to run in the background within the sabot design tool would not be meaningful. Because, time needed to design the sabot would be increased immensely, and the development of such a design tool would not be justified.

### **2.3.2. Sabot-1 Pusher Stress Analysis**

Stress analysis of Sabot-1 pusher is investigated according to loading type.

#### **2.3.2.1. Bending Loading**

Up to this point governing relations which are needed for the stress analysis of uniformly and non-uniformly loaded circular plate are derived. Pusher is modeled as a circular plate which is simply supported at the outer boundary. Figure 35 is the 3D view of the location of the model and the sabot on the pusher. Free body

diagram of the pusher with the loads induced and sign convention is given in Figure 36.

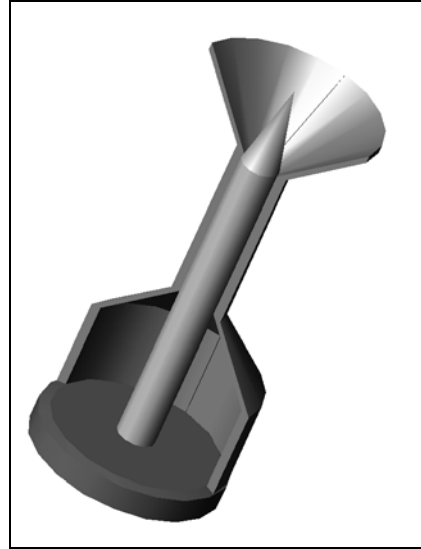


**Figure 35** 3D half view of Sabot-1

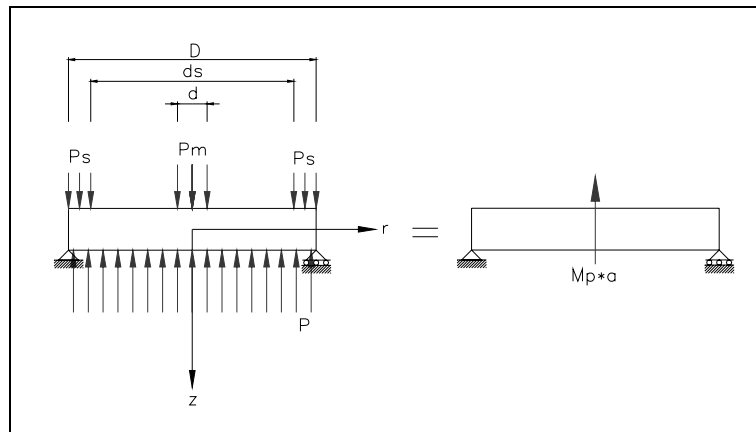


**Figure 36** Free body diagram of Sabot-1 pusher

Set back forces due to acceleration of the system are taken as distributed load which are  $P_s$  (pressure due to sabot) and  $P_m$  (pressure due to model).  $P_s$  exerts on

the annular area enclosed by diameter of the pusher (D) and inner diameter of the back part (section-4) of the sabot wall ( $d_s$ ). Since  $P_m$  is inertial load of the model it acts on the area of model diameter (d). Inertial force of the pusher, which equals to mass of pusher (Mp) times acceleration of the system (a), is also assumed as uniform load distributed over the total area,  $P_{in}$ .

Maximum radial stress on the circular plate occurs at the upper or lower face where  $z=\pm t/2$ , and at the center of the plate where  $r=0$ . Total stress is calculated by the superposition method.  $S_p$  is the stress caused by gun pressure which is calculated by thin plate theory.  $S_{Pin}$ ,  $S_{Pm}$  and  $S_{Ps}$  are stresses caused by pusher, model and sabot inertial loads, respectively. These stresses are also calculated by using thin plate formulas.

$$\begin{aligned}
 S_p &= \sigma_r \Big|_{\substack{r=0 \\ z=\pm t/2 \\ q=-P}} & S_{Pin} &= \sigma_r \Big|_{\substack{r=0 \\ z=\pm t/2 \\ q=-P_{in}}} \\
 S_{Pm} &= \sigma_1 \Big|_{\substack{r=0 \\ z=\pm t/2 \\ P1=Pm \\ P2=0 \\ a=D/2 \\ b=d/2}} & S_{Ps} &= \sigma_1 \Big|_{\substack{r=0 \\ z=\pm t/2 \\ P1=0 \\ P2=Ps \\ a=D/2 \\ b=ds/2}}
 \end{aligned} \tag{30}$$

In Equation (30)  $\sigma_r$  is the thin plate radial stress component given in Equation (21) and  $\sigma_1$  is the thin plate non-uniform loading radial stress component given in Equation (28). P1, P2, 'a' and 'b' are shown in Figure 34.

According to the given stresses in Equation (30), total corrected radial stress, to account for the R can be calculated as;

$$R = (S_p + S_{Ps} + S_{Pm} - S_{Pin}) \left( \frac{y}{100} + 1 \right) \tag{31}$$

Fracture failure is the condition where the material is incapable of withstanding the stress. To predict the failure, von Misses criterion will be used (Equation (32)).  $\sigma_y$  is yield stress [3].

$$2\sigma_y^2 = (\sigma_r - \sigma_\theta)^2 + (\sigma_\theta - \sigma_z)^2 + (\sigma_z - \sigma_r)^2 + 6(\sigma_{r\theta}^2 + \sigma_{\theta z}^2 + \sigma_{rz}^2) \quad (32)$$

According to the failure criterion maximum von Misses stress occurs at lower surface where  $r=0$  and  $z=t/2$ . At this point  $\sigma_{rz}$  is zero.  $\sigma_r$  equals to  $\sigma_\theta$ , and both are equal to  $R$ .  $\sigma_z$  is  $-P$ , where 'P' is maximum chamber pressure. Thus, failure criteria for bending should be;

$$\sigma_y > R + P \quad (33)$$

#### 2.3.2.2. Shear Loading

Model and sabot inertial forces cause shear stress in the pusher. Pressure behind the pusher tries to accelerate the system. On the contrary, model and sabot creates force in the opposite direction. Sabot set back force acts on the outer region of the pusher. Thus, side surface area that the shear force is acting on is large. On the other hand, model diameter is very small and it is located around the center of the pusher. Therefore, model shear force is dominant. Since thickness will be determined based on the maximum stress, calculating shear stress only for model will be enough.

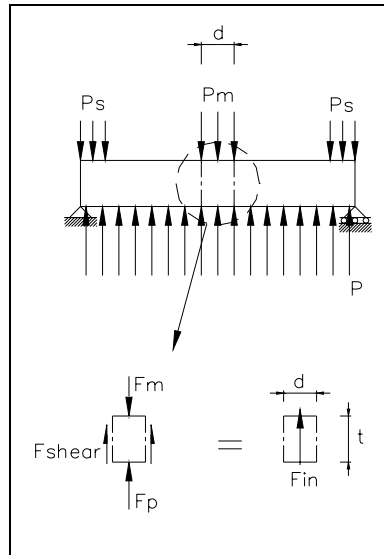


**Figure 37** Free body diagram of shear loading

Forces on pusher part for shear stress calculation are given in Figure 37. Equilibrium of these forces can be written as;

$$F_p + F_{\text{shear}} - F_m = F_{\text{in}} \quad (34)$$

$$F_p + F_{\text{shear}} - F_m - F_{\text{in}} = 0$$

where;

$$F_p = P\pi \frac{d^2}{4}, \quad F_{\text{shear}} = \pi dt\tau \quad (35)$$

$$F_m = M_m a, \quad F_{\text{in}} = \pi \frac{d^2}{4} t\rho a$$

In Equation (35); 'P' is the chamber pressure, 't' is the thickness of the pusher,  $\tau$  is shear stress,  $M_m$  is mass of the model,  $\rho$  is density of the pusher material and 'a' is the acceleration of the whole system.

For failure criterion octahedral shear stress theory is used. Thickness of the pusher can be calculated by using Equation (34) and the following criteria [7].

$$\frac{\sqrt{2}}{3} \sigma_y > \tau \quad (36)$$

### 2.3.3. Sabot-2 Pusher Stress Analysis

Stress analysis of Sabot-2 pusher is investigated according to loading type.

#### 2.3.3.1. Bending Loading

Stress analysis of Sabot-2 pusher is similar to Sabot-1 pusher. Again maximum stress occurs at lower face where  $z=t/2$ , and at the center of the plate where  $r=0$ . The only difference is location of the sabot on the pusher. Free body diagram is given in Figure 39, and 3D cut-out view is given in Figure 38.

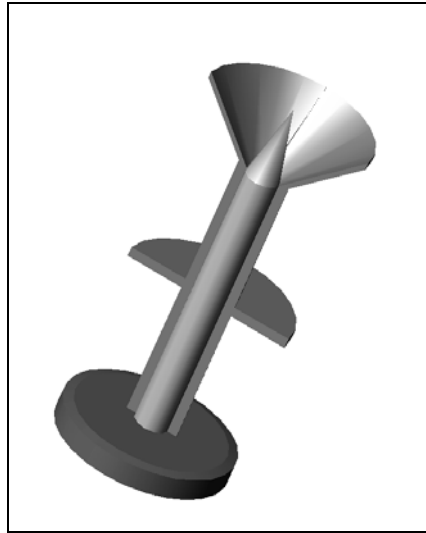


**Figure 38** 3D half view of Sabot-2

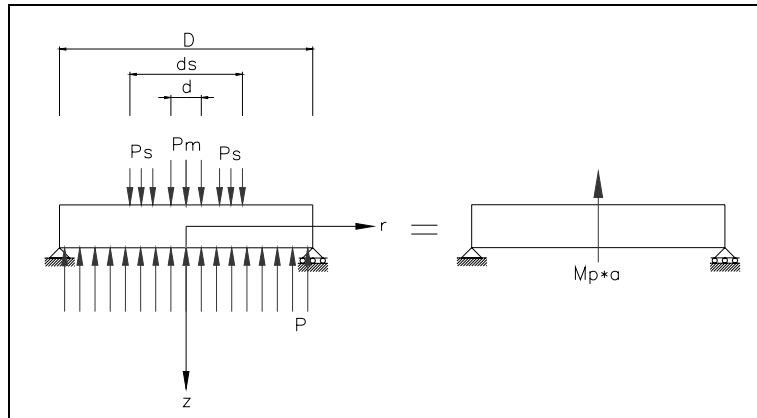


**Figure 39** Free body diagram of Sabot-2 pusher

Since pressure due to sabot is acting on the region enclosed by diameter  $d_s$  and  $d$ , non-uniform loading formulation will have to be changed. Bending stress calculation due to sabot can be obtained by superposition method (Figure 40).

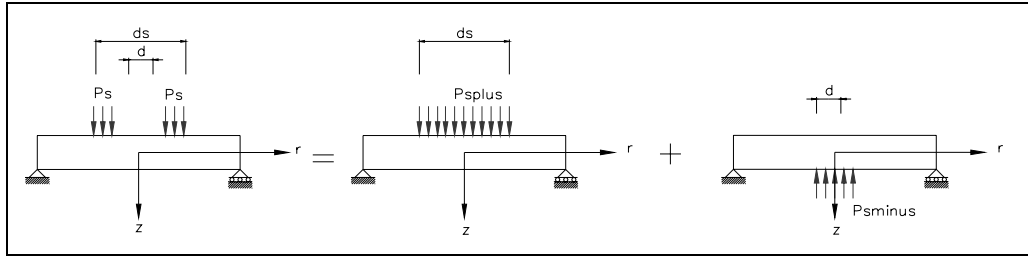


**Figure 40** Superposition of sabot pressure

Radial stress can be calculated by using Equation (21) and (28) like the pusher of Sabot-1.

$$\begin{aligned}
 S_p &= \sigma_r \Big|_{r=0}^{z=t/2} \\
 &\quad q=-P \\
 S_{pin} &= \sigma_r \Big|_{r=0}^{z=t/2} \\
 &\quad q=-Pin \\
 S_{Pm} &= \sigma_1 \Big|_{r=0}^{z=t/2} \\
 &\quad P1=Pm \\
 &\quad P2=0 \\
 &\quad a=D/2 \\
 &\quad b=d/2 \\
 S_{Psplus} &= \sigma_1 \Big|_{r=0}^{z=t/2} \\
 &\quad P1=Psplus \\
 &\quad P2=0 \\
 &\quad a=D/2 \\
 &\quad b=ds/2 \\
 S_{Psminus} &= \sigma_1 \Big|_{r=0}^{z=t/2} \\
 &\quad P1=-Psminus \\
 &\quad P2=0 \\
 &\quad a=D/2 \\
 &\quad b=d/2
 \end{aligned} \tag{37}$$

Total corrected radial stress can then be calculated by;

$$R = \left( S_p + S_{Psplus} + S_{Psminus} + S_{Pm} - S_{pin} \right) \left( \frac{y}{100} + 1 \right) \tag{38}$$

The same failure criteria given in Equation (32) will be used. Maximum stress at the critical point will be  $R+P$ , where 'P' is maximum chamber pressure. Therefore, to obey the von Misses failure criterion this value should be smaller than yield stress of the material (Equation (39)).

$$\sigma_y > R+P \quad (39)$$

#### 2.3.3.2. Shear Loading

Shear stress calculation is same as the Sabot-1 pusher shear stress calculation.

#### 2.3.4. Sabot-1 Stress Analysis

As mentioned in the previous section, Sabot-1 has 4 sections (Figure 41). Each section has different analysis procedure.

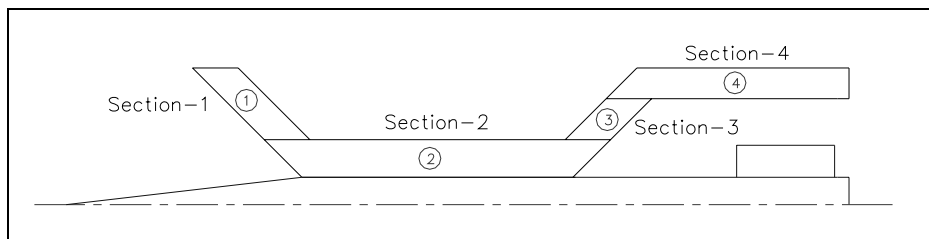


**Figure 41** Sections of Sabot-1

#### 2.3.4.1. Section-1; Bending and Shear Loading

Stress analyses of section-1 and section-3 have some assumptions. Since sabot is a revolved solid, application of bending stress calculation of a beam is not suitable. However, the aim is to calculate the stresses by using simple strength of materials relations. There is no need to derive a formula for inclined and revolved solid. The solution procedure for this problem is taken care by first assuming that section-1 is not curved but rather it is a rectangular prism. This assumption is shown in Figure 42. Then, solving some real cases by the finite element method a database can be created. This database can be used to relate the actual case to the approximate case through a correction factor which will be denoted by ' $c_{nA}$ ' in this study.

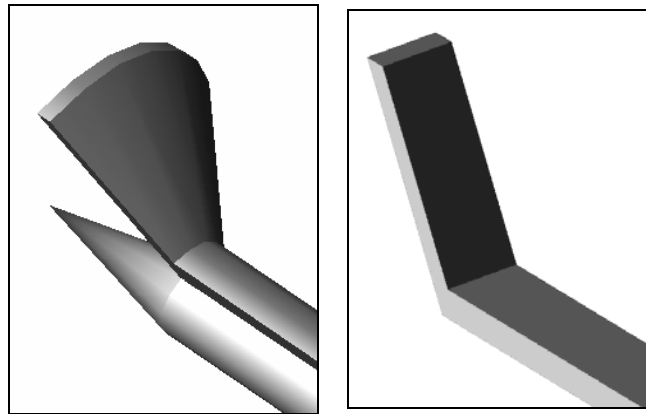


**Figure 42** Section-1 assumption

From the strength of materials approach, bending of a clamped beam case is suitable for this situation (Figure 43). After some modifications Equation (40) can be used.

Stress is defined as;

$$\sigma_b = \frac{M(x)y}{I} \quad (40)$$

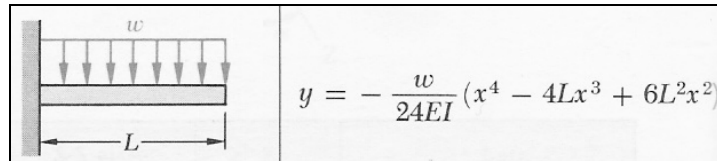


**Figure 43** Bending due to distributed load [13]

In Figure 43, deflection equation ‘y’ for a clamped beam under distributed load per unit length, ‘w’, is given [13]. To find the moment expression, derivative of the deflection equation is taken twice. After some manipulations moment expression can be obtained as;

$$M(x) = -\frac{1}{2}w(x^2 - 2Lx + L^2) \quad (41)$$

The aim here is to find the stress at point ‘X’ shown in Figure 44. For this purpose Equation (41) and (40) will be used with the parameters given in Figure 44.

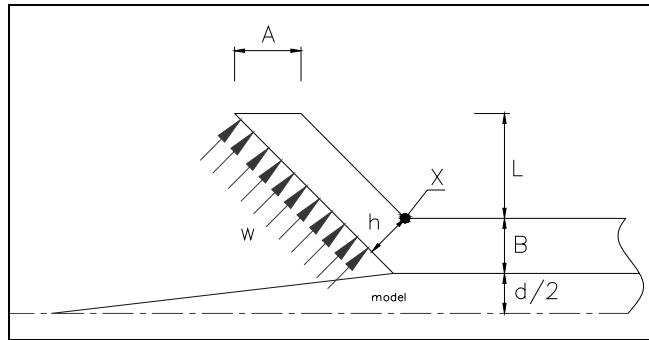


**Figure 44** Sabot-1 section-1

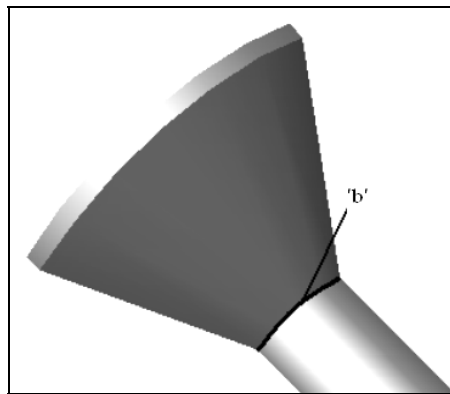


**Figure 45** Arc length 'b'

Moment of inertia of the section-1 is given in the following equation. 'b' is arc length which is  $\frac{1}{4}$  portion of the sabot at the radius where 'X' is located (Figure 45). It should be noted that, by taking 'b' as the width of the rectangular beam, more conservative results will be obtained for the stresses.

$$I = \frac{1}{12}bh^3 ; \quad h = A\sin(45^\circ) \quad (42)$$

$$b = \frac{2\pi(d/2+B)}{4}$$

Maximum bending stress occurs at the upper surface where

$$y = \frac{A \sin(45^\circ)}{2} \quad (43)$$

Moment will be calculated at the root section 'X'. In the moment expression 'w' is given in the form of force per unit length. Total force acting on the section-1 is inertial force due to mass of the section. This force is called as  $F_{inA}$ . But inertial force is acting in the acceleration direction which is parallel to the axis. Vertical force is needed to calculate the bending stress. Thus, vertical component of the force ' $F_{inA} \sin(45^\circ)$ ' should be used. If vertical component of the force is divided by the length of the section, which is ' $L/\sin(45^\circ)$ ', distributed load will be obtained.

$$w = \frac{F_{inA} \sin(45^\circ)}{L/\sin(45^\circ)} \quad (44)$$

When Equations (41), (42), (43) and (44) are inserted into the Equation (40) bending stress,  $S_{bA}$ , at point 'X' can be obtained.

Horizontal component of the inertial load causes compression stress at point 'X'. This compression stress,  $S_{cA}$ , is obtained from Equation (45).

$$S_{cA} = \frac{F_{inA} \cos(45^\circ)}{(hb)} \quad (45)$$

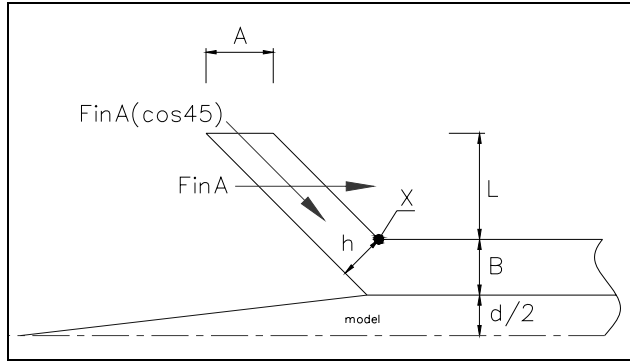


**Figure 46** Section-1 compression force

Finally exact stress at the intersecting region of section-1 and section-2 can be expressed by;

$$S_{tA} = (S_{bA} + S_{cA})c_{nA} \quad (46)$$

Calculation of correction factor  $c_{nA}$ , which relates the approximate strength of materials approach to finite element solution, will be explained in Chapter 3 in detail.

Another stress component on the region that can cause failure is shear stress acting on the region when section-1 is cut horizontally at point 'X'. This shear stress is given as;

$$S_{sA} = \frac{F_{inA}}{(bA)} \quad (47)$$

#### 2.3.4.2. Section-2; Compression Stress and Buckling Analysis

At section-2, dominant stress is compression. Since section-2 seems to be a long rod, compressive force may cause buckling. Total compressive force is multiplication of the mass in front of the most rear part of the section-2 and acceleration of the system. In addition to the inertial force of this section, there exists an eccentric force caused by the inertial force of the section-1. Assuming that inertial force of section-2 is not distributed but; it acts as an external concentrated force. Thus, with this assumption problem turns into eccentrically and normally loaded buckling problem (Figure 47).

The geometry of this region is quarter part of a hollow cylinder. It can be called as curved panel. In literature there are expressions about the buckling of a curved panel. But these expressions are valid for thin panels. Sabot structure is not suitable to use these expressions. Therefore, section-2 is approximated as a straight rectangular beam under axial and eccentric loading.

Section-3 fixes the transverse movement of the section-2, thus this region can be said to be clamped. Front region can move axially but not in the transverse direction (Figure 47).

To justify the approximation with regard to buckling of section-2, finite element analysis is applied on two different geometries. The aim is to see whether column or curved panel buckles easily. With this analysis, deformed shape of a curved column can also be determined. Both parts have the same length and cross sectional area and loading are also identical.

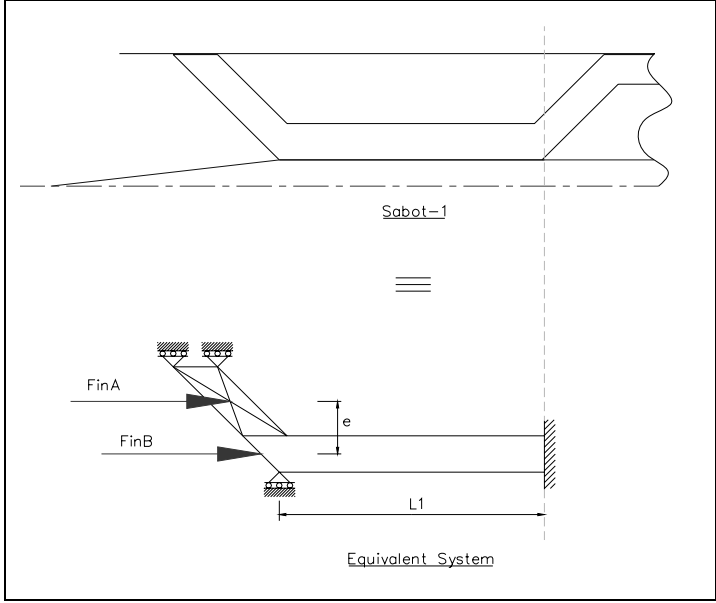


**Figure 47** Equivalent system for buckling analysis

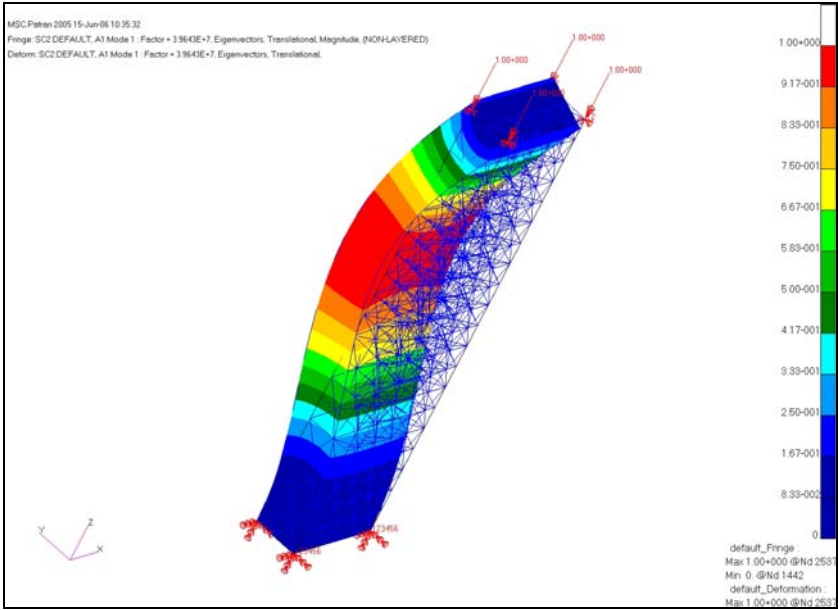


**Figure 48** Column buckling

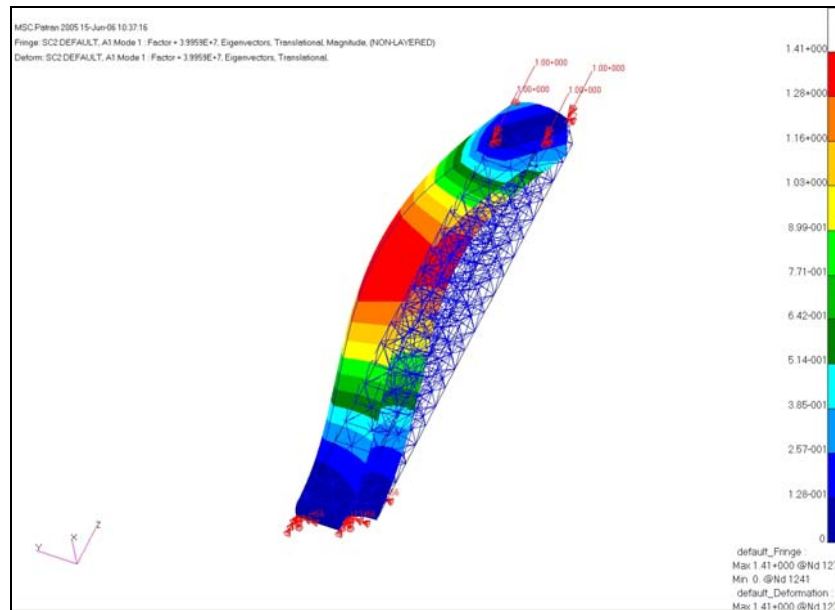


**Figure 49** Curved column buckling

Finite element analyses are performed using MSC NASTRAN<sup>®</sup>/PATRAN<sup>®</sup> buckling analysis module. Figure 48 and Figure 49 are taken from the MSC PATRAN<sup>®</sup> output file. From the images, it is seen that for the straight column buckling stress is  $3.96e7$  Pa and for the curved column buckling stress is  $3.99e7$  Pa. Therefore, straight column buckles under lower loading than curved column. Although this conclusion is achieved by finite element analysis, it is known that curved thin panels have higher buckling loads compared to straight thin panels [16]. Therefore, straight column assumption is more conservative, and can be used for approximate analytical results. Curved column deforms in the outer direction which is away from the projectile.

After these assumptions and explanations, buckling analysis starts from the equilibrium of moments on the column (Equation (48)). In the following equation ‘w’ is the transverse displacement of the column and M is the moment on the column due to eccentricity [15]. Forces and eccentricity ‘e’ are shown in Figure 47.

$$(F_{inA} + F_{inB})w + F_{inA}e - M = 0 \quad (48)$$

The governing equation for transverse displacement can be written as;

$$\frac{d^2w}{dx^2} + \frac{(F_{inA} + F_{inB})}{EI}w = -\frac{F_{inA}e}{EI} \quad (49)$$

The solution of this non-homogeneous differential equation is;

$$w(x) = C_1 \sin(\sqrt{m}x) + C_2 \cos(\sqrt{m}x) - \frac{n}{m} \quad (50)$$

$$m = \frac{F_{inA} + F_{inB}}{EI}, \quad n = \frac{F_{inA}e}{EI}$$

The coefficients  $C_1$  and  $C_2$  depend on the boundary conditions. Deflection 'w' should satisfy the following boundary conditions.

$$BC; w(0) = w(L) = 0$$

$$C_1 = \frac{n}{m} \tan\left(\sqrt{m} \frac{L}{2}\right) \quad (51)$$

$$C_2 = \frac{n}{m}$$

Maximum stress,  $S_{\text{buckle}}$ , can be obtained from secant formula.

$$S_{\text{buckle}} = \frac{(F_{\text{inA}} + F_{\text{inB}})}{\text{Area}} + \frac{F_{\text{inA}} (w_{\text{max}} + e) B/2}{I} \quad (52)$$

where area is cross sectional area of the column and 'B' is the thickness of the column. Maximum deflection  $w_{\text{max}}$  is obtained from the following equation.

$$w_{\text{max}} = w \left( \frac{L l_{\text{actual}}}{2} \right) = \frac{n}{m} \left[ \sec \left( \sqrt{m} \frac{L l_{\text{actual}}}{2} \right) - 1 \right] \quad (53)$$

In Figure 50, actual lengths of columns for different boundary conditions are seen [14]. Configuration (d) is suitable for our problem. Therefore, effective length constant of the column is taken as 0.7.

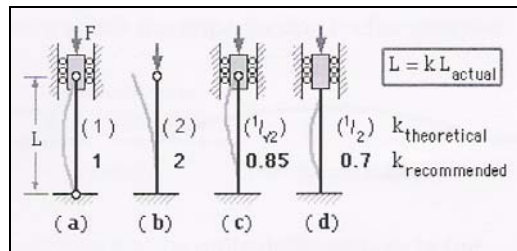


**Figure 50** Actual length of a column

Finally secant formula can be used to compute the allowable compression stress;

$$S_{\text{buckle}} < \sigma_y \quad (54)$$

First term of the secant formula is simple compression stress term and second term comes from the eccentricity. Therefore, buckling stress is always greater than the compression.

#### 2.3.4.3. Section-3; Bending and Shear Loading

Stress calculation procedure for section-3 is same as the section-1. Again this section is assumed as rectangular prism and bending stress formula is applied. Then with some real case solutions with finite element analysis a correction factor is obtained. By using this correction factor and the bending formula that will be given, actual stress at point 'X' shown in Figure 51 can be obtained.

Since formulas are derived for rectangular prism, it is expected that stress at X and Y will be equal. Thus, according to following formulas and Figure 51, it will be realized that derivation of formulas are actually done for point Y. On the other hand, in real case this geometry is a solid of revolution and some parameters at point X and Y are different, for example cross section area. This is the reason for using the parameters of point X in the following formulas instead of point Y parameters.

In this section, the main force is inertial force due to the total mass of section-1 and section-2 which are located in front of the point 'X'. It is assumed that sabot is clamped at section-4 and force is horizontally applied from section-2.

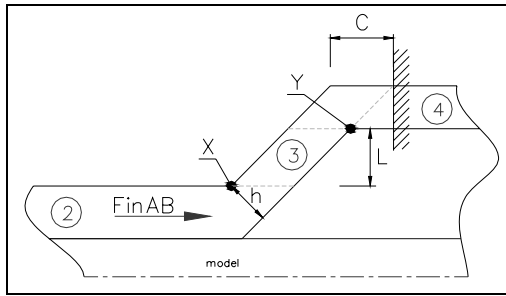


**Figure 51** Sabot-1 section-3

Thickness of the section-3 when cut horizontally is 'C' and  $h = C \sin(45^\circ)$ . Angle for section-1 was decided to be  $45^\circ$ . For simplicity of calculations angle of the section-3 will be  $45^\circ$  (Figure 52).

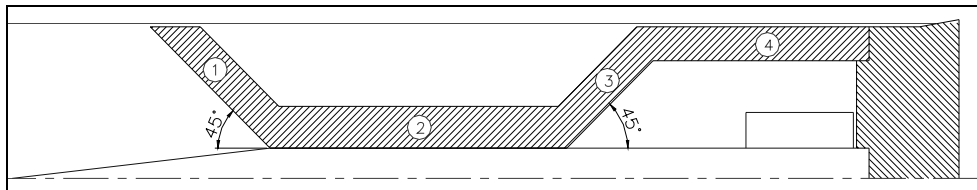


**Figure 52** Section angles

Bending stress formula due to a force is;

$$\sigma_b = \frac{Fxy}{I} \quad (55)$$

In Equation (55), 'x' denotes the moment arm distance and 'F' denotes the force acting perpendicular to the beam.

$$F = F_{inA} + F_{inB} = F_{inAB}$$

$$x = \frac{L}{\sin(45)} \quad (56)$$

$$y = \frac{C \sin(45)}{2}$$

$$I = \frac{1}{12} \frac{2\pi \left(\frac{d}{2} + B\right)}{4} (C \sin(45))^3$$

Here,  $F_{inA}$  and  $F_{inB}$  are inertial forces due to section-1 and section-2, respectively. Bending stress at 'X',  $S_{bc}$ , can be calculated by substituting Equation (56) into Equation (55). Parameters in these equations are given in Figure 51. Horizontal component of  $F_{inAB}$  causes compression stress. This stress can be calculated as;

$$S_{cc} = \frac{F_{inAB} \cos(45)}{(hb)} \quad (57)$$

$$b = \frac{2\pi(d/2+B)}{4}$$

Calculation of correction factor,  $c_{nC}$ , for this region will be explained in Chapter 3. More realistic stress at the intersecting region of section-2 and section-3 is given by Equation (58).

$$S_{tC} = (S_{bc} + S_{cc})c_{nC} \quad (58)$$

In addition to compression stress, shear stress is another failure mechanism like in section-1. This shear stress can be obtained as;

$$S_{sC} = \frac{F_{inAB}}{(bC)} \quad (59)$$

#### 2.3.4.4. Section-4; Compression Stress

Section-4 is the rear part of the sabot. Thus, inertial force is highest at this section. Contact surface between sabot and pusher is under compression. Since outer radius of section-4 is equal the gun tube radius, buckling is not possible. Displacement in the outward direction is also restricted.

Compression stress,  $S_{cD}$ , can be calculated by using the Equation (60). In Equation (60),  $M_s$  is total weight of the sabot. Since sabot is composed of 4 parts, mass of each part is  $M_s/4$ . Acceleration of the system is 'a'.

$$S_{cD} = \frac{F_s}{\frac{\pi}{4}(D^2 - d_s^2)} \quad (60)$$

$$F_s = \frac{M_s}{4} a$$

Diameters in Equation (60) are given in Figure 53.

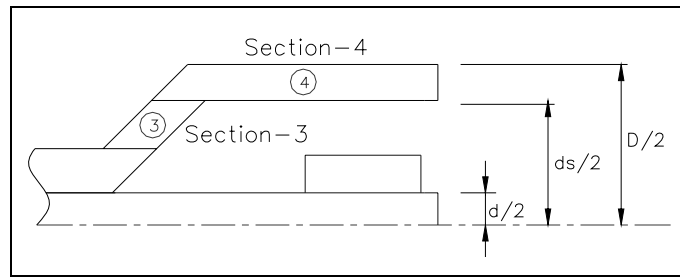


**Figure 53** Diameters of Sabot-1 for calculations

### 2.3.5. Sabot-2 Stress Analysis

The only difference between Sabot-1 and Sabot-2 is the rear part geometry. Section-1 and section-2 are same in geometry, and same forces act on them, as in Sabot-1. Therefore, bending & shear calculation at section-1 and compression & bending calculation at section-2 can also be used for Sabot-2. Since section-3 and section-4 has different geometries with different loadings, formulations for these sections will be different, and they will be explained in the following paragraphs. Sections of Sabot-2 are given in Figure 54.

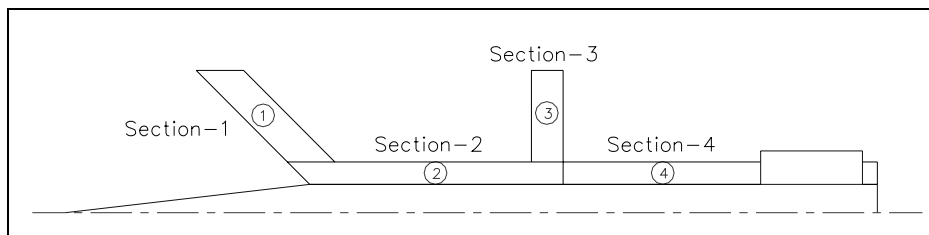


**Figure 54** Sections of Sabot-2

### 2.3.5.1. Section-3; Bending and Shear Loading

The force acting on this section is only inertial force due to its mass. Thus, stress formulation contains distributed load 'w'. Parameters that will be used in the formulation are given in Figure 55.

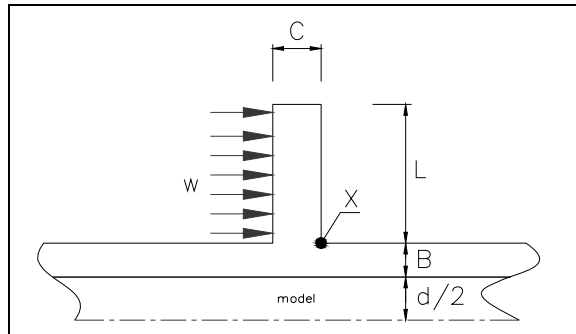


**Figure 55** Sabot-2 section-3

Procedure is similar to the calculation in Sabot-1 section-1. In this case, load and the orientation of the section-3 are perpendicular to each other. Moment due to distributed load can be calculated from Equation (41) where;

$$w = \frac{F_{inC}}{L}$$

$$x = 0 \tag{61}$$

$$L = \frac{D}{2} - \frac{d}{2} - B$$

Moment of inertia at the cross section 'X' is;

$$I = \frac{1}{12} \frac{2\pi \left(\frac{d}{2} + B\right)}{4} C^3 \quad (62)$$

Substituting Equation (61) and (62) into the Equation (40) bending stress,  $S_{bc}$ , can be obtained. Here maximum stress occurs on the surface therefore 'y' has to be taken as  $\frac{C}{2}$ .

At the vertical cross section area at point 'X', compression force due to inertia is another stress producer. Compression stress at this cross section,  $S_{cC}$ , can be easily calculated.

$$S_{cC} = \frac{F_{inA} + F_{inB}}{\pi \left(\frac{d}{2} + B\right)^2 - \pi \left(\frac{d}{2}\right)^2} \quad (63)$$

By using the correction factor, which will be explained in Chapter 3, total compressive stress is given as Equation (64). Correction factor  $c_{nC}$  is different than the correction factor of Sabot-1 section-3.

$$S_{tC} = (S_{bc} + S_{cC})c_{nC} \quad (64)$$

### 2.3.5.2. Section-4; Compression Stress

Section-4 of Sabot-2 is exposed to whole inertial force. This part lies on the model; it does not have any contact surface with the gun barrel. In the compression stress formula, given by Equation (60),  $F_s$  is the total inertial force. In Figure 56 dimensions that are used are given.

$$S_{cD} = \frac{F_s}{\frac{\pi}{4}(d_s^2 - d^2)} \quad (65)$$

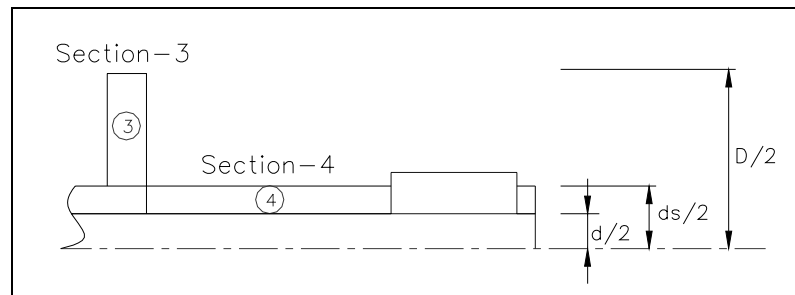


**Figure 56** Diameters of Sabot-1 for calculations

## **CHAPTER 3**

### **SABOT DESIGN TOOL**

In Chapter 2, formulations used for calculating the stresses for a certain region were explained. Stresses at the critical regions can be calculated with these expressions, but the important thing is to find the appropriate geometry to satisfy the failure criteria. In addition, the aim is also to obtain the minimum weight for the sabot. This can be achieved by minimizing the thicknesses. As the thickness of the sections getting thinner, stresses at the critical regions become higher. Therefore, thicknesses should be changed gradually to control the stresses. Since all of the parameters are related with each other, any change in the thickness also results in a change in the weight. So, it is obvious that, changing one of the parameters also affects the mass and thus acceleration of the whole system.

To make such calculations automatically, a computer tool has been developed by MathWorks Inc.'s Matlab<sup>®</sup> 7.1. Stress calculations, iterations and necessary modifications are embedded in the tool. Finally geometry of the sabot walls and pusher, with appropriate thicknesses and modifications, are given as an output of the computer tool. The tool is named as Sabot Design Tool, SDT.

Two different sabot configurations have been mentioned in the previous chapters. The tool is developed separately for each of the sabots. Each tool has approximately 450 strings. Tool calculation time for a case depends on the chosen Mach number, because iterations increase with increasing Mach number. Maximum calculation time is not more than fifteen minutes. In this chapter, design procedure used in the design tools will be explained.

### 3.1 MODIFICATIONS ON SABOT GEOMETRIES

Up to now theory and derivation of the stress formulas are given. From stress analyses and past experiences it is concluded that a sabot may need some modifications on its geometry or change in material selection.

First of all, to see the critical regions mentioned in the previous sections, analyses have been performed for two different sabot types (Figure 57 & Figure 58). MSC NASTRAN®/PATRAN® FEM software has been used for this purpose. Sabot is fixed at its back face and contact surfaces with model and gun bore are set free in axial direction. Load is given as a realistic inertial load.

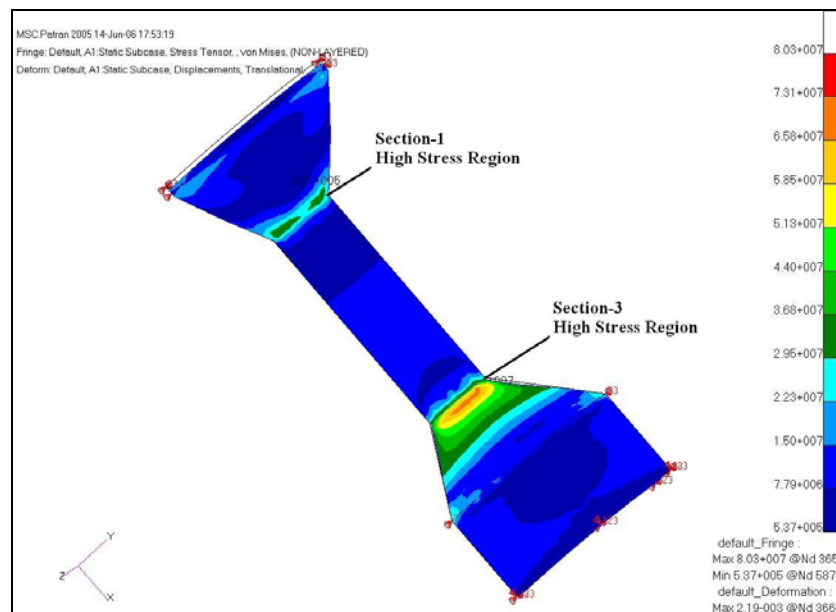
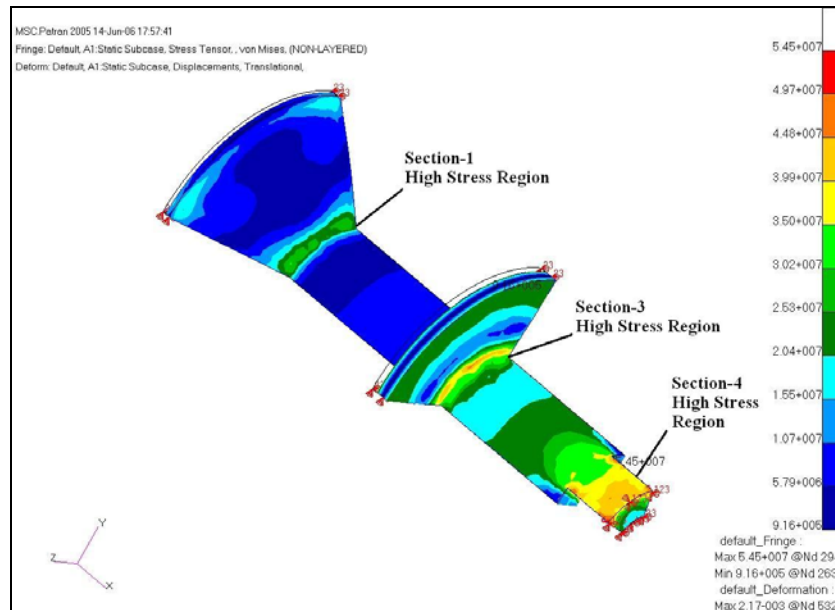
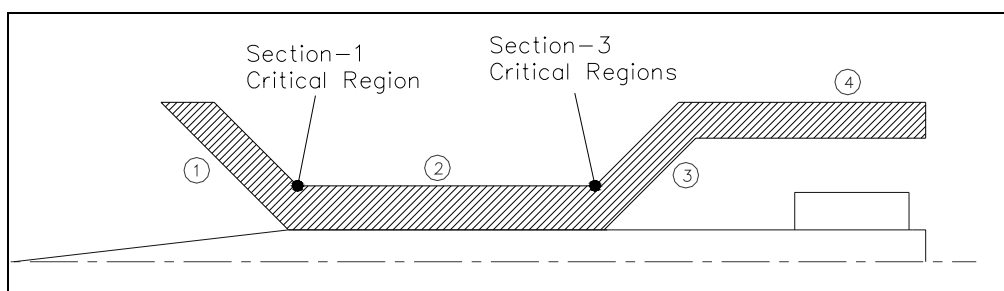


Figure 57 Sabot-1 FEM analysis



**Figure 58** Sabot-2 FEM analysis

Scales in the Figure 57 and Figure 58 show the von Misses stress in Pa unit on the sabot. As seen in these figures, most critical region is section-3 and section-1 has higher stresses than other regions. At Chapter 2, most critical regions have been predicted as shown in Figure 59 and Figure 60. Based on these analyses; we can say that predicted high stress regions are correct.



**Figure 59** Predicted critical regions for Sabot-1

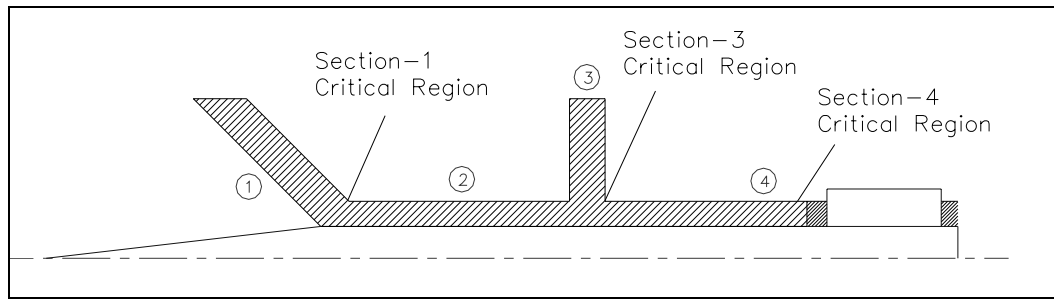


**Figure 60** Predicted critical regions for Sabot-2

From the calculations performed by using the derived formulas, it is concluded that pusher needs a support plate. Results of these calculations are given as a graph in Figure 61. This graph shows the polycarbonate pusher thickness with respect to Mach number for different support plate diameters. Model diameter has been taken as 20 mm. Pusher without a support plate has a thickness almost as twice as the thickness of pusher with a support plate which has a 40 mm diameter.

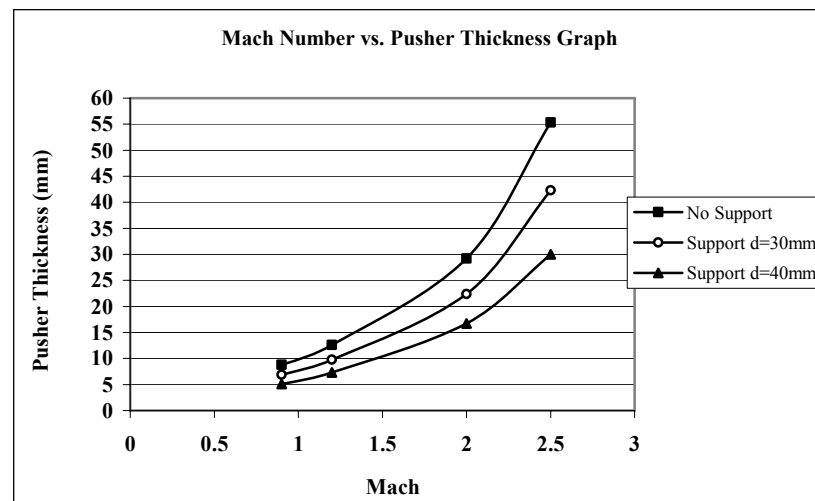


**Figure 61** Mach vs. Pusher Thickness Graph

Projectile is made from metal material which is hard and tough. But for Sabot-1 pusher, since weight is very important, it is decided to use polycarbonate. At the contact surface between sabot and projectile, compression and shear stresses are always higher than the material yield stress when only polycarbonate is used. To decrease the high stresses, it will be better to use a metal support. By making this support a little larger in diameter than projectile diameter, inertial force of the model can be distributed to a larger area (Figure 62). Therefore, radial stress can be reduced. Diameter of the support metal plate is 'd2' and its thickness is 't2'. In addition to bending stress analysis, shear stress analysis is also changed with this support plate.

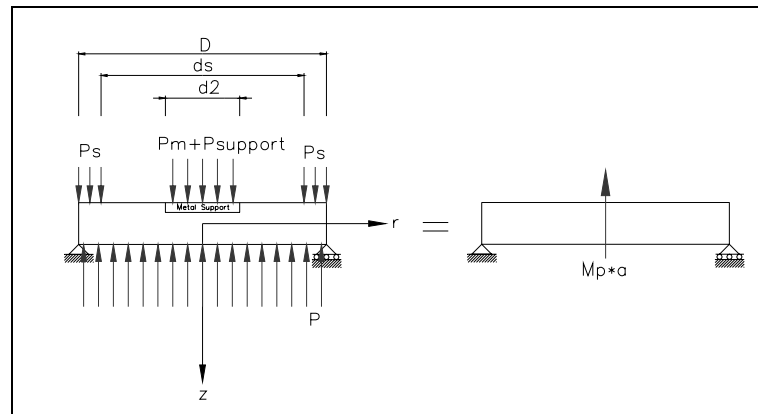


**Figure 62** Sabot-1 pusher support

The purpose in designing Sabot-2 is to use it at high velocities. During thickness calculations of a polycarbonate pusher at high velocities, it has been seen that pusher thickness was increasing drastically with increasing weight. When support plate is used for these conditions, its diameter should be almost same as the pusher diameter. This low density material turns out to be a disadvantage when it is used at high velocities. Therefore, high strength material is needed for a pusher material. Thus, for Sabot-2, pusher material is decided to be a metal material.

In addition, some modifications need to be done on the sabots. Sometimes only increasing the section thickness does not work. Since main force is the inertial force, increasing the thickness consequently increases stresses. Therefore, to reduce the stresses at the critical regions of sabots, some geometric modifications may be needed, and these modifications (AB,BC,CD and D) are given in the following figures (Figure 63 & Figure 64).

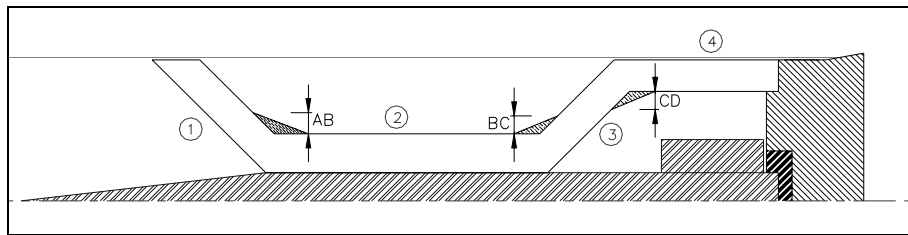


**Figure 63** Sabot-1 modification

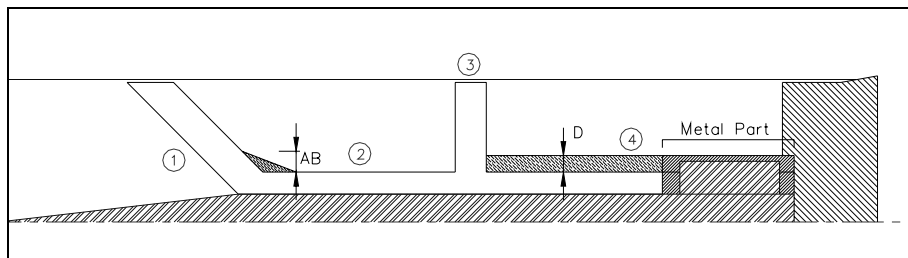
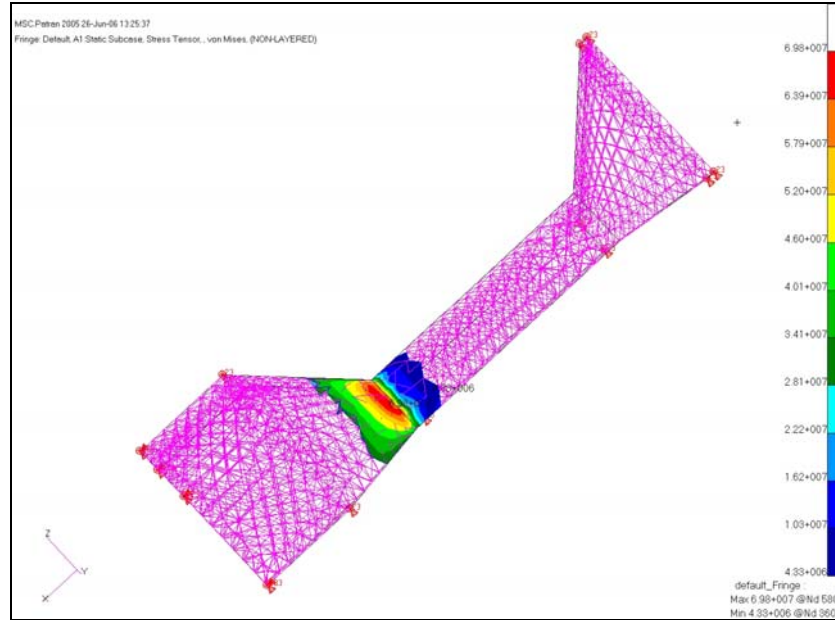


**Figure 64** Sabot-2 modification

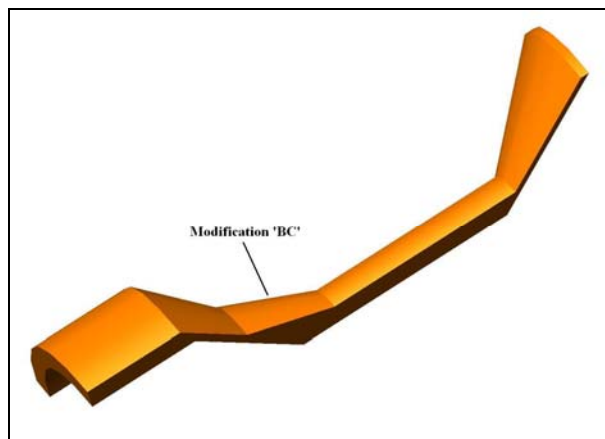
Finite element analyses have been performed on sabots with these modifications. It is seen that modification 'BC' and 'CD' has a worse effect on the sabot. They increase the stresses at the intersecting regions since weight is increased.

Figure 65 is the stress plot of a Sabot-1. Von Misses stress at section-3 without any modification is shown. Maximum stress is 69.8 MPa. Figure 67 is the finite element analysis result of the same sabot with modification at section-3 which is

given in Figure 66. Here, it can be seen that von Mises stress increases to 70.4 MPa after modification.



**Figure 65** Section-3 von Mises stress



**Figure 66** 3D Model of sabot with BC modification

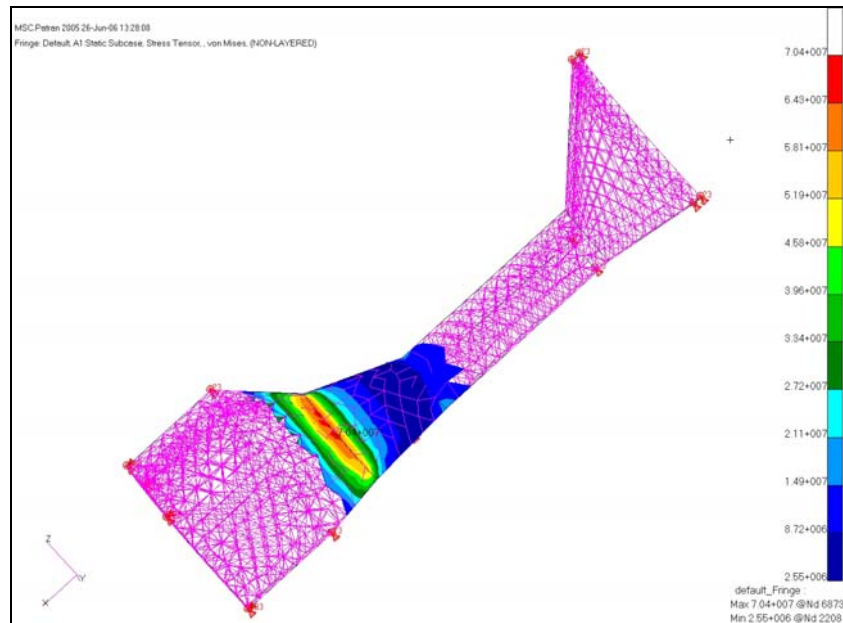


**Figure 67** Modified section-3 von Mises stress

Figure 68 is the von Mises stress plot of inner intersecting region of section-3 and section-4 of Sabot-1. Without modification, maximum stress at this region is 40.4 MPa. Figure 69 is the 3D model of the same sabot with modification CD and Figure 70 is finite element analysis result of this sabot. With modification, stress at the same region is 51 MPa.

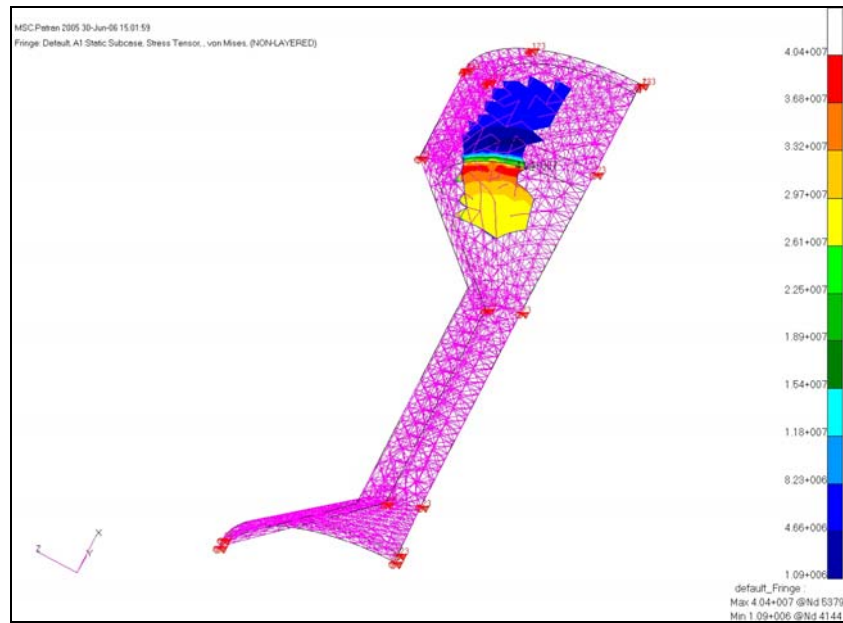


**Figure 68** Upper section-3 von Mises stress

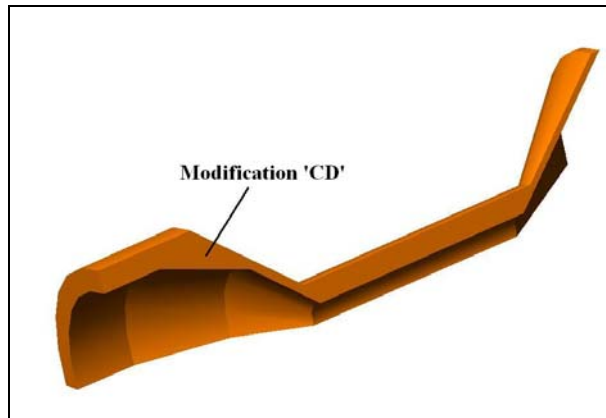


**Figure 69** 3D Model of sabot with CD modification

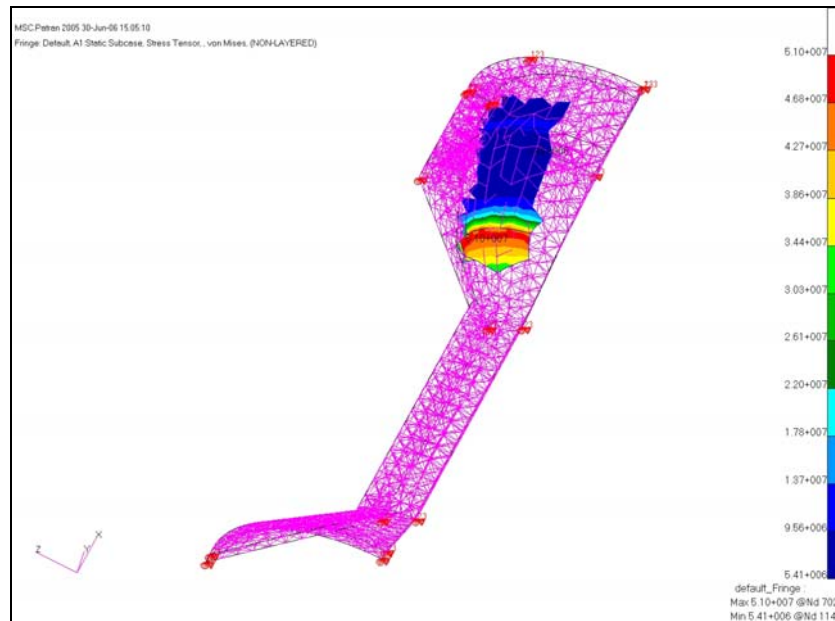


**Figure 70** Modified upper section-3 von Mises stress

But modification 'AB' for both sabots decreases the stress, because 'AB' length shortens the moment arm 'L'. This modification is the only way to reduce the stress at that region. From the analysis it was seen that increasing the thickness 'A' (Figure 71), increases the stress. Minimum stress is achieved by minimum 'A'. Therefore, it was decided that if stress at section-1 for a minimum value of 'A' is greater than yield stress, then AB modification will be implemented.

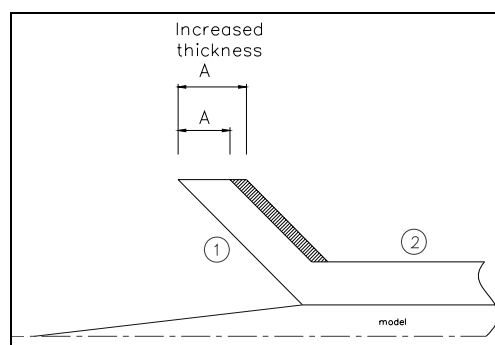


**Figure 71** Increased thickness A

In Sabot-2, a modification like AB can also be applied to intersection of section-3 and section-4 to shorten the moment arm. But there is another alternative for this idea. Sabot-2 will be used for high velocities and at these velocities finite element analysis were also performed. From these analyses it is seen that compressive stress at section-4 is very high. Therefore, increasing the thickness of section-4 'D' amount will result in an increase in the cross sectional area which in turn reduces the stress and moment arm at section-3. In addition to that, at the very rear region compression is too high. Using metal material in this region is the only way to get over this problem (Figure 64).

Modification 'D' is helpful for decreasing the stress value at the section-3. Thickness of section-3 has been named as 'C'. Neither increasing the thickness of section-3, nor using minimum thickness is the correct way to minimize the stress at the intersection region. Minimum stress is achieved for a certain 'C' value for specific 'B' value. Determination of thickness 'C' will be explained in Chapter 3.5.

## **3.2 MATERIAL SELECTION**

Material selection for a sabot is also an important subject. Since the aim is to achieve the lightest sabot, the most important criterion is the density of the material. The material should resist to high temperatures during the gun bore travel. Also during the production processes, material dimensions should not change due to the increasing temperature. In addition, high yield stress is desired because of high loadings. Besides these, it is also required that material should be deformable enough to fit in the bore without causing any damage to the gun.

These are the desired mechanical properties of the material. But the procurement and the cost of the materials are the restrictive subjects. When the conditions are examined, two different plastic material options are available. These are polyamid and polycarbonate. When plastics are compared with metals, plastics are preferred for sabot productions, because of their low density and deformation ability.

Based on the experiences, manufacturing temperature is very important. Polyamide material can easily expand when temperature increases. This causes real problems while placing the sabot in the gun. Manufacturing tolerances are very important in sabot production. On the other hand, yield strength of the polyamide is lower than polycarbonate.

Polycarbonate features great mechanical strength within a broad temperature range. It has good dimensional stability. As a result it is decided to use polycarbonate for sabot material.

Properties of the polycarbonate and the polyamide are given in Table 2.

**Table 2** Plastic Material Properties

	Polycarbonate	Polyamide
<b>E (MPa)</b>	2400	3000
<b>v</b>	0.39	0.39
<b><math>\rho</math> (kg/m<sup>3</sup>)</b>	1200	1395
<b>S<sub>y</sub> (MPa)</b>	72	65
<b>S<sub>compressive</sub> (MPa)</b>	86	-

Metals will be needed for high stress parts which are pusher support of Sabot-1, pusher of Sabot-2 and rear part of Sabot-2. Low density, high strength and easy to manufacture material aluminum 7075-T6 is chosen.

**Table 3** Aluminum Properties

	Al 7075-T6
<b>E (MPa)</b>	70000
<b>v</b>	0.29
<b><math>\rho</math> (kg/m<sup>3</sup>)</b>	2700
<b>S<sub>y</sub> (MPa)</b>	553

### 3.3 CALCULATION OF PROJECTILE-SABOT PACKAGE ACCELERATION

Requirement for the tests is to achieve the desired muzzle velocity. When the capabilities of FML and TÜBİTAK-SAGE are considered, limit for maximum muzzle velocity should be determined. Due to the production techniques, material procurement and general test requirements, maximum muzzle velocity is limited to Mach 3. Analysis in the sabot design tool will be performed for velocities between Mach 0.8 and 3.

To reach the desired muzzle velocity, sabot-projectile package is accelerated by the explosion of the gun-powder. Package has a specific velocity profile in the gun tube travel. Pressure changes continuously in the gun. In order to perform the stress analysis, acceleration should be known. Since the system is considered as static, using maximum acceleration that the package reaches will be logical.

‘GPSIM alpha 8.4’ is the tool used for predicting the inbore parameters. It was developed at TÜBİTAK-SAGE. Pressure change in the gun and velocity of the package with respect to time can be obtained from the GPSIM. Inputs of the tool are gun parameters, package mass and the powder mass. Gun parameters are constant and they are given in the following table.

**Table 4** Gun Parameters

Chamber volume (cm <sup>3</sup> ):	7973.2
Gun bore diameter (m)	0.1
Gun bore length (m)	5.5

When the package mass and the charge mass is entered, the program can calculate the muzzle velocity, total travel time in the gun bore and pressure graphs with respect to time. By changing the powder mass, desired velocity can be reached. After achieving the desired muzzle velocity, the aim is to determine the maximum pressure in the tube. The peak point of the pressure vs. time graph shows the maximum pressure value (Figure 72).

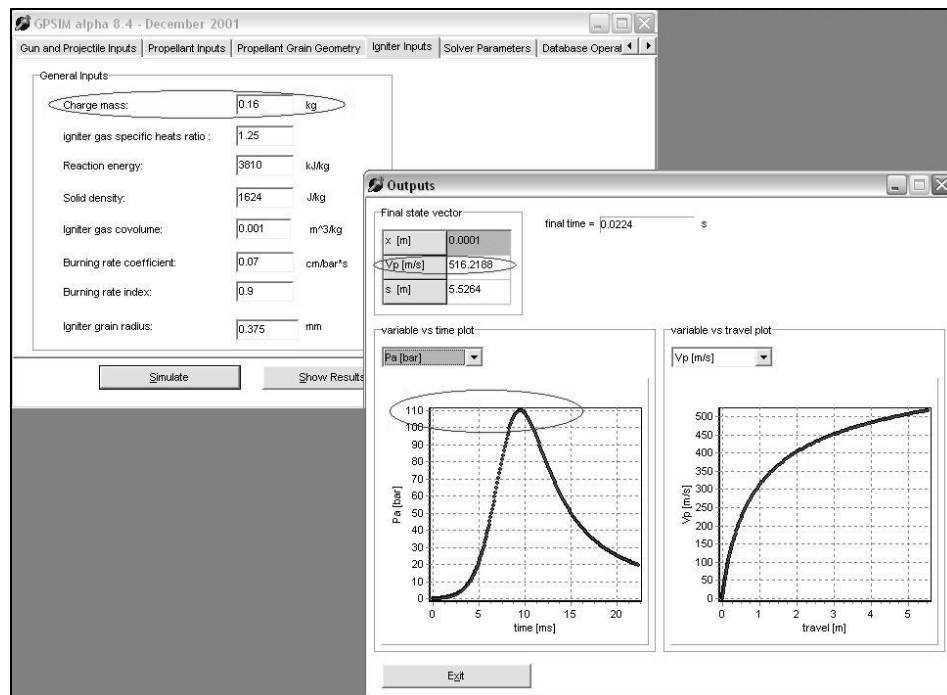


**Figure 72** GPSIM output

In Figure 72, graph at left hand side shows the pressure change. Pressure increases from zero, reaches a peak point and than pressure decreases. The right hand side graph shows the package velocity vs. distance. Package reaches its maximum velocity at the muzzle of the gun. For this situation total travel time is around 22 ms.

Acceleration of the system can be calculated in two different ways. Reference [4] has two definitions for acceleration, constant acceleration and maximum acceleration. Constant acceleration is derived from the conservation of energy. In Equation (66) acceleration definitions are given. Here, 'V' is the muzzle velocity and 'l' is the gun bore length.

$$a_{\text{cnst}} = \frac{1}{2} \frac{V^2}{l} \quad (66)$$

$$a_{\text{max}} = 3 \sim 5 a_{\text{cnst}}$$

Constant number given in the formula which is between 3 and 5, comes from the test experiences [4].

On the other hand maximum acceleration can be calculated from the equilibrium of the forces as given in Reference [3]. Total force acting on the system is the multiplication of the total mass and acceleration.

$$F = P_{\text{max}} A = M_{\text{total}} a \quad (67)$$

Here, maximum pressure is obtained from the GPSIM data. 'A' is the cross section area of the gun bore which equals to the area of the pusher. Thus, maximum acceleration, 'a', is;

$$a = \frac{P_{\max} A}{M_{\text{total}}} \quad (68)$$

With these three definitions, accelerations have been calculated and compared (Equation (69)). Acceleration ‘a’ is between the constant and maximum acceleration results. Calculation of acceleration from the maximum pressure definition seems to be logical for initial guess.

$$a_{\text{cnst}} < a < a_{\text{max}} \quad (69)$$

This acceleration calculation is valid if the friction force is assumed to be zero. But in the previous sections it is mentioned that friction force is important because of the larger diameter of the aft section of the pusher.

According to polycarbonate material ingredients and chemical production processes, different coefficient of frictions are given in the references. Detailed ingredients and chemical components of the polycarbonate material used can not be obtained from the supplier. Since the coefficient of friction value is changing from 0.35 to 0.6, friction coefficient ( $\mu$ ) of the polycarbonate material on the steel is taken as 0.5.

Friction force is the multiplication of the normal force with friction coefficient. Normal force is equal to the force that compresses the pusher diameter to gun bore diameter. Therefore, normal force can be calculated from the radial displacement formula given in Equation (70) [7],

$$u = \frac{1-\nu}{E} P_f r \quad (70)$$

Since the diameter of the gun bore is 100 mm and aft section of the pusher diameter will be 100.5 mm (based on the previous test experiences, to seal the gases 0.5 mm larger diameter is sufficient), then radial displacement 'u' can be calculated. 'r' is the radius of the gun bore, and it is also the radius of the pusher.

$$u = \frac{100.5e^{-3} - 100e^{-3}}{2} \quad (71)$$

$$r = \frac{100e^{-3}}{2}$$

Distributed load resulting due to radial displacement is called as 'Pf'. To calculate the normal stress, distributed load is multiplied with the area. Distributed load acting on the area is  $\pi D t_f$ . Where 'D' is the diameter and 'tf' is the thickness of the pusher part which has larger diameter than the gun bore (Figure 73). As a result, acceleration can be calculated from dynamic equilibrium of the forces acting on the system which is given in Equation (72).

$$P_{\max} \pi \frac{D^2}{4} - F_f = M_{\text{total}} a \quad (72)$$

where;  $F_f = P_f \pi D t_f \mu$

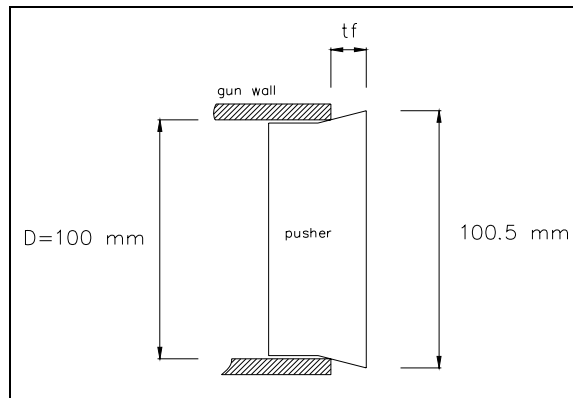


**Figure 73** Pusher at the entrance of the gun

### 3.4 CALCULATION OF PRESSURE

Maximum pressure in the gun is obtained from the output graph of the GPSIM. From the pressure vs. time graph, peak value of the graph shows the maximum pressure. This graph is obtained for a certain package weight and muzzle velocity. On the other hand, in the computer tool, total weight always changes due to iterations. Therefore, it is not possible to input the maximum value. Maximum pressure value should also be found automatically in the sabot design tool.

In order to find a relation between mass and pressure, different cases are simulated in the GPSIM, and mass vs. pressure data are obtained. Simulations are done for different Mach numbers; 0.8, 0.9, 1.2, 2.0, 2.5, 3. For each of the Mach number, fourth order curve is fit to mass vs. pressure graph. An example graph is given for Mach 3 in Figure 74. In the equation on the graph, 'y' refers to pressure and 'x' refers to mass. In the tool with such relations, for a given Mach number maximum pressure can be calculated easily and by this way weight changes can also be taken into account. Pressure equation and mass versus pressure graph for other Mach numbers are given in Appendix A.

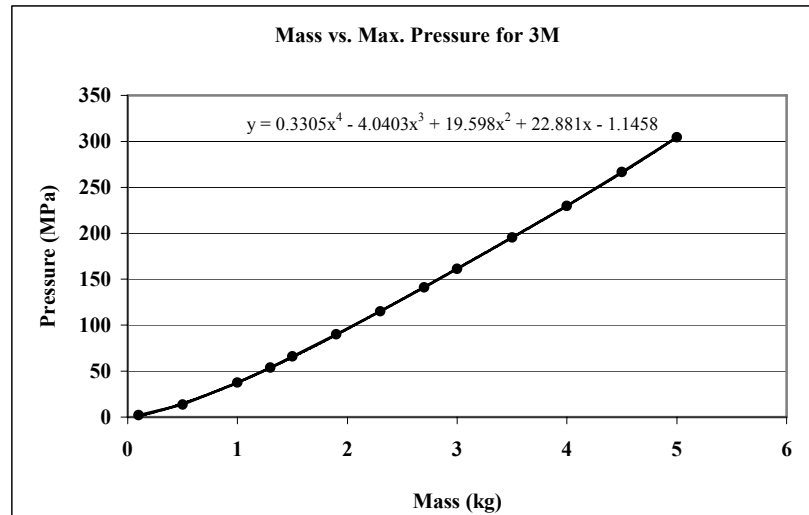


**Figure 74** Mass vs. Max. Pressure graph

### 3.5 CALCULATION OF CORRECTION FACTORS, $c_n$

In this section, calculation of correction factors,  $c_{nA}$  &  $c_{nC}$ , will be explained in detail. To calculate the stresses at the section-1 and section-3 of both sabots, basic strength formulas can be used with some assumptions which were explained in Chapter 2.3.4.1, 2.3.4.3 and 2.3.5.1. From the finite element analysis it has been seen that these formulas have some errors for some cases. Therefore, a correction factor,  $c_n$ , is needed. For different cases, stress has been calculated from the approximate relations and also obtained by the finite element method. Then, the ratio of the finite element analysis solution to the result obtained by approximate strength of materials approach has been determined. This ratio is then used as the correction factor  $c_n$ .

$$c_n = \frac{\text{Finite element analysis}}{\text{Approximate strength of materials solution}} \quad (73)$$

### 3.5.1. Sabot-1 Correction Factors

For Sabot-1, two correction factors are needed for two regions to calculate the stresses. These critical regions are section-1 and section-3.

#### 3.5.1.1. Section-1

Section-1 correction factor is  $c_{nA}$ . Stress at this section depends on the parameters 'A', 'L' and 'B' (Figure 75). Approximately 40 cases have been analyzed by finite element analysis; an example image is given in Figure 76. In these analyses only section-1 is modeled for reducing the FEA calculation time. The cut region at section-2 is clamped and inertial load is applied. Stresses are calculated by the formula for each of them. Then correction factor is obtained from Equation (73).

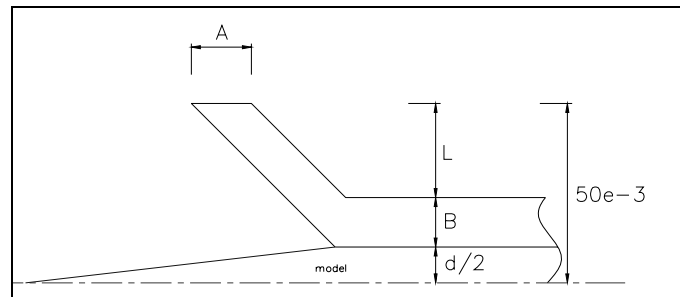


**Figure 75** Section-1 correction factor calculation

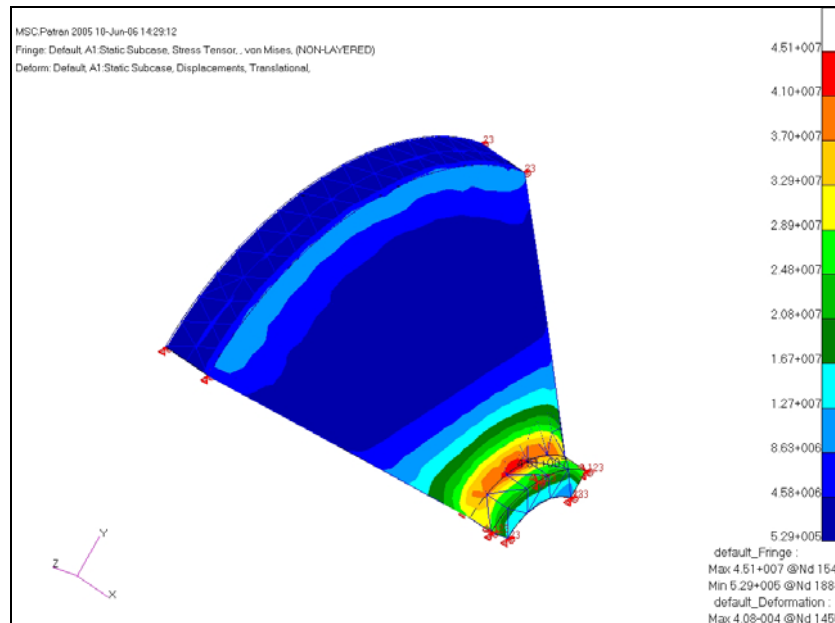


**Figure 76** An example finite element analysis for  $c_{nA}$

From the analysis it has been concluded that when thickness of the section-1 is increased, stress also increases with thickness linearly. In the design tool, for different 'A', 'B' and 'L' values, correction factor  $c_{nA}$  should be calculated automatically.  $c_{nA}$  depends on three parameters. The way to calculate  $c_{nA}$  easily is to find a function  $f(A,L)=c_{nA}$  for different 'B' values (2.5, 5, 10, 15 and 20 mm). This function forms a surface in the space. Equation of this surface, which is  $f(A,L)$ , is obtained from the TableCurve 3D Version3.12 tool. An example is given for B=15 mm;

**Table 5** A, L and  $c_{nA}$  values for B=15 mm

A	L	$C_{nA}$
3.00E-03	1.00E-02	0.49
3.00E-03	2.00E-02	0.20
3.00E-03	3.00E-02	0.08
3.00E-03	3.25E-02	0.07
1.00E-02	1.00E-02	1.47
1.00E-02	2.00E-02	0.60
1.00E-02	3.00E-02	0.26
1.00E-02	3.25E-02	0.21

‘A’ has two values; 3 mm and 10 mm. these are the logical maximum and minimum values that ‘A’ can have. Since stress is changing linearly, maximum and minimum values are enough to calculate any mid values. The equation of the surface formed by the data given in Table 5, is;

$$\ln(c_{nA}) = a + b[\ln(A)]^2 + ce^{(-L)} \quad (74)$$

where constants are;

$$a = -86.241$$

$$b = -0.0881$$

$$c = 89.357$$

This type of equation is obtained, for five values of ‘B’. Then an interpolation is made in the tool, if ‘B’ is different from the given five values. Equations for other ‘B’ values are given in Appendix B.

### 3.5.1.2. Section-3

The procedure is same as section-1. Since geometry and loading are different, equations of constant  $c_{nC}$  will be different. The way to reduce the stress in the critical region is to increase the thickness 'C'. Iterations in the tool start at minimum thickness to achieve the minimum weight. Therefore, 'C' is increased gradually until desired stress is obtained. 'C' and stress is not related linearly. Thus calculations are needed for more than two values of 'C'. Again for this section, stress depends on three parameters; 'B', 'L' and 'C'. As a result, approximately 100 cases are calculated and analyzed by finite element software.

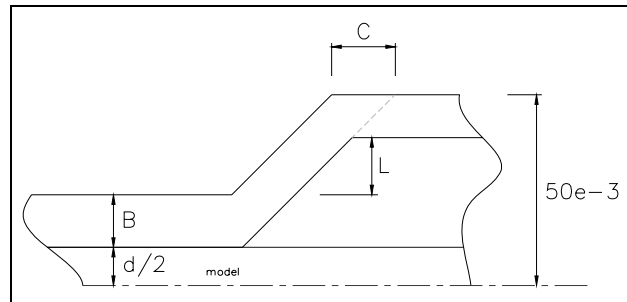


**Figure 77** Sabot-1 section-3 correction factor calculation

Results for B=15 mm is given in the following table, as an example;

**Table 6** A, L and  $c_{nC}$  values for B=15 mm

C	L	$c_{nC}$
5.00E-03	5.00E-03	3.34
5.00E-03	3.00E-02	17.49
7.00E-03	5.00E-03	1.79
7.00E-03	3.00E-02	13.00
1.00E-02	5.00E-03	1.69
1.00E-02	3.00E-02	7.15
1.50E-02	5.00E-03	1.35
1.50E-02	3.00E-02	5.36
2.00E-02	5.00E-03	1.03
2.00E-02	3.00E-02	3.45
2.50E-02	5.00E-03	0.80
2.50E-02	3.00E-02	3.03

Equation of the surface which is formed by these values is;

$$\ln(c_{nC}) = a + b \ln(C) + c \ln(L) \quad (75)$$

where constants are;

$$a = 0.3679$$

$$b = -1.1574$$

$$c = 1.0268$$

Equations for other 'B' values are also given in Appendix B.

### 3.5.2. Sabot-2 Correction Factors

Like Sabot-1, two regions of Sabot-2 needs correction factor for stress calculations.

### 3.5.2.1. Section-1

$c_{nA}$  is totally same with Sabot-1. There is no difference between the sabots. Therefore, equations for Sabot-1 can be used for Sabot-2.

### 3.5.2.2. Section-3

For this section, approximately 20 cases were analyzed. It is concluded that stress does not change with thickness 'C' linearly. In addition to that, minimum stress is not achieved with maximum thickness. Finite element analysis stress results with respect to thickness 'C' are given in Figure 78 for different 'B' values.

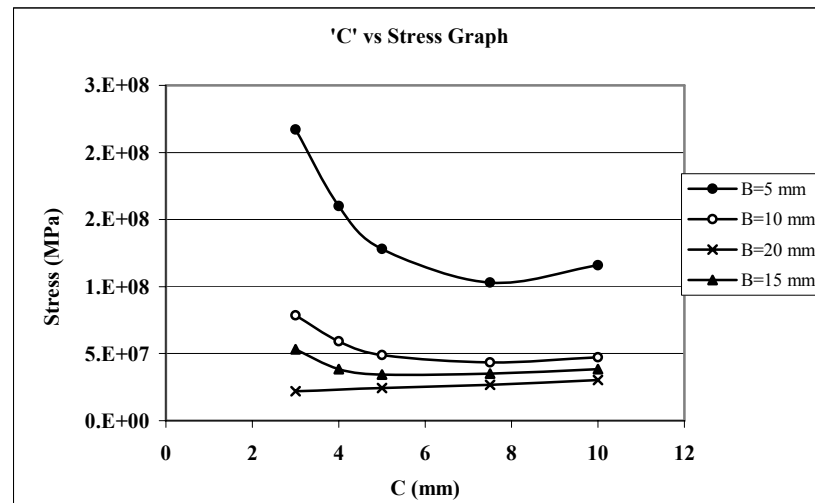


**Figure 78** FEA results for section-3 of Sabot-2

It is seen that from Figure 78, minimum stress for a 'B' value is obtained at a certain value of 'C'. In other words, stress is not inversely proportional with thickness 'C'. From these results, a relation can be derived to find the suitable 'C' value which gives the minimum stress for a given 'B' or 'L' value. Therefore,

thickness 'C' can easily be calculated by using this relation which is given at Equation (76).

$$C = -1.66L^2 + 0.2724L - 0.0007 \quad (76)$$

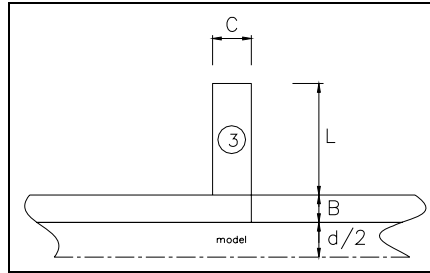


**Figure 79** Sabot-2 section-3 correction factor calculation

Thickness 'C' is related only with 'L' and therefore stress is related only with 'L'. Thus, constant  $c_{nC}$  is the function of 'L' only. Equation for  $c_{nC}$  is derived as ;

$$c_{nC} = -21.27L + 1.2538 \quad (77)$$

### 3.6 ITERATIONS

For two different sabot geometries, two different sabot design tools are developed. In each tool, different iteration procedures are involved because of the geometries, materials used etc.

### 3.6.1. Sabot Design Tool for Sabot-1

The aim is to make the sabot as thin as possible to reduce the weight of the sabot and pusher. Therefore, SDT starts its calculations from an initial guess. Sabot thicknesses 'A', 'B', 'C' and pusher thickness initially have minimum values. This initial value is 4 mm which is decided according to production limits and flexibility characteristics of polycarbonate material. Modification 'AB' is zero initially. Initial thickness of the support plate is 2 mm and diameter is 10 mm greater than the model diameter. Other inputs of the SDT are;

- Material Properties
  - Polycarbonate density
  - Polycarbonate Poisson's ratio
  - Polycarbonate yield stress
  - Polycarbonate modulus of elasticity
  - Polycarbonate friction coefficient
  - Aluminum density
  - Aluminum yield stress
- Model properties
  - Diameter
  - Length of the rod
  - Fin chord
- General parameters
  - Diameter of the bore
  - Thickness of the pusher which has a larger diameter than gun bore ( $p_i$ )
  - Horizontal distance between the fin and the section-3 ( $p$ )
  - Mach number

As it is seen in the following figure, section-2 and section-4 have the same thicknesses, 'B'. This is done on purpose to reduce the iteration process.

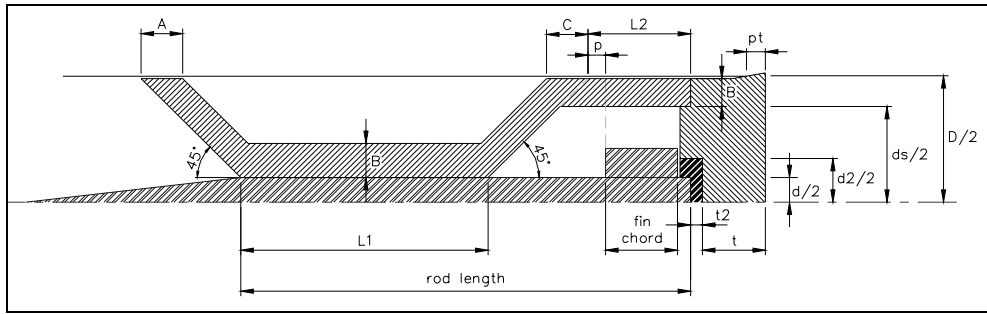


**Figure 80** Inputs for Sabot-1

All of the parameters are known and used for initial volume calculation. These parameters are given in Figure 80. From the material properties and calculated volume, total sabot mass can be obtained. Thus, total mass of the system and the desired velocity is known. Maximum pressure can now be obtained from the pressure functions which are explained in Chapter 3.3. Finally, acceleration can be easily calculated by using Equation (72).

For these initial values, stresses at the critical regions are calculated in SDT. As mentioned in the previous chapters, critical regions are;

- Section-1 & Section-2 intersection: related parameters are 'A' and 'AB'.
- Section-2: related parameter is 'B'.
- Section-2 & Section-3 intersection: related parameter is 'C'.
- Section-4: related parameter is 'B'
- Pusher: related parameter is 't'
- Pusher support: related parameters are 't2' and 'd2'.

Calculated combined stresses are then compared with the design stress. In missile technology, structural design safety factor has a range between 1.1 and 1.5 [18]. Since sabot-model packages in this study do not have interface with humans during firing and also do not contain warheads, the safety factor for the calculations is taken as 1.2 for initial start point. This safety factor is applied to the yield stress of

the polycarbonate and aluminum. Design stress is calculated by dividing the yield stress of the material to safety factor.

For a given 't', 't2' and 'd2' values, sabot thicknesses are iterated until the stresses become smaller than the yield stress. During the iteration process for sabot design, parameters 'B', 'C' or 'AB' are increased to reduce the stress. Thus, total weight of the system also changes, and this directly affects the pressure and acceleration. In all of the iteration loops, pressure is updated every time a new mass is determined.

When the iteration finishes for the sabot, pusher stress calculation starts. If stress is high for the pusher, then thickness of the pusher is increased one step. According to the outcome of the calculations, thickness of the pusher support may also be increased. From this point, for a new pusher thickness, sabot loops starts to calculate the appropriate sabot thicknesses. To summarize, there is a main loop for the pusher and in this loop there is another loop for sabot.

Unless the main loop reaches a solution, SDT starts to increase the diameter of the pusher support. This means that in the given thickness limit for the polycarbonate pusher, pusher may not satisfy the conditions. This is why the support diameter is increased.

These iteration loops work continuously until all the stress conditions are satisfied. Flow chart of the tool for Sabot-1 which summarizes the above paragraphs is given in Figure 81.

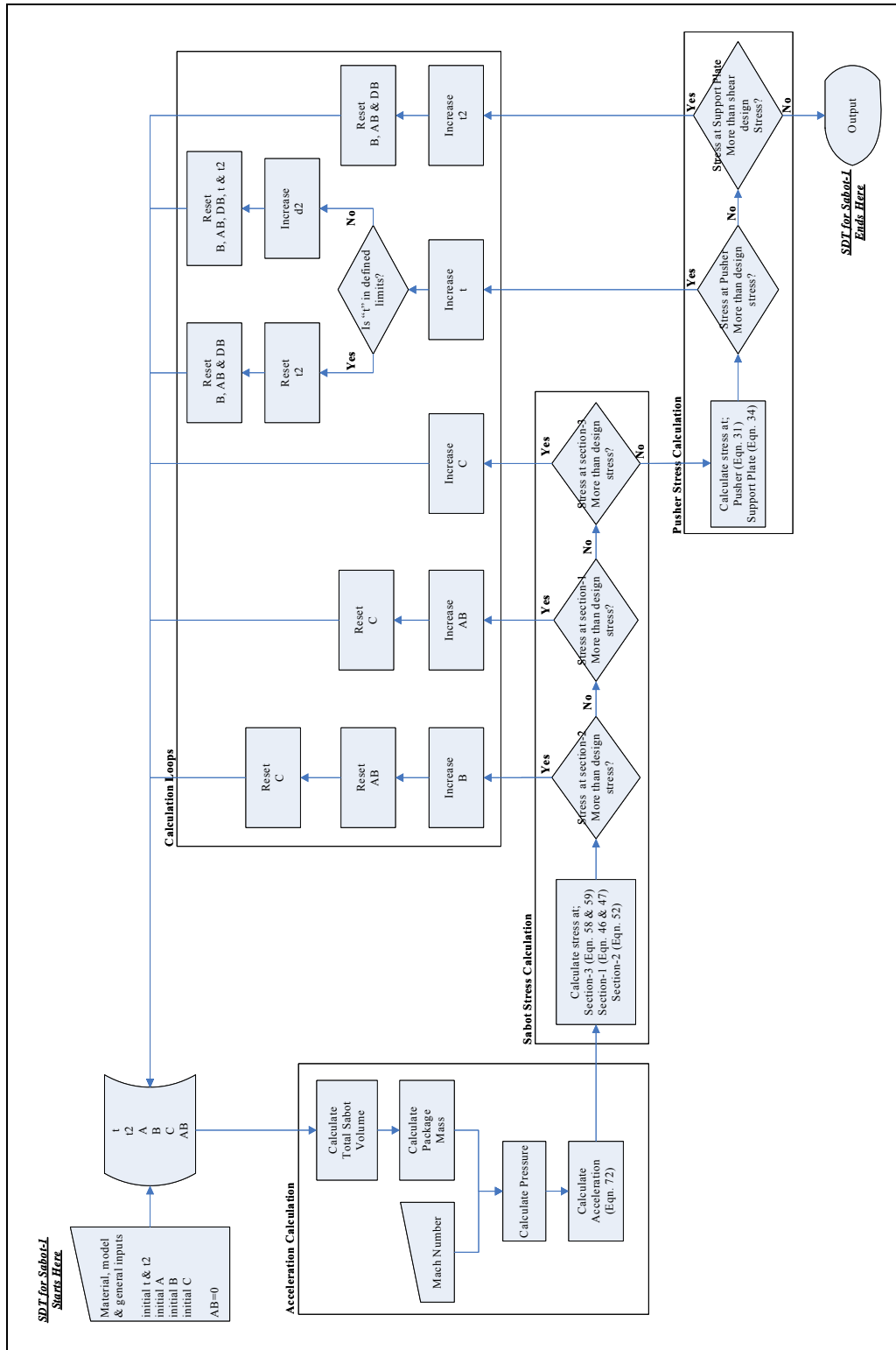
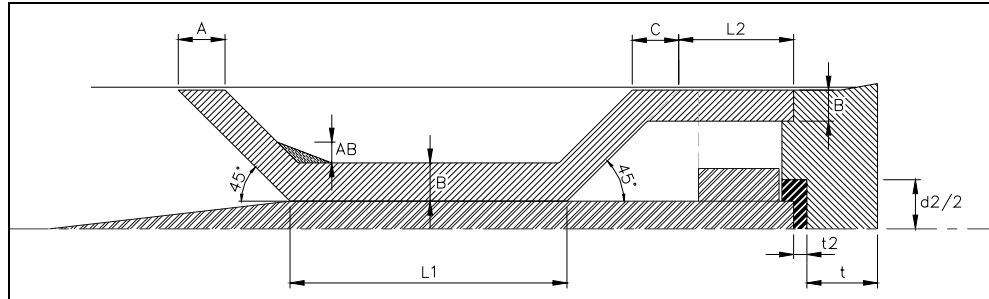


Figure 81 Flow Chart of SDT for Sabot-I

Finally, the tool gives the values for the parameters which determine the geometry of the sabot. Output of the tool is given as a schematic drawing in Figure 82.



**Figure 82** Output of SDT for Sabot-1

### 3.6.2. Sabot Design Tool for Sabot-2

Calculation and iteration principle is similar to Sabot-1 tool. Pusher thickness, 'A' and 'B' have initial values. 'C' is calculated by using 'B'. 'AB' and 'D' modifications are initially zero. Inputs of the Sabot-2 SDT are given in the following list and shown in the Figure 83 and Figure 84;

- Material Properties
  - Polycarbonate density
  - Polycarbonate Poisson's ratio
  - Polycarbonate yield stress
  - Polycarbonate modulus of elasticity
  - Polycarbonate friction coefficient
  - Aluminum density
  - Aluminum Poisson's ratio
  - Aluminum yield stress
- Model properties
  - Diameter

- Length of the rod
- Fin chord
- Fin thickness
- CG position
- General parameters
  - Diameter of the bore
  - Thickness of the pusher which has a larger diameter than gun bore ( $p_i$ )
  - Radial distance between the fin and Sabot-2 metal part ( $f_p$ )
  - Distance between the fin and the cavity start point ( $p$ )
  - Mach number

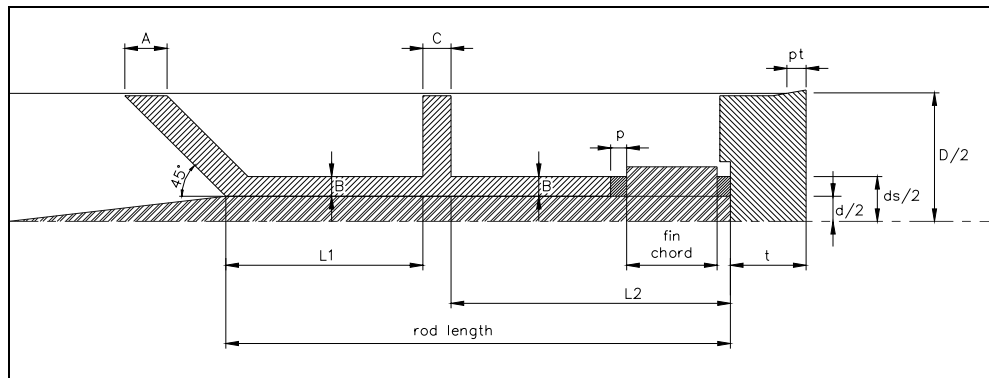


**Figure 83** Inputs for Sabot-2

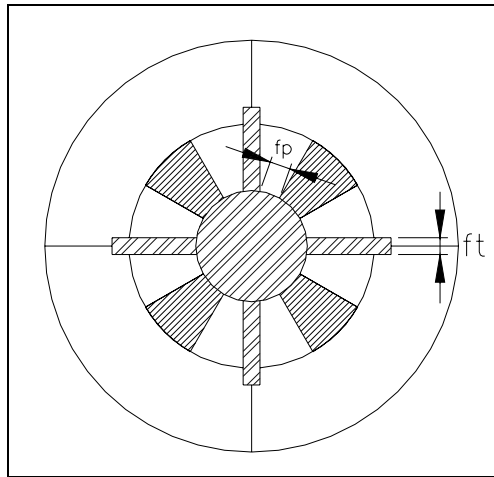


**Figure 84** Inputs for Sabot-2, back view

After all the iterations, when all the stresses satisfy the failure criteria, SDT gives geometric parameters as an output which is given in Figure 85.

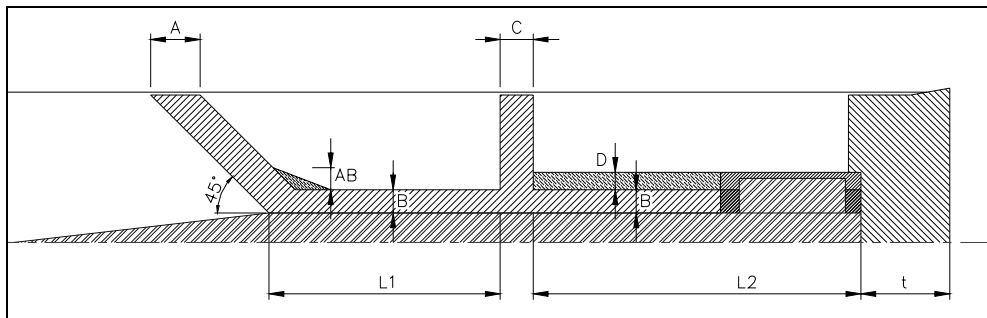


**Figure 85** Output of SDT for Sabot-2

Flow chart of the Sabot Design Tool for Sabot-2 is given Figure 86.

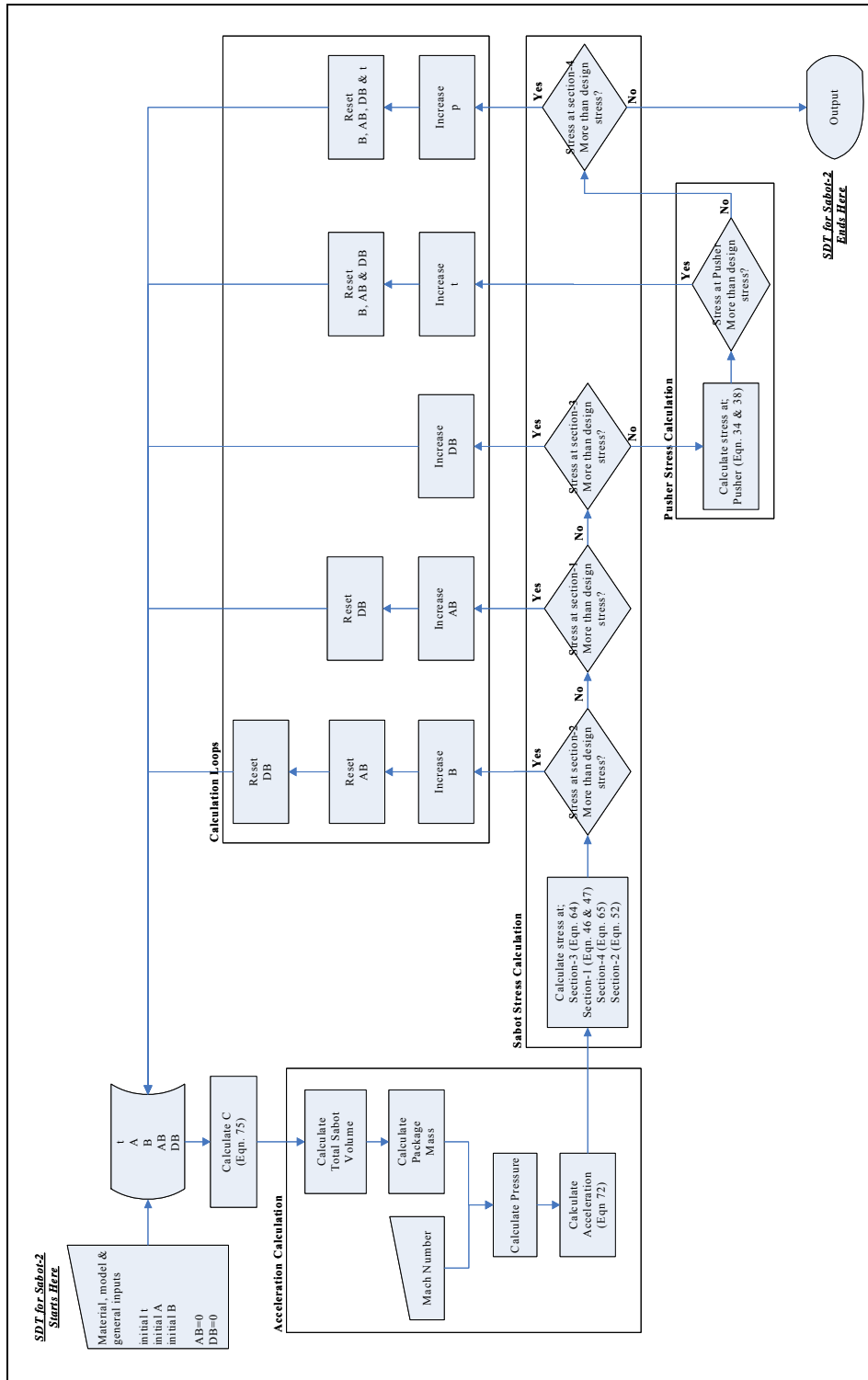


Figure 86 Flow Chart of SDT for Sabot-2

## **CHAPTER 4**

### **VERIFICATION OF THE SABOT DESIGN TOOL**

It is necessary to verify whether the outputs of the SDT are reliable or not. There are two verification methods. First one is to perform finite element analysis for the output of the SDT. The other one is to produce and test the sabots physically. In this study the SDT has been tested with both of the methods. Finite element analysis shows that formulations which are derived and modified for stress analysis are reliable. The physical tests, in other words FML tests, indicated that the assumptions due to uncertainties in the gun are correct.

#### **4.1 TEST MODELS**

Models which fit to the assumptions during the design of Sabot-1 & 2 are selected for analysis and test verification studies. Thus, models must have axially constant radius. On the other hand, to produce a test model, money and time is needed. Therefore, using the models which are available in the FML inventory would be better.

According to the reasons explained in the previous paragraph, two different projectiles have been chosen. First one is the model of an unguided artillery rocket, 'TOROS'. Second one is 'BASIC WAF' which is mostly used model in aeroballistic range testing. WAF is the abbreviation of 'wrap around fin'. Properties of the models are given in Table 7.

**Table 7** Model Specifications

	TOROS	BASIC WAF
Mass (gr)	500	451
Diameter (mm)	20	20
CG (mm)	185	88
Rod Length (mm)	268	158
Chord Length (mm)	57	35
Fin Thickness (mm)	5	5

In the following figure, pictures of the models are shown. The model on the left is TOROS and the one on the right is BASIC WAF. Both of them has wrap around fin. TOROS model is designed for high muzzle velocities. Therefore, different metal materials are used. For the aft region special design is made to resist high stresses.



**Figure 87** TOROS and BASIC WAF models

## 4.2 TEST CASES

Several tests can be performed for verification and also for obtaining data for better sabot designs in the future. However, test cases were reduced according to the cost of tests and time. The FML tests can be performed with at least 3 engineers and 1 technician. Therefore, work force should also be considered. Minimum amount of test cases with efficient test configurations have been decided. Test plan is given in the following table.

**Table 8** Test Cases

Case No.	Model	Mach	Sabot Type	Number of Tests
1	Basic WAF	0.8	Sabot-1	3
2	Basic WAF	2	Sabot-2	4
3	Toros	2	Sabot-1	4
4	Toros	2	Sabot-2	3

There are two different models and two different sabots. 0.8 Mach muzzle velocity is usually used for testing subsonic aircraft munitions models in FML. Mach 2 is relatively high speed according to the tests performed in the past. Case 1 and 4 have been repeated 3 times at the same conditions and case 2 and 3 have been repeated 4 times to obtain reliable test results.

Inputs of the SDT are model parameters, material properties, general parameters (Table 9), and Mach number. Parameters in Table 9 have been explained in Chapter 3.6.

**Table 9** General Inputs for the Tool

	Sabot-1	Sabot-2
<b>fp (mm)</b>	-	3
<b>Factor of Safety</b>	1.2	1.2
<b>Design Stress</b>	Sy/1.2	Sy/1.2
<b>Friction Coeff.</b>	0.5	0.5
<b>pt (mm)</b>	6	6
<b>p (mm)</b>	0	20

Output of SDT for every test case is given in the following tables. These results are enough to obtain a three dimensional model of the pusher and sabot. Therefore, with these results finite element analysis and FML tests can be performed.

**Table 10** Tool Output – General

Case No.	Mach	L1 (mm)	L2 (mm)	Sabot Mass (gr)	Pusher Mass (gr)	Model Mass (gr)	Total Mass (gr)	Max. Acceleration (m/s <sup>2</sup> )
<b>1</b>	0.8	83	35	190.0	170.6	451.0	811.6	3.307E+04
<b>2</b>	2	67	85	281.8	284.2	451.0	1017.0	1.186E+05
<b>3</b>	2	171	57	725.4	300.1	500.0	1526.0	1.300E+05
<b>4</b>	2	80	182	406.4	313.9	500.0	1220.0	1.231E+05

**Table 11** Tool Output – Pusher

Case No.	Polycarbonate Thickness (mm)	Aluminum Thickness (mm)	Aluminum Support Diameter (mm)
<b>1</b>	17.7	2.0	30
<b>2</b>	-	13.4	-
<b>3</b>	31.4	2.2	30
<b>4</b>	-	14.8	-

**Table 12** Tool Output – Sabot

Case No.	A (mm)	B (mm)	C (mm)	AB (mm)	D (mm)
1	4.00	5.54	4.00	0.00	-
2	4.00	9.90	5.99	0.00	0.00
3	4.00	11.42	27.00	0.00	-
4	4.00	10.18	5.94	0.00	0.00

Parameters ‘AB’ and ‘D’ are calculated as 0 mm in test cases. Since test cases are analyzed up to Mach 2, it means that these modifications are not needed for these test conditions. But, it will be seen that in the next chapter, after Mach 2 analyses ‘AB’ and ‘D’ has certain values.

### **4.3 FINITE ELEMENT ANALYSES**

Finite element analyses have been applied to test cases 1, 3 and 4. Three dimensional modeling of the parts have been done by Mechanical Desktop 2004 DX software. Sabots have been designed to resist the expected loading conditions. Thus, based on finite element analyses it is expected to see whether stress at critical regions will be higher than yield stress or not.

#### **4.3.1. MSC NASTRAN<sup>®</sup>/PATRAN<sup>®</sup> Analyses**

Static stress analyses were performed on the sabots by the help of the MSC NASTRAN<sup>®</sup>/PATRAN<sup>®</sup> software. STEP format was needed to transfer the geometries which were designed by Mechanical Desktop 2004 DX to MSC NASTRAN<sup>®</sup>/PATRAN<sup>®</sup> software. Sabots are clamped at their back faces. The contact surfaces with projectile and the gun are fixed radially and set free in axial direction. Loading is applied as inertial force. Maximum acceleration obtained from SDT is applied to the models.

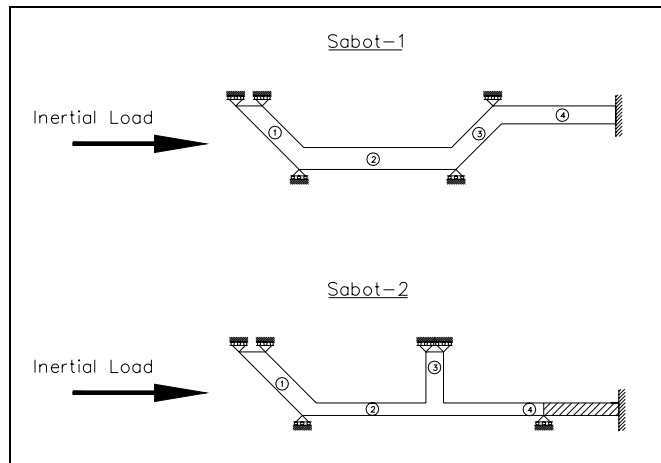


**Figure 88** Loading and boundary conditions for FEA

Since analysis is applied to three dimensional solid models, tetrahedral elements have been used for meshing. Tet10 has been selected for analysis which is one of the MSC PATRAN tetrahedral elements (Figure 89). It is ten noded quadratic element. Tet10 is used for Auto TetMesh approach which is a technique for meshing solid geometries.

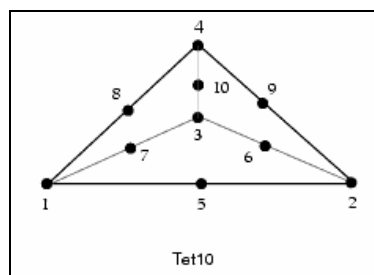


**Figure 89** Tet10 element

Figures given in the following sections are von Misses stress plots of the sabots for sample cases. Unit of the scale on the figures is Pa and shows the stresses of the chosen meshes or whole model.

### 4.3.1.1. Test Case 1

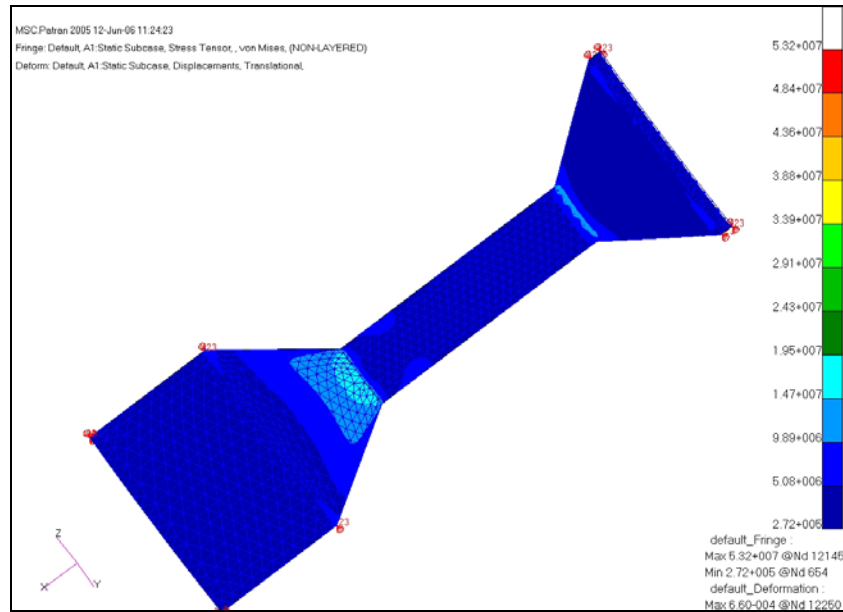


**Figure 90** Test Case 1; Top view of Sabot-1

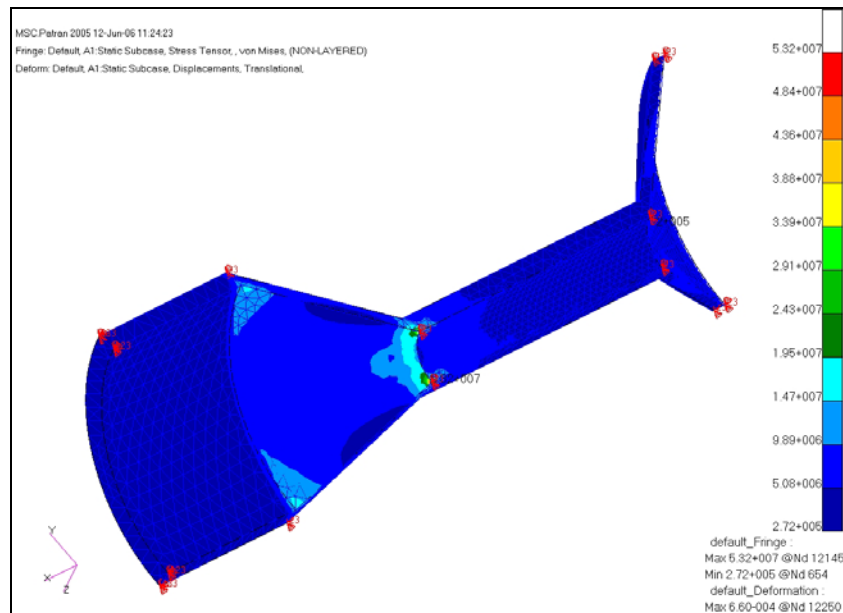


**Figure 91** Test Case 1; Bottom view of Sabot-1

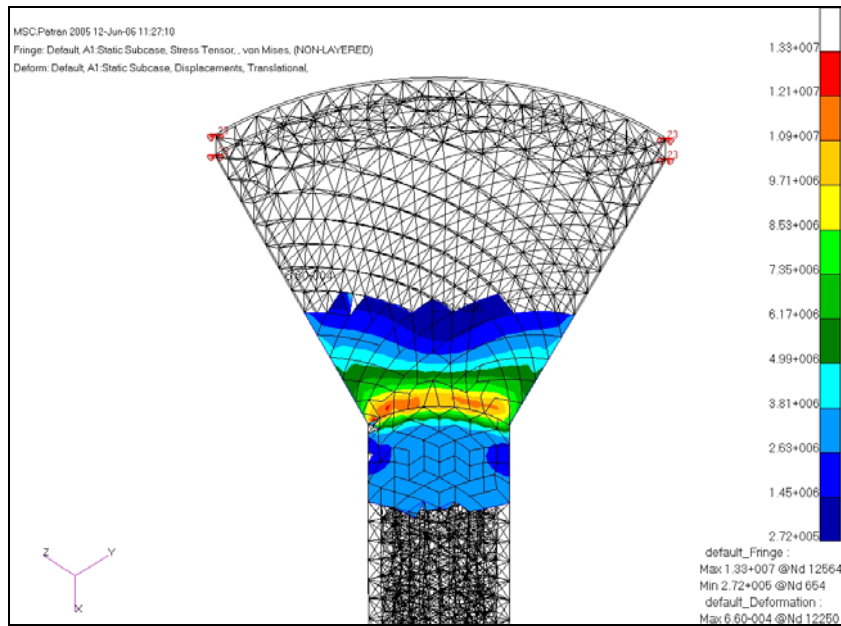


**Figure 92** Test Case 1; Section-1 view of Sabot-1

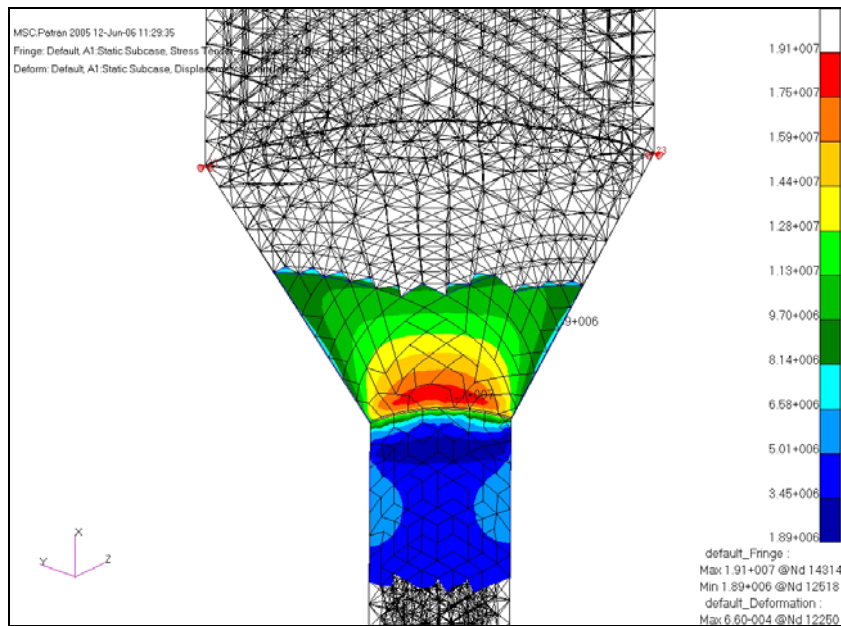


**Figure 93** Test Case 1; Section-3 view of Sabot-1

### 4.3.1.2. Test Case 3

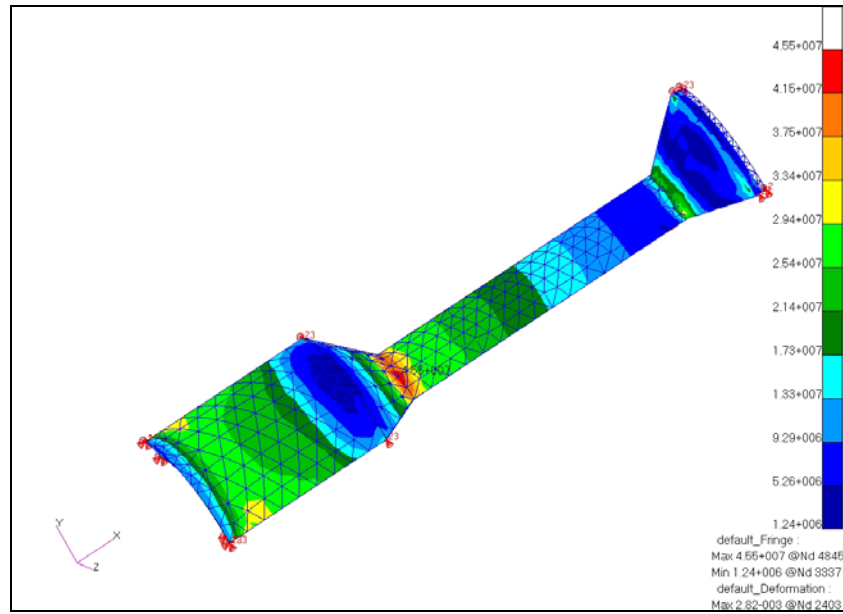


**Figure 94** Test Case 3; Top view of Sabot-1

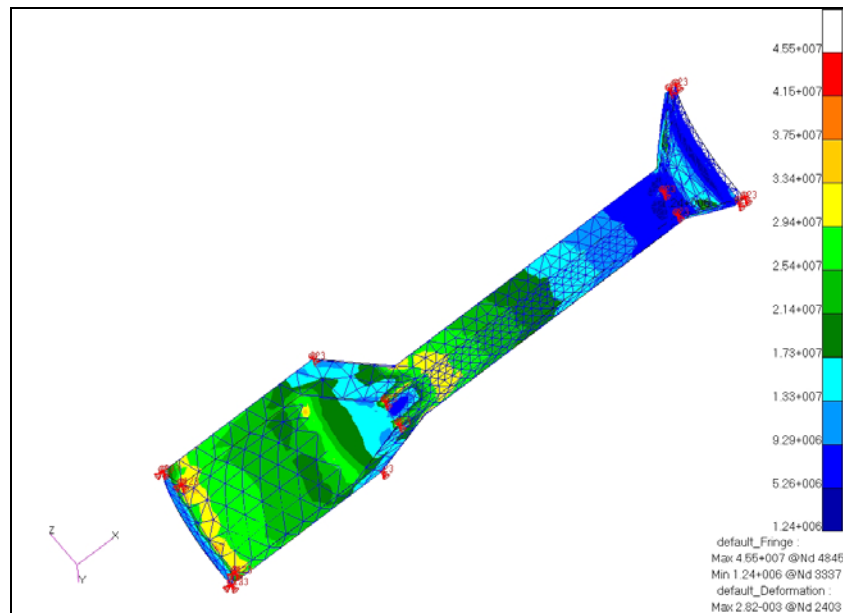


**Figure 95** Test Case 3; Bottom view of Sabot-1

### 4.3.1.3. Test Case 4

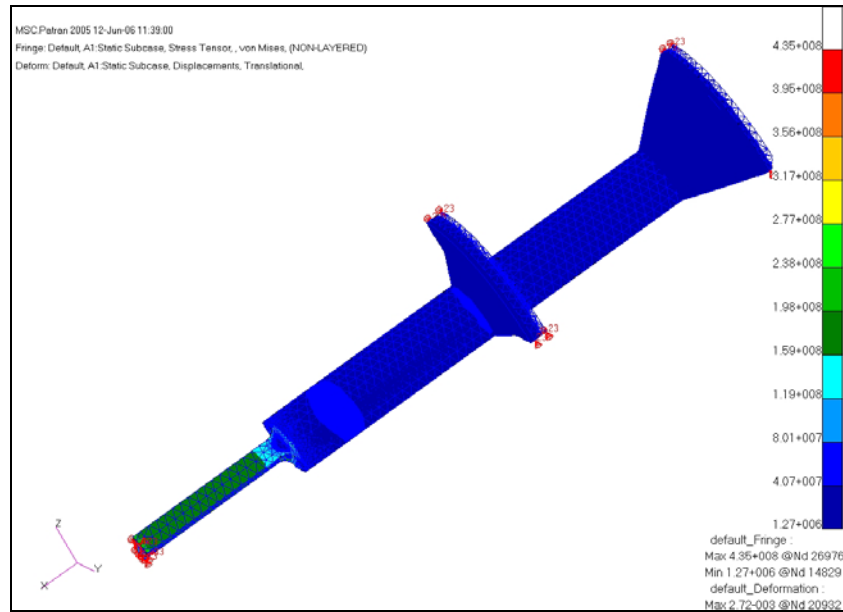


**Figure 96** Test Case 4; Top view of Sabot-2

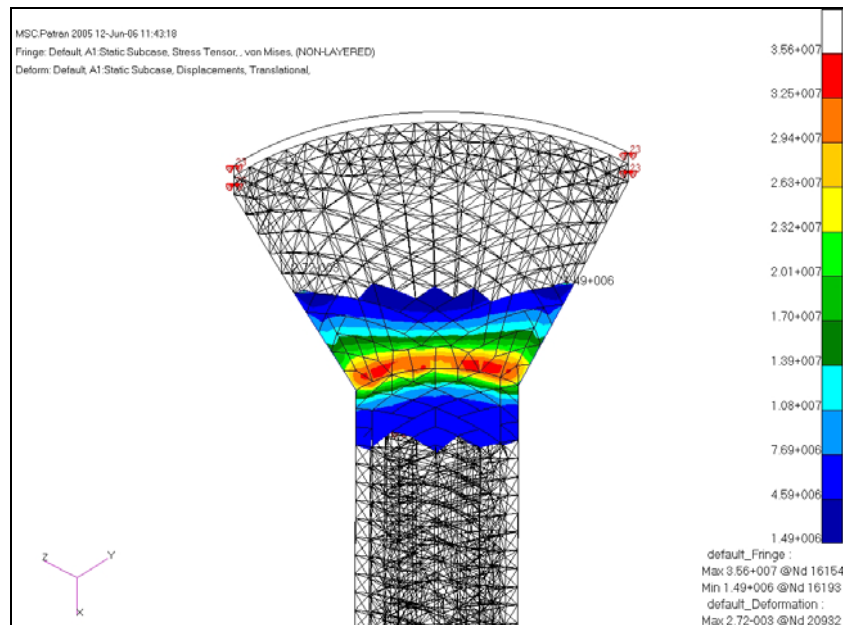


**Figure 97** Test Case 4; Section-1 view of Sabot-2

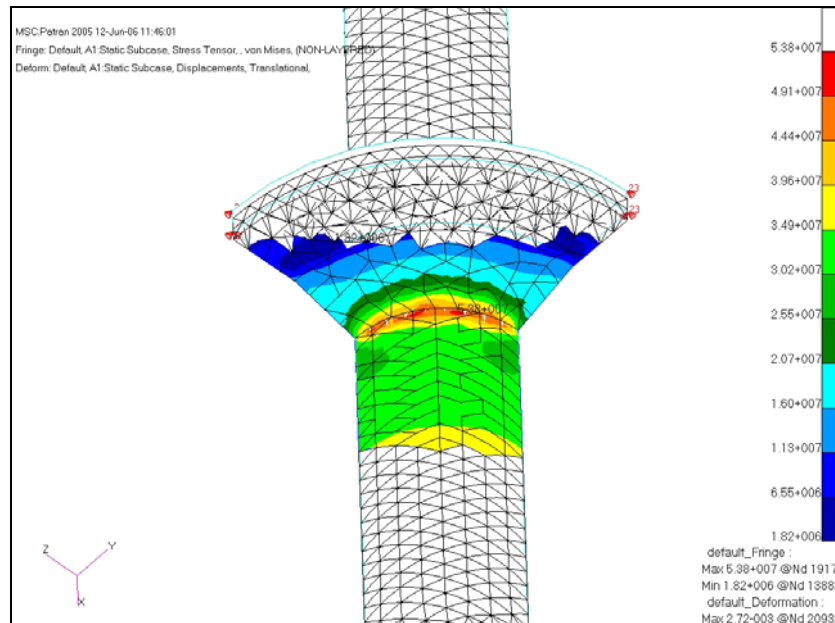


**Figure 98** Test Case 4; Section-3 view of Sabot-2

#### 4.3.2. DISCUSSION OF STATIC FEA RESULTS

From the von Mises stress plots, it can be clearly seen that maximum stresses on the sabots are not higher than design stress. In the SDT analysis, design was performed for 1.2 safety factor. Yield stress of polycarbonate is 72 MPa, when safety factor is applied design stress becomes 60 MPa. For aluminum design stress is 460 MPa.

For Test Case 1, SDT has given minimum limit value, which is 4 mm, for sabot thicknesses. From finite element analysis, maximum stress at critical regions for Test Case 1 is 19 MPa; this is why the SDT did not increase the thicknesses. Stress plots show that maximum stress occurs at section-3 at Test Case 4 as expected and maximum value is 53 MPa. Aluminum part of Sabot-2 of test case 4 has approximately 230 MPa compressive stress.

Static finite element analyses results shows that expected critical regions are correct and calculated stress at SDT are consistent with finite element results.

#### **4.3.3. MSC MARC<sup>®</sup>/MENTAT<sup>®</sup> Analysis**

Finite element analysis for pusher has only been done for test case 3 by MSC MARC<sup>®</sup>/MENTAT<sup>®</sup>. The sabot-projectile package is in motion in the gun bore. Loads acting on the package are changing as the package travels in the gun bore. Since the nature of the package motion and loading are time dependent, transient analysis gives sufficient information about the stresses on the pusher. In transient analysis of test case 3, pusher, sabot, model and gun bore have been modeled and analyzed.

Chamber pressure with respect to total travel time is necessary for transient analyses. Pressure data has been taken from the GPSIM (Figure 99). Two dimensional drawing was enough for finite element modeling, since analysis assumption was axisymmetric analysis. To import the two dimensional drawing of the package and the gun tube into the MSC MARC<sup>®</sup>/MENTAT<sup>®</sup>, IGES format has been used.

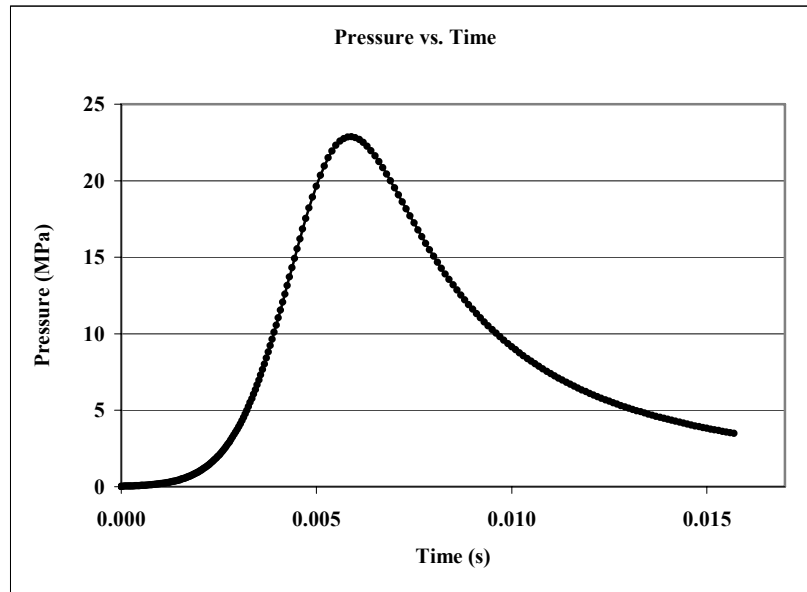


**Figure 99** Pressure vs time graph

Since model is two dimensional, two dimensional elements have been used for meshing. “Element type 10” has been selected because it is four noded quadrilateral element written for axisymmetric applications. This element is preferred when used in contact analyses [17].

In Figure 100, load and boundary conditions are shown. Displacement of the centerline in y-direction is restricted. For transient analysis 5 parts were modeled; sabot, pusher, support plate, model and gun wall. The contact surfaces among the parts are given in Figure 101. Between pusher and gun wall, friction coefficient is defined in the software and effect of friction has been obtained. Also between pusher and support plate, nodes on the contact surface are bounded to each other. Other parts are defined as simply contact bodies.

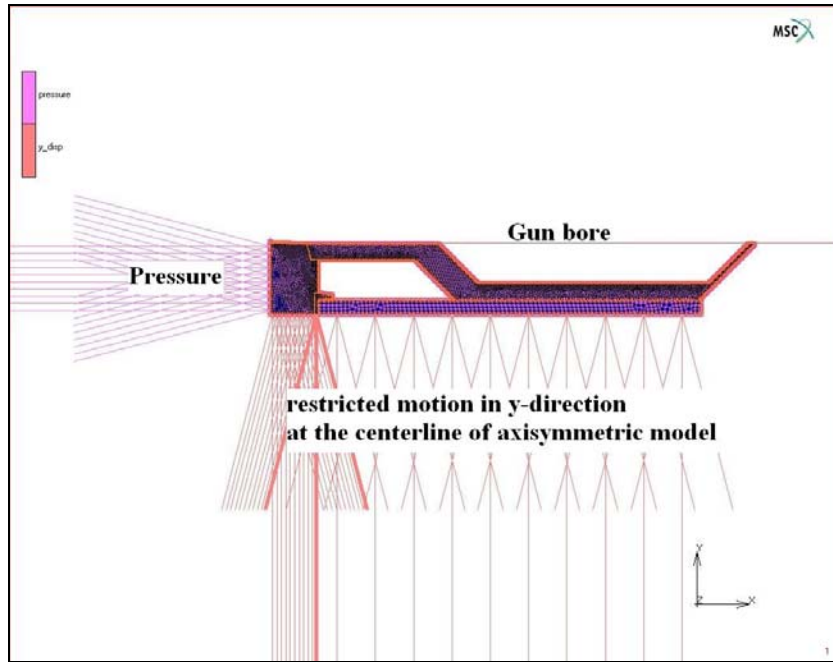


**Figure 100** Test Case 3 boundary condition and loading

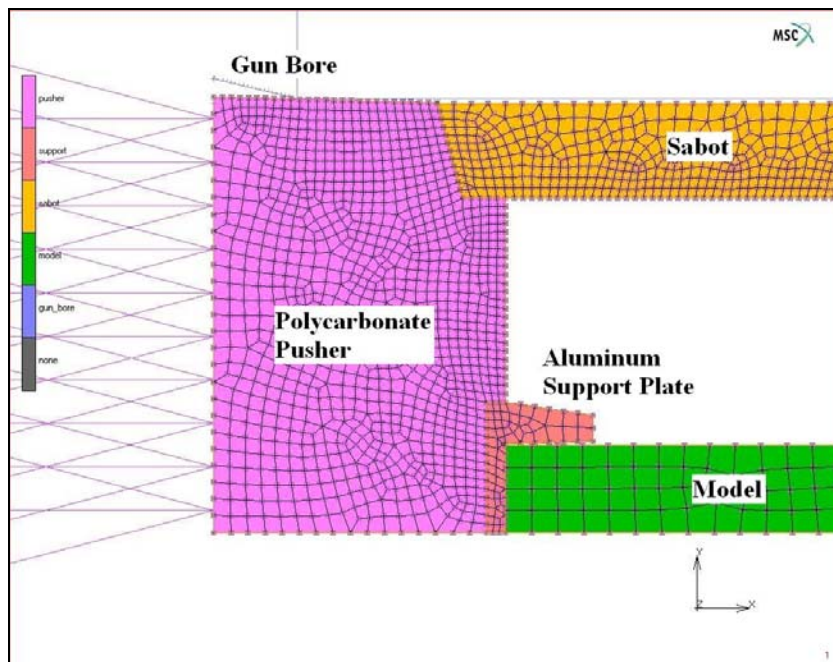


**Figure 101** Test Case 3 contact surfaces and materials

The transient analysis can be verified by investigating the acceleration and velocity graphs of the package. Pressure vs. time graph (Figure 99) which is taken from GPSIM, shows that travel time in the gun is about 0.015 seconds. Desired velocity is Mach 2 which corresponds to approximately 680 m/s. Travel time and velocity information can be seen from the output graph of MSC MARC<sup>®</sup>/MENTAT<sup>®</sup> software (Figure 102). Maximum acceleration calculated by the SDT for this case is  $1.3E5 \text{ m/s}^2$ . From Figure 103, maximum acceleration determined as a result of transient analysis performed by MSC MARC<sup>®</sup>/MENTAT<sup>®</sup> is seen as  $1.16E8 \text{ mm/s}^2$ . We know that for the maximum acceleration calculation, there are different formulations and some of them depend on empiric constants. From the comparison of accelerations, it can be concluded that SDT gives sufficient and satisfactory acceleration results.

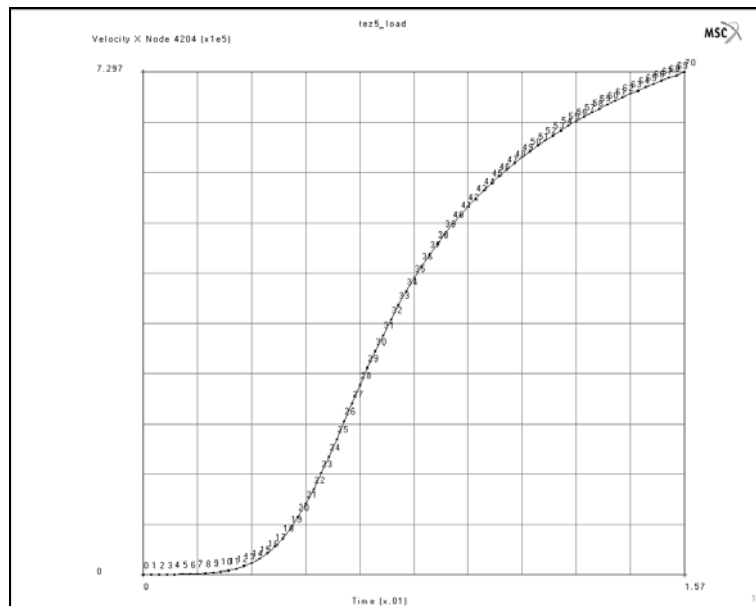


**Figure 102** Package velocity profile

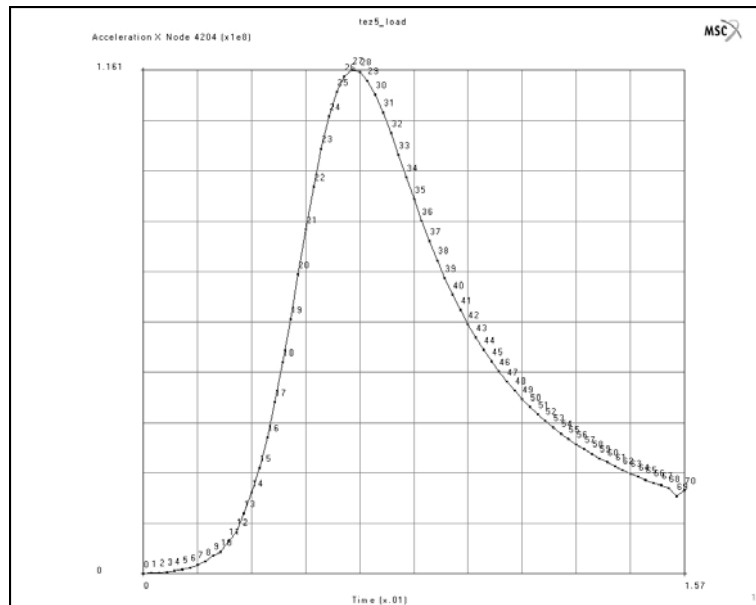
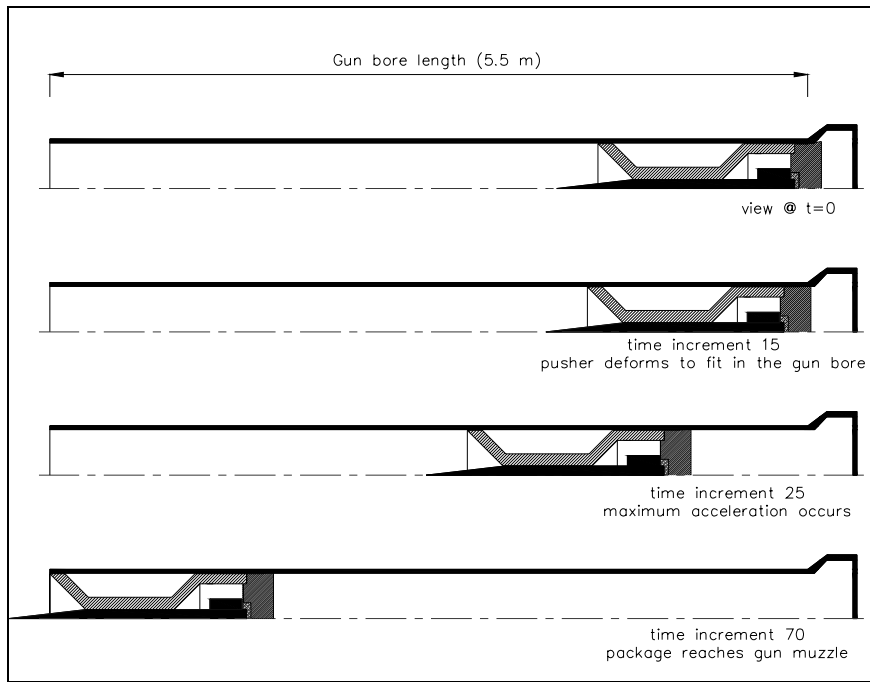


**Figure 103** Package acceleration profile

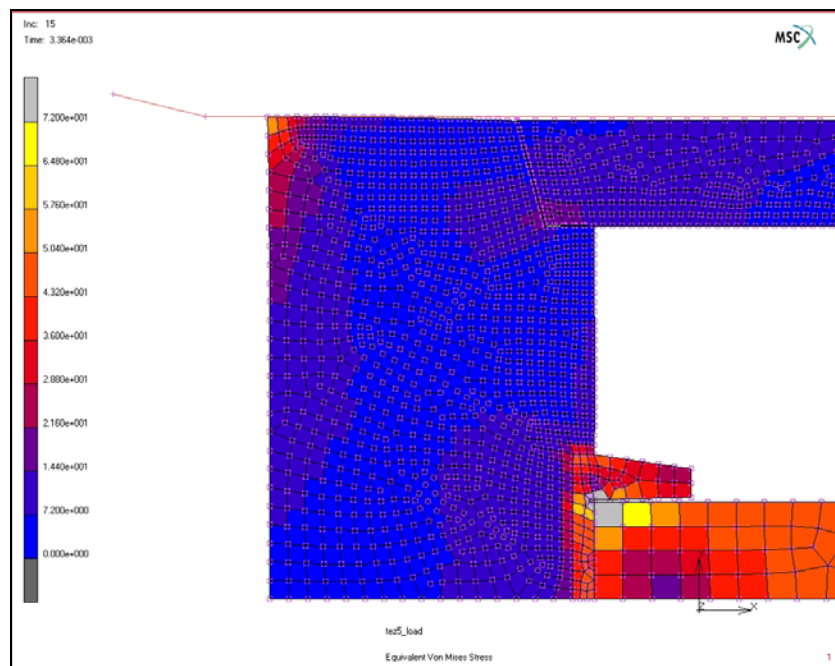
Schematic drawing of the motion of the package in the gun bore with respect to time increments are given in the Figure 104. Figure 104 is not drawn to scale.

Figure 105 shows the 15<sup>th</sup> time increment view of the package. At this instant package just enters the gun bore. Upper left corner of the pusher has high stresses. Since the rear region is larger than the gun tube, it fits in the gun tube by forcing. Scale on the left side shows the von Misses stress.

From acceleration graph, Figure 103, it is seen that maximum acceleration is reached at the 25<sup>th</sup> - 26<sup>th</sup> time increment. Therefore, maximum stress can be seen at 25<sup>th</sup> increment. Figure 106 is the stress history plot of the node located at the center and upper surface of the pusher. Maximum von Misses stress is 55.3 MPa and occurs at 25<sup>th</sup> increment.



**Figure 104** Motion in gun bore



**Figure 105** Test Case 3; time increment 15

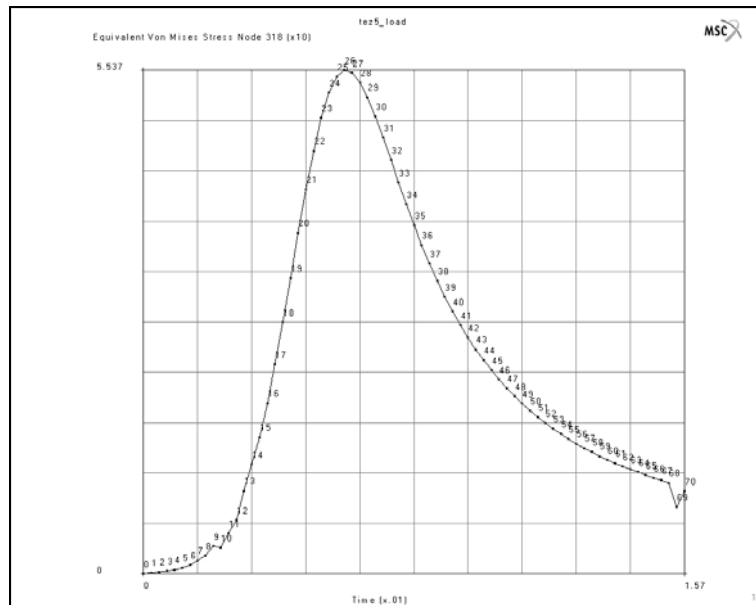


**Figure 106** Stress profile at the center of the pusher

Stresses on the sabot were also obtained from the transient stress analysis. There is difference between static (MSC NASTRAN<sup>®</sup>/PATRAN<sup>®</sup>) and transient (MSC MARC<sup>®</sup>/MENTAT<sup>®</sup>) analysis. In static analysis quarter part of sabot is used. In transient analyses, cross-section of the sabots has been modeled and meshed in two dimensions; however, analyses have been performed in axisymmetric mode. Therefore, in MSC MARC<sup>®</sup>/MENTAT<sup>®</sup>, whole sabot geometries have been analyzed for transient analyses.

In the following figures, maximum stress counter plots and history plots of the nodes with respect to travel time are given for the critical regions. Unit of the scales in contour plots is MPa.

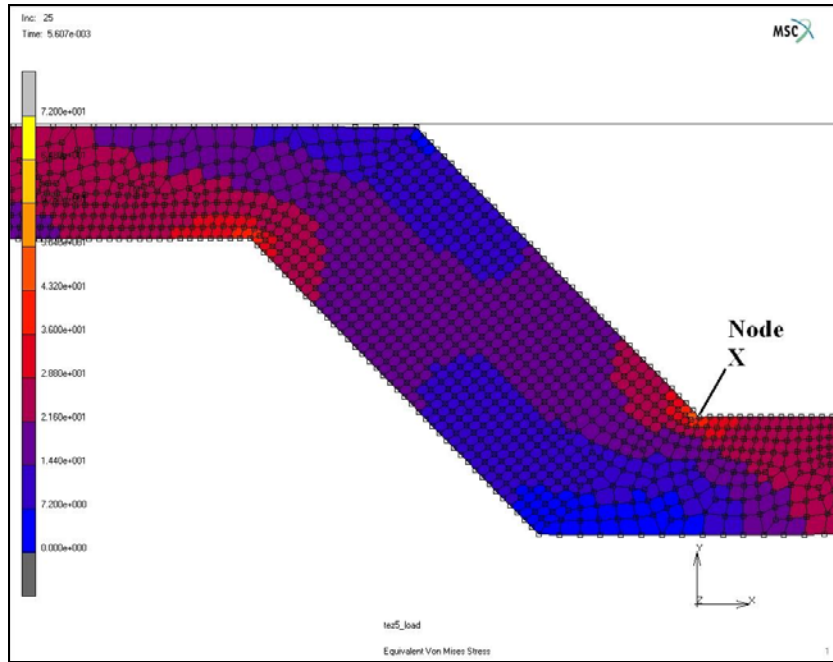


**Figure 107** Test Case 3 section-3, time increment 25

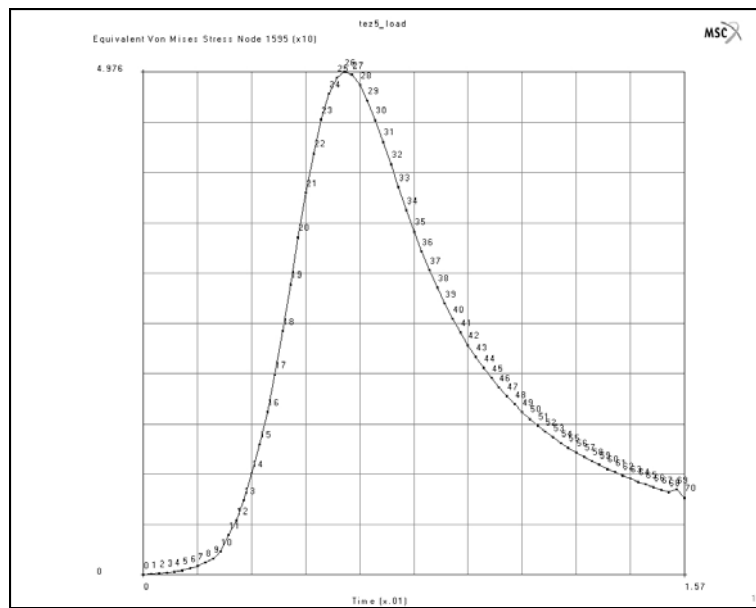


**Figure 108** Stress profile of section-3 node X

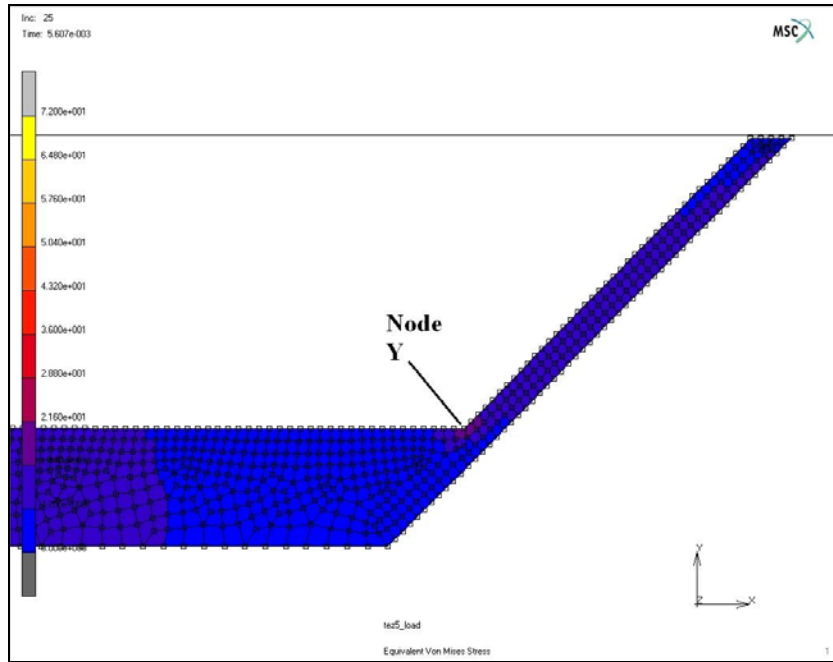


**Figure 109** Test Case 3 section-3, time increment 25

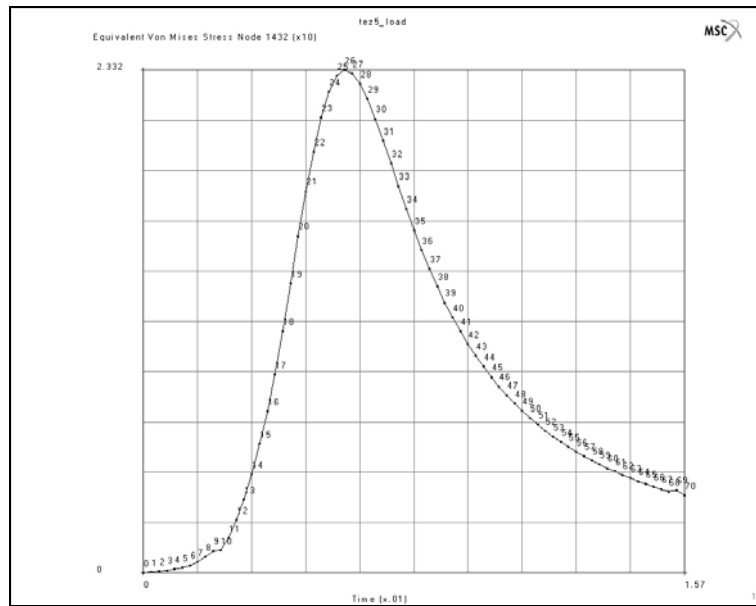


**Figure 110** Stress profile of section-1 node Y

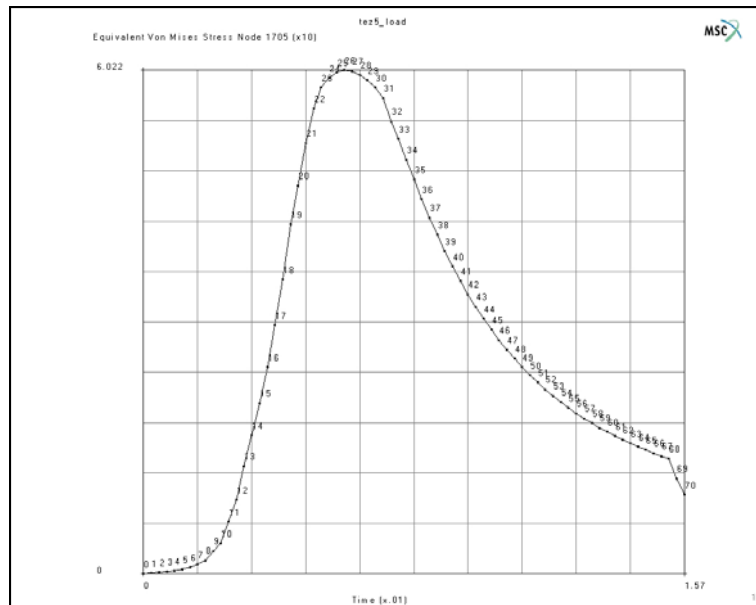


**Figure 111** Stress profile at section-4 of sabot

Figure 111 shows the stress profile of the most rear node which is located on the contact surface between sabot and pusher.

#### 4.3.4. DISCUSSION OF TRANSIENT FEA RESULTS

At these von Mises stress plots, stress scale is fixed to a maximum value, 72 MPa which is the yield stress of polycarbonate. If stress was higher than 72 MPa, this region would be shown as grey. Since the analysis is transient, results change at every time increment. Therefore, stress can be viewed by the stress profile graphs. At section-1 maximum stress is 23 MPa. Since this stress value is very small, 4 mm thickness is used for section-1. Maximum compression stress at section-4 is 60 MPa which is equal to the design stress. Pusher has maximum stress value at the center and it is equal to 55 MPa.

These finite element stresses are expected results. Transient analysis also verifies the SDT results. In addition to the verification of the stresses, by the velocity and

acceleration graphs taken from MSC MARC<sup>®</sup>/MENTAT<sup>®</sup>, pressure calculation equations with acceleration calculations are also verified.

## **4.4 FML TESTS**

From the FML tests it is expected to see whether sabot and pusher will be damaged or not in the gun bore. In addition, it can also be seen whether the model is stable or not during its travel. By using the high speed cameras, sabots can be seen in detail while they are traveling to the test section.

### **4.4.1. PRODUCTION OF THE SABOTS**

All of the four test cases were produced in Mechanical Production Plant and tested in Flight Mechanics Laboratory. Technical drawings of the sabots and pushers have been made. Technical drawing sample for Sabot-1 is given in Appendix C.

Up to the production phase, general preliminary design of a sabot is performed. For the production of a sabot, geometric details should be taken into account. For Basic WAF model, spaces for fins on the pusher support plate are needed. Contact regions on the pusher with sabot and model should have some cavities to protect the radial slippage during the travel in the bore. For 90 degrees corners, a radius should be defined for manufacturing tools.

Sabot is divided into four segments to have a cleaner separation from the model. Shear pins, machined integral with the sabot parts, are provided to prevent different axial movement of the parts during launch [4].

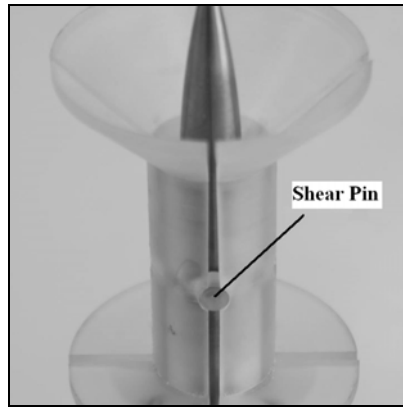


**Figure 112** Shear pin

Another important subject is obturation. For Sabot-1 obturation method was explained. Aft periphery of the pusher is produced larger in diameter. On the other hand, if this method is applied to Sabot-2 pusher, serious damage will occur in the gun wall. As it was mentioned in the previous chapter, pusher material for Sabot-2 is aluminum. Aluminum does not deform easily as polycarbonate. Contact between metal and metal is not preferred. Therefore, another method has been used for obturation. Aluminum pusher is produced smaller in diameter and a cup like polycarbonate structure is used for obturation. In this method, aluminum pusher is fixed in the polycarbonate cup (Figure 113). This cup is larger in diameter at its aft region like the pusher of Sabot-1.

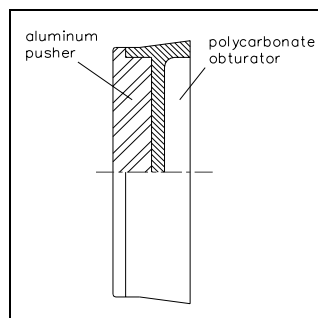


**Figure 113** Sabot-2 obturation

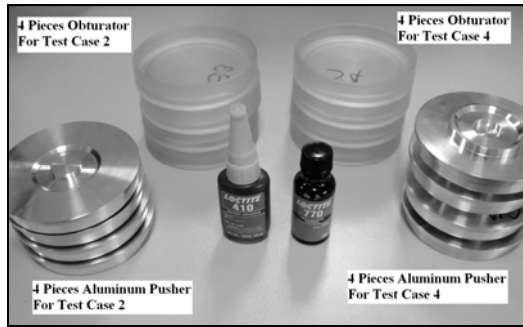


**Figure 114** Produced pushers and obturators

Both materials are glued by Loctite<sup>®</sup> 410 (Figure 115). Loctite<sup>®</sup> 410 is general purpose, toughened adhesive suitable for applications where heat and impact resistance is required.

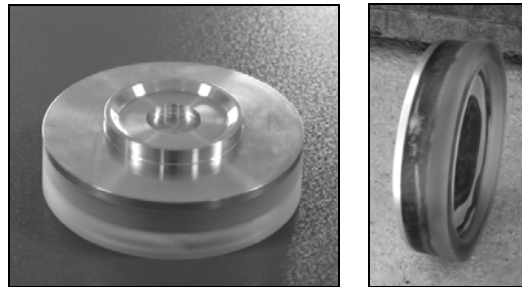


**Figure 115** Sabot-2 pusher after bonding process

Sabot-2 is composed of two materials. Front part is polycarbonate and rear part is aluminum. These two parts are produced in a way that they are fixed with each other on three surfaces by Loctite<sup>®</sup> 410 (Figure 116).

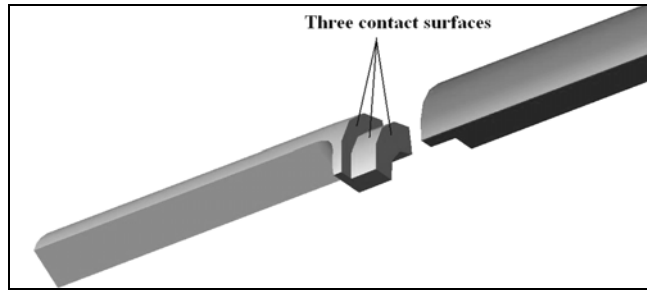


**Figure 116** Contact surfaces between two parts of Sabot-2

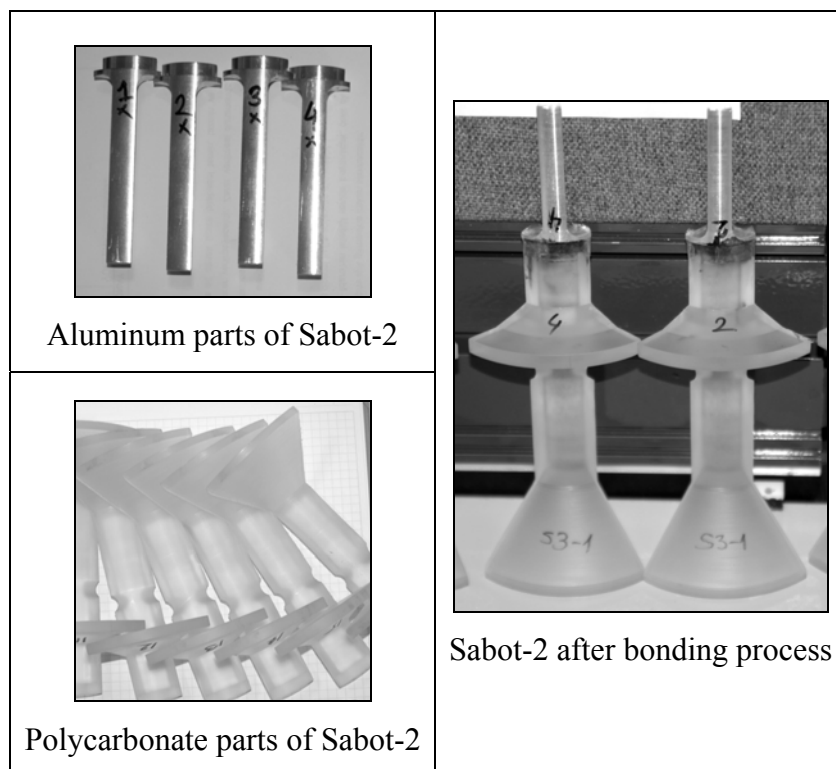


**Figure 117** Produced Sabot-2 parts

Three parts (sabot, pusher and model) are packaged to be placed in the gun bore. Example pictures of the package are taken before the test and they are shown in Figure 118 and Figure 119.

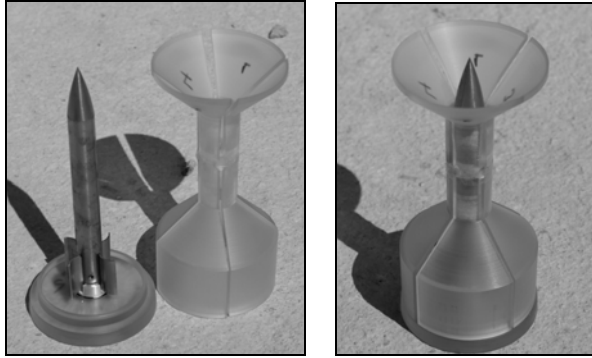


**Figure 118** Sabot-1, pusher and Basic WAF package



**Figure 119** Sabot-2 packages for two different projectiles

#### **4.4.2. TEST SETUP**

During the test phase, packages are fired to the test section. But the entrance hole is closed by high strength steel blocks. The aim is to prevent the models to get in the test section. Since tests are performed for verification purposes until the entrance of the test section, it will be meaningless to take a risk on measurement systems which are located inside the test section.

High speed cameras were used to trace the models and sabots. Image frame rates were 1000-2000 frames per second. Separation of the sabot parts can easily be seen from these videos.

Velocity measurement is very important in the firing tests. If muzzle velocity can be measured, it will be easy to understand whether desired velocity is achieved or not. From this velocity measurement, important information can be obtained. If the model is stable after exiting the muzzle, but the muzzle velocity is less than the desired velocity, there might be a gas leakage around the pusher. To obtain this information, muzzle velocity is measured by using 35.497 GHz frequency Doppler Radar.

#### **4.4.3. TEST RESULTS**

Table 13 summarizes the test results comparing with the SDT results. Calculated package mass is the mass of the sabot, model and pusher which is calculated by the SDT. From volume calculation of the sabot geometry, mass is obtained by multiplying the volume by the density of the materials used. Columns to the right of the Fire No. column are the masses of each part measured by a sensitive weighing machine after production of the parts. Difference between calculated and measured masses comes from the unpredictable glue mass, gap between quarter part sabots which are occurred while cutting with saw, etc.

**Table 13 Test Results-1**

Case No.	Mach	Desired Velocity (m/s)	Calculated Package Mass(gr)	Used Charge Mass (gr)	Fire No.	Measured Pusher Mass (gr)	Measured Sabot Mass (gr)	Model Masst (gr)	Measured Total Package Mass (gr)
1	0.8	272	811.6	37.6	1	175.8	188.7	450.6	815.1
					2	174.9	188.6	450.6	814.1
					3	175.3	188.6	450.6	814.4
2	2	680	1016.9	199.0	4	337.2	243.0	450.6	1030.8
					5	338.0	244.8	450.6	1033.4
					6	337.2	248.4	450.6	1036.2
					7	337.6	243.5	450.6	1031.6
3	2	680	1525.5	282.0	8	269.8	676.7	505.0	1451.5
					9	269.3	677.9	505.0	1452.1
					10	269.6	675.9	505.0	1450.5
					11	269.6	677.2	505.0	1451.8
4	2	680	1220.2	231.0	12	367.6	350.3	505.0	1222.9
					13	370.3	353.8	505.0	1229.1
					14	369.5	351.7	505.0	1226.1

**Table 14 Test Results-2**

Case No.	Fire No.	Desired Muzzle Velocity (m/s)	Measured Muzzle Velocity (m/s)	High Speed Camera Record	Success
1	1	272	x	No	Yes
	2		204	No	Yes
	3		198	Yes	Yes
2	4	680	640	Yes	Yes
	5		609	No	Yes
	6		652	No	Yes
	7		659	Yes	Yes
3	8	680	660	No	Yes
	9		649	Yes	No
	10		650	Yes	Yes
	11		660	Yes	Yes
4	12	680	630	Yes	No
	13		650	Yes	Yes
	14		650	Yes	Yes

Table 13 shows the measured muzzle velocity, and whether the high speed camera record could be taken or not, and the success of the tests. Success criteria for the tests were to see the packages without any damage just after exiting the muzzle and to observe the flight of the projectiles in their trajectories without any disturbance.

Figure 120 is an example screen view of TestCenter<sup>®</sup> Doppler Radar Velocity Measurement software. Software has a capability of making extrapolation on velocity data to able to see muzzle velocity. Figure 120 shows the 2<sup>nd</sup> fire velocity measurement. As it is seen in the figure, muzzle velocity,  $V_0$ , is given as 204.203 m/s.

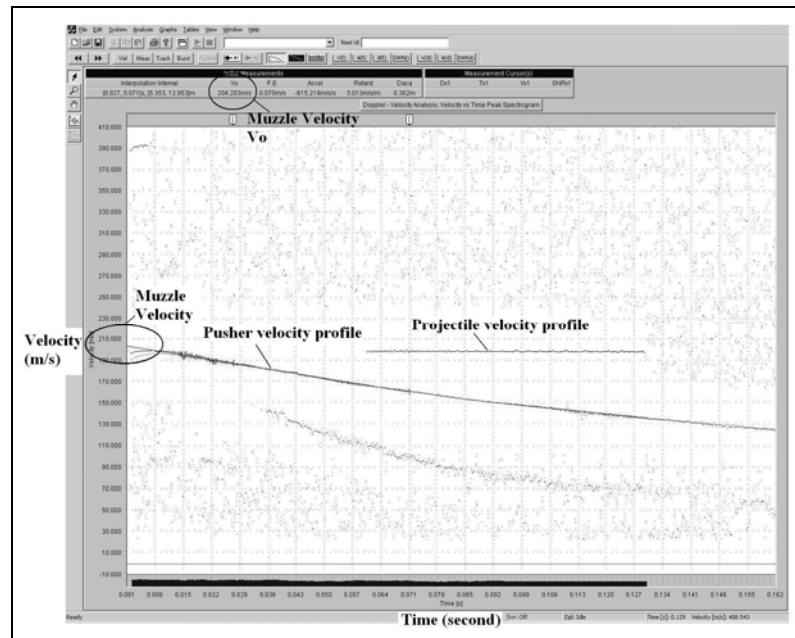


**Figure 120** Example view from velocity measurement software

In Figure 121, sequence of video captures is given as an example. These images were captured from the high speed camera video. This is the 13<sup>th</sup> fire of the tests which belongs to test case 4. It can be clearly seen that Sabot-2 discards smoothly without influencing the flight path of the projectile.

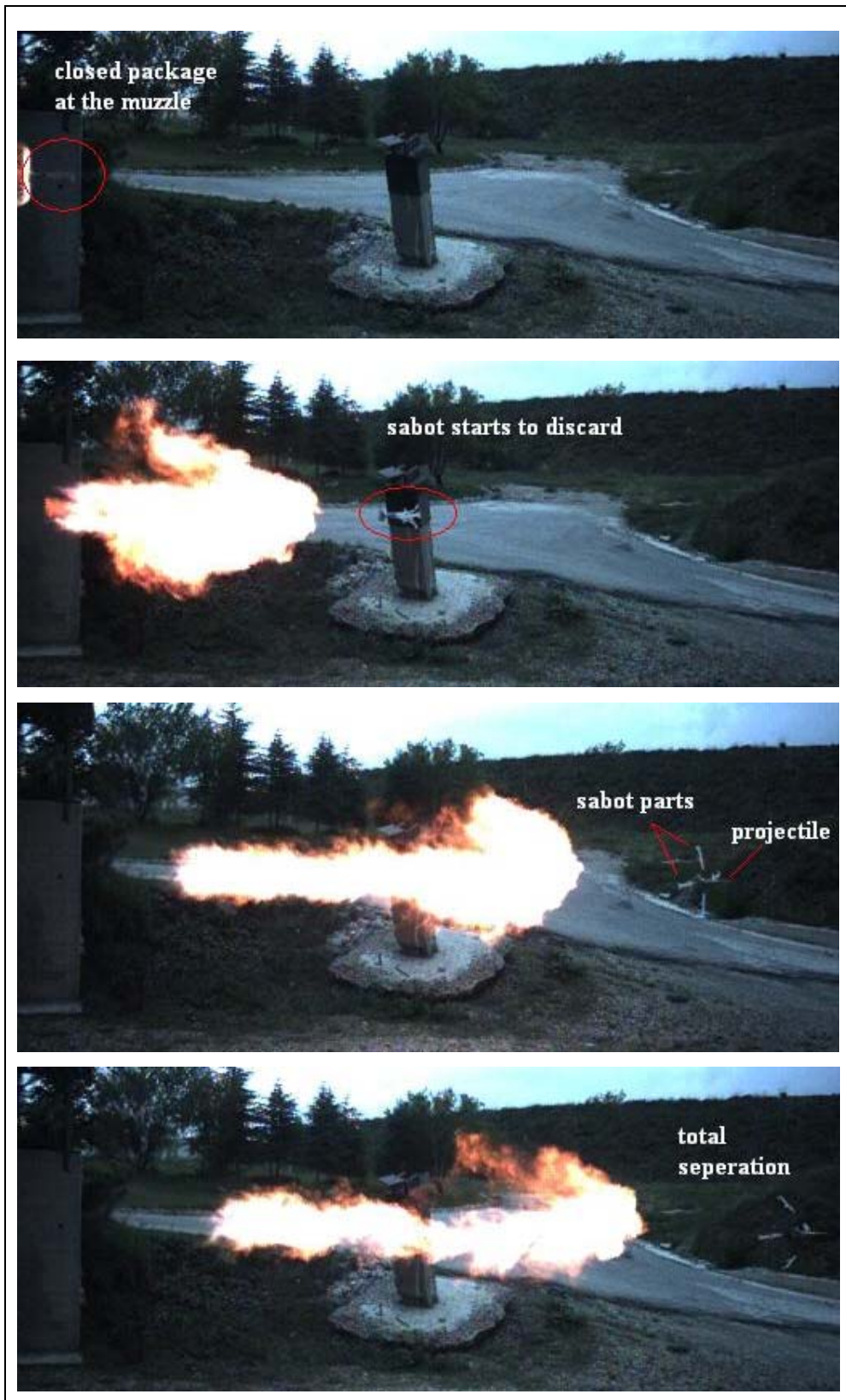


Figure 121 High speed camera images

#### 4.4.4. DISCUSSION OF THE FML TEST RESULTS

FML test results are given in Table 13 and Table 14. Mass calculation results of packages are shown in Table 13. Measured and calculated mass results are very close to each other. Small differences in the results come from manufacturing tolerances, shear pin masses, glue masses, gaps between four parts of sabot etc.

Table 14 shows the desired and measured muzzle velocities. It is clear that, results of test cases 2, 3 and 4 are consistent with each other but there is a small amount of difference between desired and measured velocities. On the other hand, for test case 1 difference is more and this result indicates obturation problem.

In general, during the tests it is not possible to achieve the desired velocity completely. Explosion efficiency of the powder depends on the ambient temperature, ambient humidity and powder's own temperature. Before the tests, powder had been conditioned to 21°C. Since the tests last for a day, powder temperature and humidity changes which affect the velocity seriously. In addition, any differences in the tolerances of the pusher dimensions may change the friction which in turn affects the muzzle velocity. Thus, all of the above causes eventually may lead to a muzzle velocity which is different from the desired muzzle velocity.

The last and the most important reason for inability to reach desired velocity is gas sealing. For test case 1, it is predicted that gas sealing could not be performed perfectly. Pusher thickness of the Test Case 1 is 17.7 mm which is the thinnest pusher used in the tests. The obturation technique was to use larger aft diameter. In Figure 122, it is seen that thin pusher has very narrow obturation surface compared to the thick pusher. This may cause weak gas sealing. This problem can be solved by increasing the aft diameter more or making the aft surface like the polycarbonate obturator of Sabot-2.

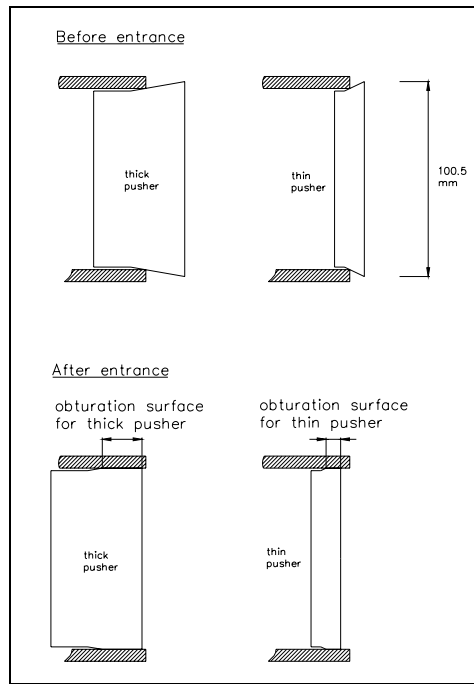


**Figure 122** Obturation surface comparison

Unsuccessful firings 9 and 12 were detected by high speed camera, and it was seen that from the muzzle first a blast of gas and fire exited. Projectile and sabot then came out in broken pieces. This indicates that sabot had been broken in the gun tube which is unacceptable. Since other firings have been successful, these two unsuccessful firings are thought to have different failure mechanism. Reason for this is attributed to the powder condition, which has an uncontrollable explosion and production process.

There is another simple control mechanism to determine the success of the firings. It was mentioned that one of the criteria for the successful firing is flight of the projectile in its trajectory without any disturbance. Thus, projectile should hit the target first at its nose, than starts to deform trough its axial direction. If projectile is not in its trajectory, which means that it has a disturbed and unstable flight, projectile can not hit the target perpendicularly, and hits at its side. From the

deformed shapes of the projectiles this may easily seen. Figure 123 shows pictures of BASIC WAF projectile which are taken after a successful firing.

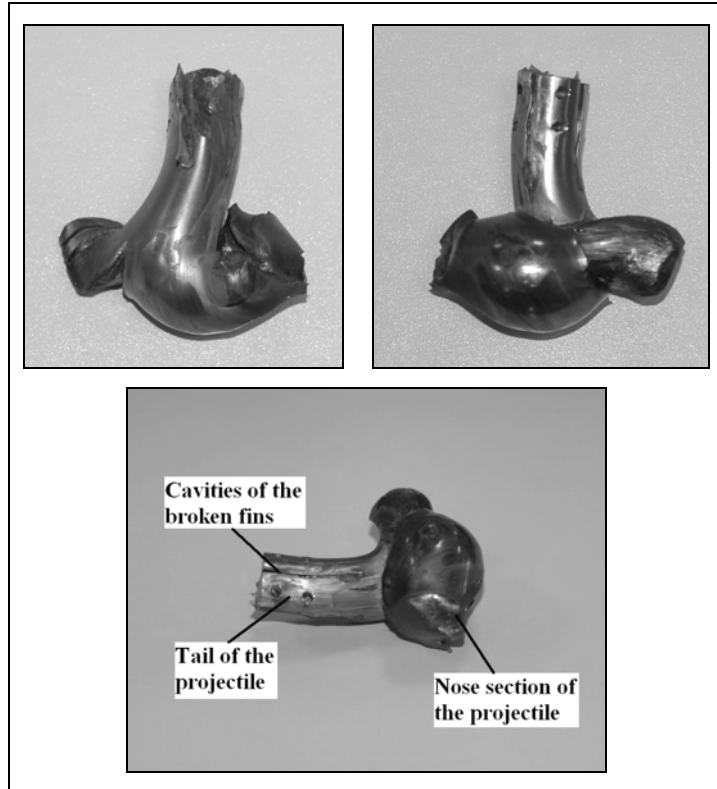


**Figure 123** Deformed projectile after fire

## CHAPTER 5

### DISCUSSION AND CONCLUSION

#### 5.1 DISCUSSION

A new sabot geometry design has been made in this study. The reason for new sabot geometry demand is necessity for tougher sabots for high velocities. In addition, the aim is to design a sabot as light as possible. Certain analyses have been performed by using SDT in order to make a comparison between two sabots, which are designed within the context of this study.

These analyses have also been performed for pushers. In Chapter 3.1 it was explained that for high velocities thickness of the polycarbonate pusher becomes too much thick and weight of the pusher increases. It was also mentioned that instead of using polycarbonate pusher for high velocities, aluminum pusher should be preferred.

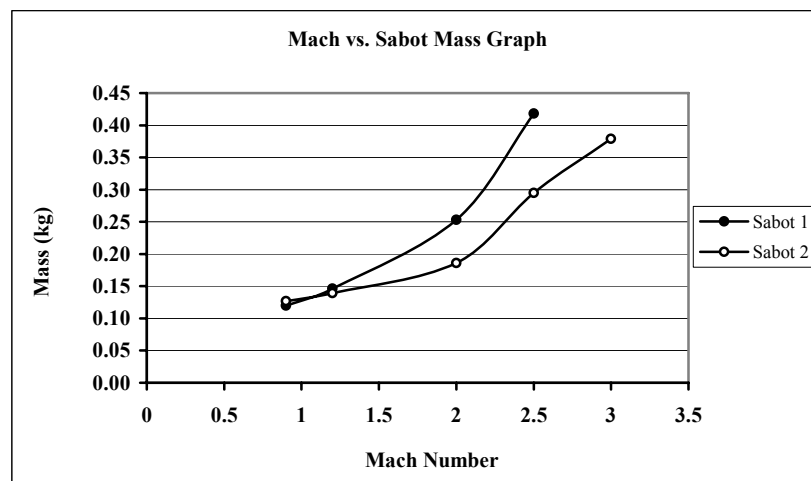
For example, for sabot analyses all the parameters except Mach number were taken as same. Only sabot loop has been used in SDT and pusher parameters for both sabots and for all of the Mach number analyses were same. This situation has been applied to pusher analysis. Only pusher loop was used in SDT and sabot parameters were taken same at all conditions.

In Table 15, results of SDT for two sabots and 5 different Mach numbers are given. Mach number is changing from Mach 0.9 to 3.0 which is the maximum design

Mach number. Sabot parameters B and C, and also modifications AB and D are given.

**Table 15** Sabot Comparison Results Taken From SDT

	Mach 0.9		Mach 1.2		Mach 2.0		Mach 2.5		Mach 3.0	
	Sabot-1	Sabot-2	Sabot-1	Sabot-2	Sabot-1	Sabot-2	Sabot-1	Sabot-2	Sabot-1	Sabot-2
<b>B (mm)</b>	4.24	4.24	5.72	5.70	10.20	9.98	13.20	16.30	-	16.10
<b>C (mm)</b>	3.00	7.63	3.00	7.43	5.19	6.79	16.60	5.74	-	4.60
<b>AB (mm)</b>	0	0	0	0	0	0	2.30	0	-	9.90
<b>D (mm)</b>	-	0	-	0	-	0	-	0	-	6.31
<b>Mass (kg)</b>	0.120	0.127	0.146	0.139	0.253	0.186	0.418	0.295	-	0.379



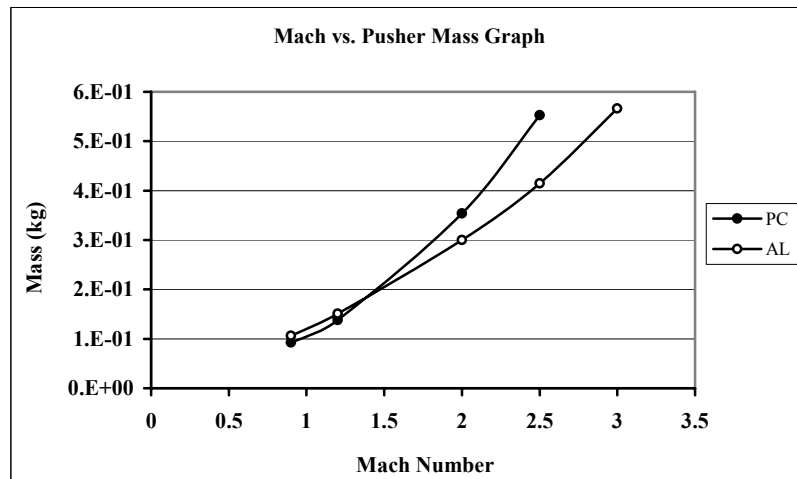
**Figure 124** Mach vs. Sabot Mass graph

Figure 124 shows the relation between Mach number and mass of a sabot. For velocities less than Mach 1 Sabot-1 is lighter than Sabot-2. Thus, Sabot-1 should be preferred for low velocities. On the other hand, as the Mach number increases mass of Sabot-1 increases drastically. Consequently, suggestion that have been made for using Sabot-2 for high velocities has been confirmed.

Pusher and support thicknesses, support diameter and their masses are given in Table 16. PC is polycarbonate pusher and AL is aluminum pusher which belongs to Sabot-1 and Sabot-2, respectively.

**Table 16** Pusher Comparison Results Taken From SDT

	Mach 0.9		Mach 1.2		Mach 2.0		Mach 2.5		Mach 3.0	
	PC	AL	PC	AL	PC	AL	PC	AL	PC	AL
Thickness (mm)	9.5	5.0	13.9	7.1	34.8	14.1	43.9	19.6	-	26.7
Support Thickness (mm)	1.8	-	3.6	-	13.5	-	18.9	-	-	-
Support Diameter (mm)	3.0	-	30.0	-	30.0	-	59.0	-	-	-
Pusher Mass (kg)	0.090	0.106	0.131	0.151	0.328	0.300	0.413	0.415	-	0.566
Support Mass (kg)	0.003	-	0.007	-	0.026	-	0.140	-	-	-
Total Mass (kg)	0.093	0.106	0.138	0.151	0.354	0.300	0.553	0.415		0.566



**Figure 125** Mach vs. Pusher Mass graph

Almost same trend is obtained for pusher (Figure 125). It is seen that for velocities higher than Mach 1.5, aluminum pusher becomes lighter than polycarbonate pusher. In conclusion, using aluminum pusher for high velocities would be efficient.

## 5.2 CONCLUSION

In this study, development of a sabot design tool has been performed in detail. Conventional sabot geometry which has been used in FML tests is first investigated. According to investigations, disadvantages of the conventional sabot, which is named as Sabot-1, are determined. As a result new sabot geometry is designed to meet the needs for high speed testing. This new sabot, named as Sabot-2, has better physical and geometrical properties and it can resist high accelerations.

For both of the sabot geometries, stress critical regions are determined and stress calculation methods are decided. Strength of materials approach is used and approximate stress calculation methods are determined. Appropriate relations for different regions on sabots are derived.

For some regions on the sabot because of the complex geometry, some assumptions are made to make the strength of materials formulas applicable. The aim of stress analysis in this study is to use simple static stress relations, to be used in the analysis of the sabot. The results of these relations have to be checked by the reliable sources. Therefore, results obtained from the approximate relations are compared with finite element solutions, and it was observed that some formulas needed corrections. These correction factors are achieved by the help of the finite element analyses.

From the literature survey, especially in USA sources, simple stress formulas are directly used for sabot design without any corrections. For pusher part, thin plate theory is used in Reference [3] which is a US Army Sabot Design Handbook. But from the solutions it is easily seen that pusher thicknesses do not obey the thin plate theory assumption. Although thin plate formulation is used in some sources, in this study thick plate formulas are derived to achieve more accurate results.

After all the stress analysis procedures are determined, sabot design can be made. Stress analysis procedures contain heavy and iterative calculations. Therefore, computer aided Sabot Design Tool, SDT, is developed. Calculations, iterations and modification decisions to achieve the lightest sabot are done automatically by SDT. To verify the SDT, results of the tool is compared with finite element results. In addition, sabots which are designed by SDT are manufactured and tested in FML.

Static finite element results show that estimated critical regions are correct and stresses at critical regions are not exceeding design stresses. These results are also verified by transient analysis. From transient analysis results it is seen that model can reach the desired muzzle velocity, from this result it can also be concluded that pressure, acceleration and mass calculations in the SDT are consistent.

In FML tests manufactured sabots are physically tested. From velocity measurements it is seen that models reach the desired muzzle velocity with 5% bias error. Separations of the sabots from the models have been monitored and it is concluded that designed sabot geometries are immensely sufficient for use in FML tests in the future.

Major objective of this study is achieved successfully by developing a sabot design tool. This tool can be used by an engineer who has knowledge about aeroballistic range testing. SDT will be very useful for Flight Mechanics Division of TÜBİTAK-SAGE, since time to design a sabot for a specific test condition is reduced. In addition, the use of the SDT is simple enough so that an inexperienced engineer can also use it effectively.

### **5.3 FUTURE WORK**

To make the SDT user friendly, graphical user interface is needed. Although, the input data and the output data structure are simple, graphical user interface makes the usage of the SDT easier.

Friction coefficient between pusher and gun wall is taken as 0.5 in SDT stress calculations. This value is determined from the references of polycarbonate material. But friction coefficient in the gun bore can be calculated by performing some pull out tests. If coefficient is known exactly, acceleration calculations will be more reliable.

Safety factor that is used in SDT is 1.2, and it is applied to the yield strength. FML tests show that sabots resist the loadings in the gun bore. In the future, FML tests can be repeated with sabots which are designed by using different safety factors or without safety factor, and from these tests a specific safety factor for designing a sabot can be determined. Thus, unknown dynamic effects in the gun bore can be included into the sabot design safety factor.

The most important thing which should be investigated in the future is separation of the sabots. Detailed separation analyses are not in the scope of this study; however aerodynamic analysis after gun exit should be taken into account during sabot design process.

## REFERENCES

- [1] Mahmutyazıcıoğlu, G., Tanrıkulu, Ö., “**Aeroballistic Research Laboratory (ARL) Project**”, 47<sup>th</sup> ARA Meeting, (1996)
- [2] Daniel, D.C., Boudreau, A.H., “**Trends in International Aerospace Ground Test Facilities**”, AIAA Paper, AIAA-93-0348, (1993)
- [3] Engineering Design Handbook, “**Sabot Technology Engineering**”, Headquarters US Army Materiel Command, (1972)
- [4] “**Ballistic Range Technology**”; AGARDograph No.138, (1970)
- [5] Burns, B., Drysdale, W., Hoppel, C., Bogetti, A., “**The Development of Composite Sabots for Kinetic Energy Projectiles**”, 19<sup>th</sup> Int. Symposium of Ballistics, (2001).
- [6] Rabern, D. A., Parker, R. B., “**Launch Behavior of 60mm Pushed and Traction Driven Saboted Launch Packages**”, Int. J. Impact Engineering Vol. 16, No. 1, (1995)
- [7] Ugural, C. A., Fenster, S. K., “**Advanced Strength and Applied Elasticity**”, Prentice Hall
- [8] Cayzac, R., Carette, E., Alziary de Roquefort, T., “**Intermediate Ballistics Unsteady Sabot Separation: First Computations and Validations**”, 19<sup>th</sup> Int. Symposium of Ballistics, (2001).

- [9] Mikhail, A., Heavey, K., “**Sabot Opening Lift Force: Analysis, CFD and Test**”, 38<sup>th</sup> Aerospace Sciences Meeting and Exhibit, (2000).
- [10] Ugural, C.,A., “**Stresses In Plates and Shells**”, McGraw-Hill, (1999)
- [11] Timoshenko, S., “**Theory of Elasticity**”, McGraw-Hill
- [12] Sokolnikoff, I., S., “**Mathematical Theory of Elasticity**”, (1941)
- [13] Beer, F., P., Johnston, E., R., “**Mechanics of Materials**”, McGraw Hill, (1992)
- [14] “**Design and Analysis of Machine Elements Course Notes**” [On-line]  
Available:  
<http://www.mech.uwa.edu.au/DANotes/buckling/columns/columns.html>
- [15] “**Practical Columns- Design Equations**” [On-line] Available:  
[http://www.efunda.com/formulae/solid\\_mechanics/columns/eccentric.cfm](http://www.efunda.com/formulae/solid_mechanics/columns/eccentric.cfm)
- [16] Peery, D., J., Azar, J., J., “**Aircraft Structures**”, McGraw Hill
- [17] “**MSC Marc Volume B – Element Library**”, MSC Marc documents, (2005)
- [18] Fleeman, E., L., “**Tactical Missile Design**”, AIAA Education Series, (2001)

# APPENDIX A

## PRESSURE DATA

In Figure 126 - Figure 130, calculated maximum pressure data with respect to package mass is given. Pressure equation, 'y', is pasted on the graphs for 0.8, 0.9, 1.2, 2, 2.5 Mach numbers.

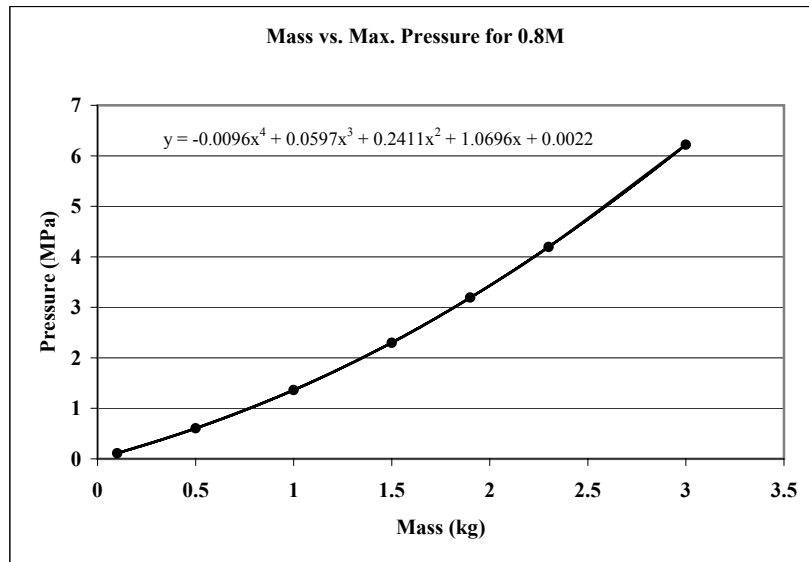


**Figure 126** Mass vs. Pressure graph for Mach 0.8

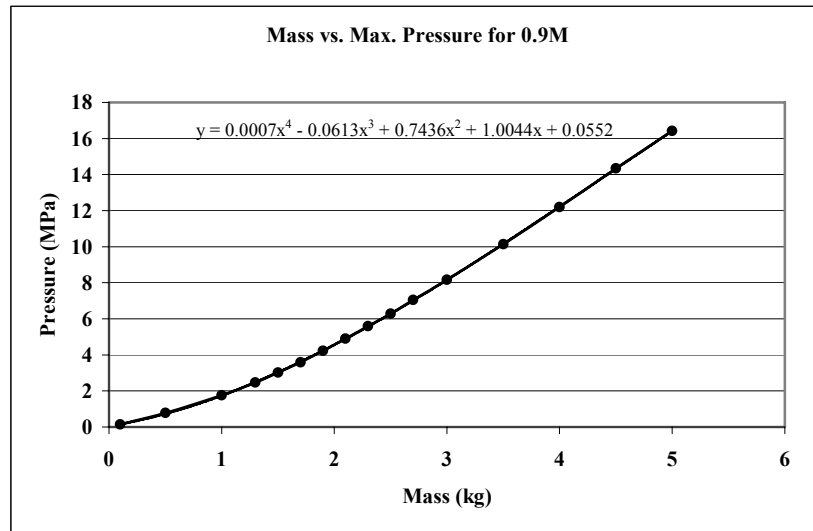


**Figure 127** Mass vs. Pressure graph for Mach 0.9

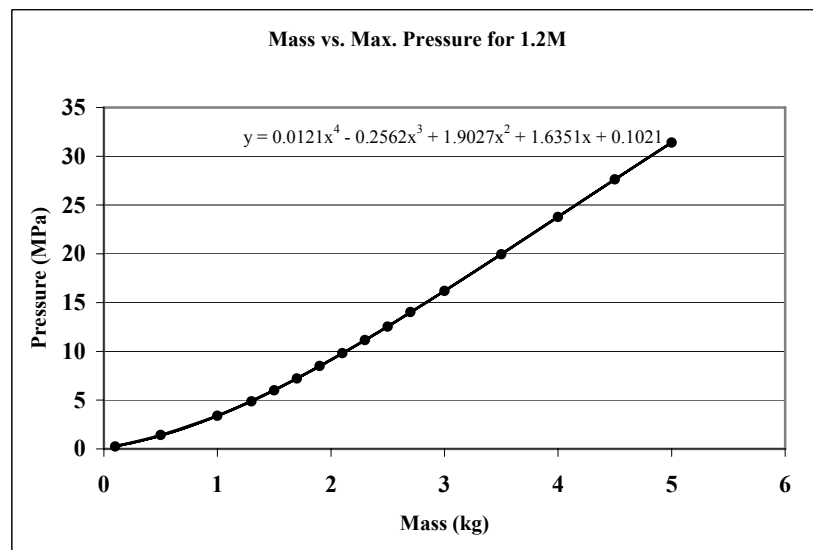


**Figure 128** Mass vs. Pressure graph for Mach 1.2

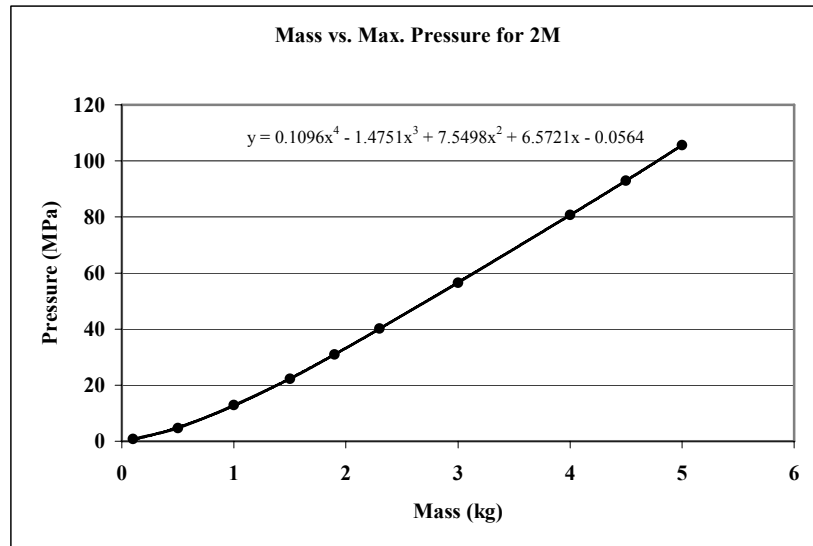


**Figure 129** Mass vs. Pressure graph for Mach 2

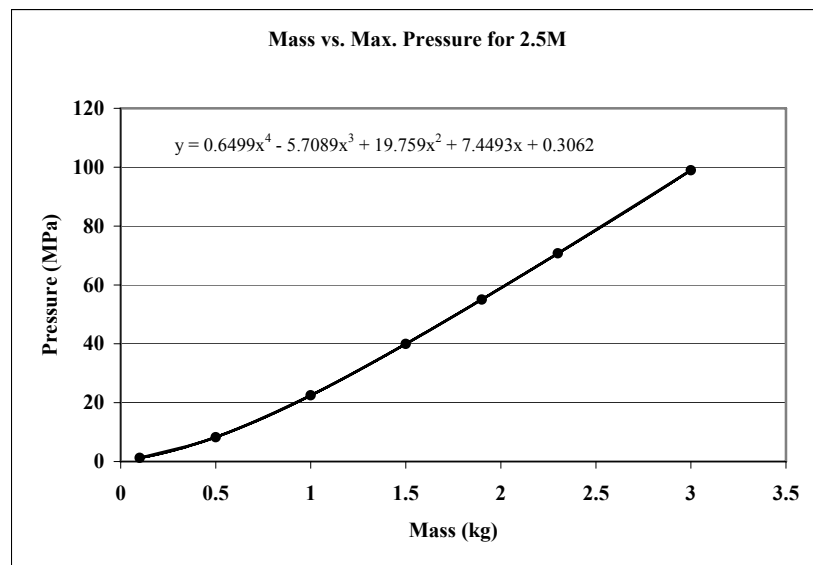


**Figure 130** Mass vs. Pressure graph for Mach 2.5

## APPENDIX B

### SABOT SECTION COORECTION FACTORS

#### B.1 SECTION-1 CORRECTION FACTORS

Section-1 correction factors for both sabots are given in Equations (78) - (81) for other 'B' values.

B=2.5 mm;

$$\ln(c_{nA}) = a + bA^{1.5} + c\sqrt{L} \quad (78)$$

where constants are;

$$a = 3.369$$

$$b = -0.00024989$$

$$c = -25.4207$$

B=5 mm;

$$\ln(c_{nA}) = a + be^{-A} + c\sqrt{L} \quad (79)$$

where constants are;

$$a = 162.8553$$

$$b = -161.3992$$

$$c = -26.41238$$

B=10 mm;

$$\ln(c_{nA}) = a + bA^2 \ln(A) + c\sqrt{L} \quad (80)$$

where constants are;

$$a = 1.77639$$

$$b = -2745.1569$$

$$c = -26.507488$$

B=20 mm;

$$\ln(c_{nA}) = a + b \ln(A)/A + cL \quad (81)$$

where constants are;

$$a = 1.75279$$

$$b = 0.0007672$$

$$c = -96.5668$$

## **B.2 SECTION-3 CORRECTION FACTORS**

Section-3 correction factors of Sabot-1 are given in the following equations for other 'B' values.

B=2.5 mm;

$$\ln(c_{nC}) = a + b\sqrt{A} + c\sqrt{L} \ln(L) \quad (82)$$

where constants are;

$$a = 1.2646$$

$$b = -36.3383$$

$$c = -7.5101$$

B=5 mm;

$$\ln(c_{nC}) = a + b/\ln(A) + c \ln(L) \quad (83)$$

where constants are;

$$a = 12.63238$$

$$b = 30.9494$$

$$c = 1.01285$$

B=10 mm;

$$\ln(c_{nC}) = a + b\sqrt{A} \ln(A) + c \ln(L) \quad (84)$$

where constants are;

$$a = 10.24459$$

$$b = 9.75054$$

$$c = 1.00444$$

B=20 mm;

$$\ln(c_{nC}) = a + b \ln(A) + c\sqrt{L} \ln(L) \quad (85)$$

where constants are;

$$a = -7.3086$$

$$b = -1.1068$$

$$c = -7.03678$$



